Title
Time-Stretch Accelerated Instrumentation for High-Speed Signal Analysis and Ultra-fast Device Characterization

Author
Lonappan, Cejo Konuparamban

Publication Date
2018

Peer reviewed|Thesis/dissertation

UNIVERSITY OF CALIFORNIA

Los Angeles

Time-Stretch Accelerated Instrumentation for High-Speed Signal Analysis and Ultra-fast Device Characterization

A dissertation submitted in partial satisfaction
of the requirements for the degree
Doctor of Philosophy in Electrical Engineering

by

Cejo Konuparamban Lonappan

2018

ABSTRACT OF THE DISSERTATION

Time-Stretch Accelerated Instrumentation
for
High-Speed Signal Analysis
and
Ultra-fast Device Characterization

by

Cejo Konuparamban Lonappan
Doctor of Philosophy in Electrical Engineering
University of California, Los Angeles, 2018
Professor Bahram Jalali, Co-Chair
Professor Asad Mohamed Madni, Co-Chair

Internet traffic has been growing exponentially due to the increasing popularity of bandwidth-hungry applications among mobile and cloud platforms, as well as the increased penetration of broadband technologies. The advancements in fiber optic communication technology has enabled the scaling of data rates to very high bandwidths to support the increasing global data traffic growth. This has come at the cost of making the optical network infrastructure too rigid to changes in demand, difficult to service and maintain, and energy inefficient. The next-generation of optical networks needs to be more agile so that it can dynamically scale network resources based on demand, identify and locate impairments in the network automatically, be resilient to network disaster and cybersecurity attacks, and be more energy efficient. This necessitates the development of software-defined networking at the physical layer of optical networks with rapid optical performance monitoring capabilities to be able to dynamically modify the network and its parameters to ensure high quality of service and energy efficiency. Rapid optical performance monitoring requires high-throughput instruments that can analyze high-speed optical signals accurately with low power consumption.

The increasing demand for higher data bandwidth is leading the communication industry to increase the operating frequency of components and systems. Performing accurate and rapid measurements of the various characteristics of electronic, electro-optic, and opto-electronic devices, modules, and systems at these high bandwidths is very challenging. With increasing operating frequencies, the conventional test equipment cost, size and power consumption also scales up proportionately. Longer test times to achieve increased accuracy would result in significantly higher test costs, hence innovations in faster testing of high bandwidth components and systems is a breakthrough that the test engineering community is anxiously awaiting for.

Electronic digitizers are an integral part of modern digital instrumentation systems. The resolution and speed limits of analog-to-digital converters presents the bottleneck in the development of high-throughput, high bandwidth instruments. Photonic time-stretch technology boosts effective bandwidth and sampling rate of the conventional electronic digitizers by 50 to 100 times by slowing down the high bandwidth signals prior to digitization and signal processing. Time-stretch technology is a fundamentally different approach to broadband digitization technology. Instead of increasing the speed of back-end analog-to-digital converters and digital signal processors to keep up with ever accelerating data rates, time-stretch slows down incoming signals before digitization, reducing the analog bandwidth of the signal. By employing this technique, lower speed, higher resolution, more energy efficient digitizers and signal processors can be used to capture and process full wide-band signals in real-time. In addition, the time-stretch architecture scales with digitizer and signal processor technology, continually improving in resolution, speed, and energy efficiency as the electronic back-end technology progresses.

In the first part of this dissertation, I discuss my work in the development of a novel photonic time-stretch accelerated processor for in-service, real-time burst-mode optical performance monitoring to enable the implementation of agile optical networks. This instrument with an equivalent 2 Terabit/s burst mode processing capability measures the bit-error rate, an important metric for the quality of transmission, of 40 Gigabit/s data with a 28 microsecond acquisition time. With a low power consumption of 50 W, this instrument has a

real-time burst sampling throughput of 250 Giga-samples/s using an electronic digitizer with only 2.5 Giga-samples/s sampling rate at 2 GHz analog bandwidth. The measured bit-error rate is transmitted as a feedback to the software-defined networking controller to automatically take corrective actions in case of impairments or network disasters. I also discuss the various demonstrations using this instrument such as in-service analysis of streaming video packets at 10 Gigabit/s on a commercial optical networking platform, characterization of various non-linear effects in optical fiber networks, and an ultra-fast instantaneous frequency measurement system.

In the second part of this dissertation, I discuss the development of an innovative high-performance single-shot network analyzer employing photonic time-stretch for extremely fast frequency response measurement of high bandwidth electronic, opto-electronic, and electro-optic devices, modules, and systems. This single-shot network analyzer has an effective sampling throughput of 2.5 Tera-samples/s at 40 GHz analog bandwidth. This instrument also features an extremely fast acquisition time of 27 nanosecond, a measurement jitter of 5.4 femtosecond, and a power consumption of 50 W.

The dissertation of Cejo Konuparamban Lonappan is approved.

Chang-Jin Kim

Subramanian S. Iyer

William J. Kaiser

Asad Mohamed Madni, Committee Co-Chair

Bahram Jalali, Committee Co-Chair

University of California, Los Angeles

2018

To my parents,

Anna Puthenparampu Joseph

and

Lonappan Konuparamban Devassy

TABLE OF CONTENTS

LIST OF FIGURES

LIST OF TABLES

ACKNOWLEDGMENTS

My doctoral work and life have been influenced, inspired, advised, encouraged, and supported by many individuals. First and foremost, I would like to thank both of my doctoral advisors, Prof. Bahram Jalali and Prof. Asad M. Madni for giving me the privilege of being their student.

I express the deepest appreciation to my advisor, Prof. Bahram Jalali for his guidance and support of my doctoral research. His insights, ideas, and passion has been very inspirational and thought provoking. I am also grateful to him for all the valuable professional advice he has given me and for providing the opportunities for my professional growth.

I wholeheartedly thank Prof. Asad M. Madni for the enormous encouragement, advice, and support he has given me during my research. I am inspired by his exceptional punctuality, professionalism, leadership, and passion for engineering and teaching. I am extremely grateful to Prof. Madni for not only treating me like his son, but for also being very strict and critical of me when needed. I also thank his wife, Gowhartaj Madni and son, Jamal Madni, for welcoming me to their family and for all the support and encouragement they have showered upon me.

I also thank my dissertation committee members, Prof. Chang Jin Kim, Prof. Subramanian S. Iyer and Prof. William J. Kaiser, for their valuable guidance, patience, and encouragement. Prof. Kaiser is an exceptional educator from whom I have learned a lot and I appreciate all the kindness and support he has given me during my time at UCLA.

I have had the opportunity of working with amazing students and post doctoral scholars at UCLA. I wish to thank Dr. Brandon Walter Buckley, Dr. Daniel Wai Chuen Lam, Prof. Jost Adam, Dr. Eric Diebold, Dr. Ali Ayazi, Dr. Ata Mahjoubfar, Dr. Ali Motafakker-Fard, Dr. David Borlaug, Dr. Jacky Chak-kee Chan, and Dr. Sebastian Karpf for their insights and collaborations. I also thank the co-authors on all my publications.

I want to thank the sponsoring organizations, Center for Integrated Access Networks (CIAN) - a National Science Foundation funded Engineering Research Center, IEEE In-

strumentation and Measurement Society Graduate Fellowship, and the Office of the Naval Research, for their funding and support. I thank our collaborators, professors Daniel C. Kilper and John Wissinger, at the University of Arizona; Keren Bergman at Columbia University; and Alan Willner at University of Southern California, and their students and post doctoral scholars Dr. Sarmad Albanna, Dr. Weiyang Mo, Ajay Gautham Manicka Sureshbabu, Dr. Stanley Johnson, Dr. Atiyah Sayyidah Ahsan, Dr. Michael S. Wang, and Dr. Ahmed Almaiman.

Finally and most importantly, I want to express my deep gratitude and appreciation to my entire family, and friends for their love, support, and encouragement.

VITA

2000–2004 Bachelor of Technology in Electronics and Communication Engineering, Model Engineering College, Kochi, Kerala, India.

2005 Post Graduate Diploma in VLSI, Semiconductor Complex Limited, India.

2006–2007 Test Engineer, Cypress Semiconductors, Bangalore, India. Did post silicon validation and testing on four-PLL based programmable clocks products for desktop and laptop computer motherboards.

2007–2009 Lecturer, Department of Electronics Engineering, Model Engineering College, Kochi, Kerala, India. Taught solid state devices and ASIC design. Started the advanced laboratories for the graduate program in VLSI and Embedded Systems.

2009–2010 Research Project Staff, Department of Electrical Engineering, Indian Institute of Technology Bombay, India.

2010–2012 Master of Science, Department of Electrical Engineering, University of California, Los Angeles, USA.

2013–present Graduate Student Researcher, Department of Electrical Engineering, University of California, Los Angeles, USA.

2017–present Chair, IEEE Photonics Society Los Angeles Chapter, California, USA.

PUBLICATIONS

Bahram Jalali, **Cejo Konuparamban Lonappan**, Asad M. Madni, "A method for characterizing Terahertz signals," World and U.S. Patent (Applied), 2018.

B. Jalali, M. Suthar, **C. K. Lonappan**, A. Ribas, T. S. Nowicki, J. M. Chen, "A method for digital pathology using augmented reality," World and U.S. Patent (Applied), 2018.

Bahram Jalali, **Cejo Konuparamban Lonappan**, "A method for signal characterization," World and U.S. Patent (Applied), 2018.

Cejo Konuparamban Lonappan, Asad M. Madni, and Bahram Jalali, "Single-shot network analyzer for extremely fast measurements," Applied Optics 55, 8406-8412 (2016).

Bahram Jalali, **Cejo Konuparamban Lonappan**, Asad M. Madni, "Single-shot Network Analyzer (SiNA)," World and U.S. Patent (Applied), 2016.

C. K. Lonappan, B. W. Buckley, D. W. Lam, A. M. Madni, B. Jalali, J. Adam, "Time-stretch accelerated processor for real-time, in-service, signal analysis," Signal and Information Processing, 2014 IEEE Global Conference on, Atlanta, GA, 2014, pp. 707-711.

D. W. Lam, , B. W. Buckley, **C. K. Lonappan**, A. M. Madni, B. Jalali, "Ultra-wideband instantaneous frequency estimation," in IEEE Instrumentation & Measurement Magazine, vol. 18, no. 2, pp. 26-30, April 2015.

A. Ayazi, K. Goda, J. Sadasivam, **C. K. Lonappan**, J. Adam, D. R. Gossett, E. Sollier, A. Fard, S. C. Hur, C. Murray, C. Wang, N. Brackbill, D. Di Carlo, B. Jalali, "Real-time image processor for detection of rare cells and particles in flow at 37 million line scans per second," SPIE Photonics West, San Francisco, CA (2013).

K. Goda, A. Ayazi, D. R. Gossett, J. Sadasivam, **C. K. Lonappan**, E. Sollier, A. Fard, S. C. Hur, J. Adam, C. Murray, C. Wang, N. Brackbill, D. Di Carlo, B. Jalali, "High-throughput single-microparticle imaging flow analyzer," Proceedings of the National Academy of Sciences 109, 11630 (2012).

CHAPTER 1

Introduction

The global data traffic has been growth exponentially due to the rapid increase in the popularity of bandwidth-hungry applications among mobile phone users and the adoption of cloud computing platforms. As shown in Figure 1.1, the Ethernet Alliance predicts deployment of 400 Gigabit Ethernet (GbE) links in hyperscale data centers by 2020, with 800 GbE and 1.6 Terabit Ethernet (TbE) connectivity being achieved in the next five years or so [1]. The mobile data traffic has grown 18-fold over the past 5 years [2]. The growth in data traffic is caused by the ever-increasing insatiable demand for higher bandwidth for various applications and the increased penetration of broadband technologies among users.

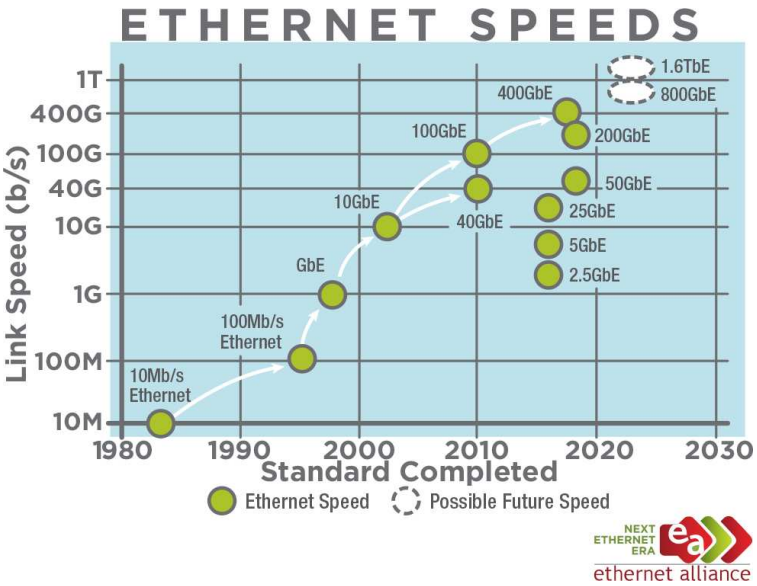

Figure 1.1: Ethernet Roadmap 2018 by the Ethernet Alliance. Courtesy of [1].

The annual global Internet Protocol (IP) traffic is expected to reach 3.3 zettabytes (ZB) per year by 2021, or 278 exabytes (EB) per month [3]. The major sources for the increased

traffic are bandwidth-intensive applications such as streaming video and audio, cloud based web-services, social media, gaming, etc. Additionally, the 5G mobile network technologies is expected to provide 30 to 50 times faster speeds than 4G and is expected to utilize a mobile backhaul network based on fiber optics. The advancements in fiber optic communication technology over the last two decades has enabled the global data traffic to grow exponentially, as predicted by Keck's Law [4].

1.1 Recent Developments in Fiber Optic Communications

The fiber optic communication networks have also evolved to meet the enormous bandwidth requirements, for example, the adoption of advanced modulation formats using digital coherent receivers and Wavelength Division Multiplexing (WDM) for achieving high spectral efficiency [5, 6]. The fiber transmission speeds have been further increased by combining quadrature amplitude modulation with polarization multiplexing on the transmitter side and coherent detection, digital signal processing, and high performance Forward Error Correction (FEC) [7] on the receiver side, and also by Faster-than-Nyquist (FTN) modulation and demodulation [8]. With the introduction of super-channels employing techniques such as Orthogonal Frequency-Division Multiplexing (OFDM), the bit-rates rates have been increased beyond Terabit/s [9, 10]. Numerous demonstrations of long-haul, ultra-high fiber transmission speeds exceeding many Terabit/s have been reported by both academic research community [11–13] and industry [14–17]. Combined with the aforementioned advanced modulation and detection schemes and WDM, the development of newer complex network architectures employing Re-configurable Optical Add-Drop Multiplexers (ROADM) with flexible grids have enabled the development of a dynamic, flexible/elastic optical network with a better utilization of the available transmission capacity [18].

The increase in data bit-rates is not just limited to long-haul fiber communication. The global intra-data center IP traffic is expected to grow at a Compound Annual Growth Rate (CAGR) of 23.4 percent from 2016 to 2021 [19]. This growth is driven by the increasing Machine-to-Machine (M2M) traffic as well as the demand for higher bandwidth for cloud

services, big data applications, increasing digitization, mobility, and the Internet of Things (IoT). Such increased growth in intra-data center traffic is driving the higher bandwidth capabilities for the Data Center Interconnects (DCI) with bit rates extending to 400G with four-level pulse amplitude modulation (PAM4). These demands have increased the interest in the development of integrated photonic systems [20, 21] employing silicon-photonics [22–26], III-V compound semiconductor [27–30] as well as hybrid [31–34] and heterogeneous integration [35–37], and packaging technologies [38–41]. The data-center interconnect bottlenecks for networking and computing also creates opportunities to closely integrate optical communication systems with computing and switching silicon circuits [42]. Space-domain multiplexing (SDM) is also being proposed as a promising technology for enabling high-capacity transmissions with the scaling potential to meet future capacity demands [43–46].

While the aforementioned advancements in the optical network elements and systems have enabled the development of high bandwidth communication networks, there is an increasing need for making the network agile or flexible. Agility or flexibility in the next-generation optical networks enable it to dynamically scale based on demand, identify and locate impairments in the network automatically, be resilient to network disaster and cybersecurity attacks, and be more energy efficient. This requires software-defined optical networking at the physical layer with faster instrumentation systems for performing high-speed network signal analysis so that the network packets and/or the quality of transmission can be monitored rapidly to take automated corrective actions. Additionally, the increased bandwidths of opto-electronic, electro-optic and radio-frequency (RF) and microwave devices and systems also demand the need for faster and accurate instrumentation and measurement techniques.

1.2 Optical Performance Monitoring

Optical performance monitoring (OPM) is a set of measurements performed on optical signals at the intermediate network nodes or inside the receiver itself to estimate the performance of a transmission network such as optical signal to noise ratio (OSNR), bit error rate (BER),

Q-factor, etc. Network monitoring is the ability to measure the network infrastructure and resources in real-time. To enable robust, self-managed, and smart operation, OPM techniques should be able to accurately measure and rapidly reflect the physical states of network elements, optical paths, and the quality of propagating data signals. The ability to measure both the data quality and the physical state of the network path in real-time has traditionally been challenging due to the large number of possible impairments, the variety of data modulation formats, the variety of data rates, and the continuous growth and change of the network structure. Therefore, multiple impairments that cause the alarms must be isolated, localized, and compensated, requiring real-time monitoring and dynamic feedback control [47].

Optical performance monitoring techniques are employed to implement software-defined optical networks that are smart, robust, resilient, highly programmable or reconfigurable, and secure [48–54]. Rapid optical performance monitoring provides important information about mean time to repair and mean time to failure of network elements and can be used to ensure high Quality of Transmission (QoT). Important performance metrics, bit error rate, Q-factor, rise-fall times, eye-opening, and jitter, can be determined from the eye diagrams of the data signals [55]. Estimating these parameters, especially BER and Q-factor, quickly is important for active performance monitoring in high-speed networks to enable next-generation agile optical networking.

In Chapter 2, I give a brief introduction to the photonic time-stretch technology which enables real-time continuous and burst sampling of high-speed data by slowing down analog signals so that one or more low speed analog-to-digital converters (ADC) can capture long time segments of the signal continuously or in bursts. This technology is enables ultra-fast monitoring of the various parameters of the eye diagrams of high-speed signals as well as faster characterization of high bandwidth optical and electronic devices, all of which are described in the subsequent chapters.

1.3 High-Speed Signal Analysis

Bit-error rate is the ultimate metric for the quality of data transmission among all the optical performance monitoring measurements. The ability to perform high speed BER analysis of the optical signal through a network while in service can enable development of agile optical networks that are impairment aware and resilient to network disasters. Bit error rate testers (BERT) and equivalent-time sampling oscilloscopes are the most common techniques for analyzing high-speed signals. While these equipment are used for research and bench-top characterization of signals and testing the performance of optical network elements, they are not effective for in-service analysis of communication links. BERTs cannot be used for in-service signal analysis as it generates the test pattern data to be transmitted through the device under test. Equivalent-time sampling oscilloscopes are extremely slow, bulky and high power consuming. Real-time oscilloscopes and digitizers with high sampling rates cannot provide high resolution for the high frequency signals and are very power hungry. BER based optical performance monitoring techniques for enabling agile optical networks and for providing a feedback signal to a software-defined networking controller is expected to have a high-speed measurement time, high accuracy, low power consumption, and a compact form factor.

In Chapter 3, I introduce a time-stretch accelerated instrumentation system for performing ultra-fast BER analysis of 10 and 40 Gigabit/s non-return-to-zero (NRZ) on-off-keying (OOK) data from its eye diagrams with minimal hardware and power consumption compared to existing techniques [56]. The measurement time for producing eye diagrams of in-service signals and BER estimation for the time-stretch accelerated instrumentation system is ∼28 microseconds with an equivalent 2 Terabit/s burst mode processing capability.

1.4 Agile Optical Networks and Software-Defined Networking

The exponential traffic growth has led to unprecedented scaling of optical networks and has driven ever higher bit rates: from 100G to 400G. The demand for dynamic, cloud-based

services has created new challenges that require improved network agility, resilience to impairments and disasters, and automation in order for the network resources to become more readily consumable and elastic in their response to demand from higher network layers. Agile optical networking technologies enables telecommunication service providers to meet these challenges and significantly improve the delivery of cloud, mobile broadband and other bandwidth hungry services. Modern data center networks are also expected to scale, automate, and optimize different types of DCI network systems from intra-data center campus, enterprise to data center, disaster recovery, Metro DCI and long-haul data centers connecting globally. The exponentially increasing bandwidth requirements for various applications and highly dynamic services in mobile, cloud, intra-data center, 5G wireless, and Internet of Things (IoT) platforms needs agile optical networks.

Conventional dense wavelength division multiplexing (DWDM) technique has been used to establish rigid optical network connections employing a fixed modulation scheme such as OOK, quadrature phase-shift keying (QPSK), or differential phase-shift keying (DPSK) at fixed bit rate of up to 100 Gigabit/s with a fixed or flexible channel-channel spacing of 0.8 nm (100 GHz grid) or 0.4 nm (50 GHz grid) [57]. Optical switching has been used to provide limited reconfigurability when signals are being provisioned or restored. However,the use of active optical switching to address variations in network conditions and changing traffic behavior is yet to be adopted by service providers [58]. The availability of frequency tunable lasers also provide limited flexibility in terms of wavelength assignment to respective transponders [59]. This limited flexibility of current rigid optical networks makes it very challenging to upgrade or modify the network parameters to adapt to fluctuating network conditions and traffic patterns [60].

The energy consumption in optical networks is also increasing alarmingly as data networks grow in terms of traffic volume and end user data transaction size [61]. The exhaustion of scaling benefits from wavelength division multiplexing (WDM) and the slowing down of power efficiency of gains of RF and microwave components at higher frequencies have led to high thermal densities in central office equipment [62]. The engineering challenges of managing the power consumption in large switching centers and especially data centers are

increasingly becoming a matter of serious concern [63–65]. Many agile optical networking architectures and technologies have been proposed to improve energy efficiency of the network systems [66–68].

Software-defined networking (SDN) is a control framework that separates control and data planes to support programmability of network functions using well-defined interfaces [69]. SDN has become an important control and management framework for communication networks, especially in electrical circuit and packet switching systems. SDN protocols such as OpenFlow has recently been updated to include optical system compatibility [70]. Many approaches to extending SDN to support optical transport and elastic optical networks have also been proposed [71–75]. These proposed SDN extensions aims to enable a data center infrastructure that will enable automated, quality of service (QoS) aware, mapping of traffic flows into packet transport layers for intra and inter-data center links. In-service optical performance monitoring can provide the optical signal parameters such as BER as a feedback to the SDN control plane to dynamically take corrective actions based on impairments occurring in the network paths.

In Chapter 4, I discuss the various applications of TiSAP for in-service optical performance monitoring of agile optical networks. In particular, the experimental demonstrations performed in the testbed at the College of Optical Sciences at the University of Arizona for real-time feedback of the BER to the SDN control plane to switch wavelengths and routes to implement an agile network that recovers from disasters is presented. In addition, the characterization of various non-linear effects namely, amplified spontaneous emission and self phase modulation; burst-mode real-time, in-service, optical performance monitoring using eye diagrams on a 10 Gigabit/s NRZ OOK streaming video packets on a commercial optical network platform consisting of two Fujitsu Flashwave 9500 nodes [56]; and an ultra-fast time-stretch instantaneous frequency measurement receiver based on TiSAP which allows for both amplitude and frequency measurements for a wide bandwidth of 5-45 GHz are also discussed in this chapter [76].

1.5 Ultra-fast Device Characterization

The ever increasing demand for higher data bandwidth is pushing the communication industry to augment the operating frequency of components and systems. To implement very high-speed optical telecommunication systems and interconnects, it is necessary to develop wide-band devices such as photo-diodes (PD), electro-optic modulators (EOM), and radio frequency (RF) electronic circuits. The recent developments in the design of high performance photo diodes [77–79] and electro-optic modulators [80–82] have taken device bandwidths to well beyond 100 GHz. Performing accurate instrumentation and measurements of the various characteristics of electronic and optical devices/circuits/subsystems/systems/materials at these high bandwidths becomes very challenging. Longer test times for performing accurate measurements result in higher test costs during the production phase. To be able to perform faster testing of components is a key feature that is expected by the instrumentation and measurement community [83, 84]. With increasing frequencies, conventional test equipment cost, size, and power consumption also scale up proportionately.

In Chapter 5, I will introduce a new instrument for performing extremely fast measurements of frequency response of high bandwidth optical and electronic devices. This new approach combines an ultra-short mode-locked laser pulse used as excitation for the device under test and photonic time-stretch to achieve very fast impulse response measurements of the device under test, leading to its frequency response estimation. An extremely fast measurement time of 27 ns and an ultra-low intra-pulse jitter of 5.4 fs is reported for the proposed instrument [85, 86].

CHAPTER 2

Photonic Time-Stretch Technology

In this chapter, I introduce the photonic time-stretch technology, its performance, and review the existing research work that has been done. Real-time, high-throughput instrumentation at high bandwidth is an essential technology for studying high speed signals and rare events. Such instrumentation systems are employed for a wide range of medical, scientific, and industrial applications. The resolution of the analog-to-digital converters at high analog bandwidths limits the performance of such instrumentation and measurement systems. Photonic time-stretch technology slows down analog signals before digitization to enable real-time continuous and burst sampling of high-speed data by so that one or more low speed analog-to-digital converters can capture long time segments of the signal continuously or in bursts. The broadband signal of interest is modulated onto a pre-chirped optical pulse and stretched inside of a dispersion compensating fiber. Upon photo-detection, a slowed down copy of the original signal can be digitized and analyzed with lower speed, higher resolution electronic components.

Time-stretch technology has been used for implementing various high-throughput, real-time instruments developed for science, medicine and engineering applications. The bandwidth of a time-stretch system is limited by dispersion penalty and the electro-optic modulator (EOM) used. However, the bandwidth limit set by dispersion penalty can be mitigated by techniques such as phase diversity, coherent detection, and single side-band modulation. Additionally, the non-linearity in the time-stretch system can be mitigated by various techniques such as differential operation, back propagation and linearization.

2.1 Introduction

High-speed signals and high bandwidth devices pose many challenges to the instrumentation and measurement community as they are difficult to measure and characterize. One of the major limiting factor for high-speed signal analysis is the resolution limit at high frequencies for the analog-to-digital converters used in real-time oscilloscopes. An analog-to-digital converter or digitizer uses a sample and hold (S/H) circuit to sample a continuous analog signal at regular intervals of time based on an accurately generated clock signal and quantizes it to the nearest digital values by comparing the sampled analog voltage to a discrete set of digital levels. An electronic ADC, based on its architecture, can employ many S/H circuits, clock generators with different phases and duty cycles, quantizers, comparators, reference voltage circuits, and digital signal processing (DSP) for correcting distortions and mismatches. The sampling rate of the ADC has to be at least twice the largest frequency of the input analog signal, also called analog bandwidth, for adequately reproducing the analog signal from its digitized samples. This is called the Nyquist sampling criterion and is critical for high-resolution digitization. Therefore, to capture high-speed signals, very high sampling rates are required.

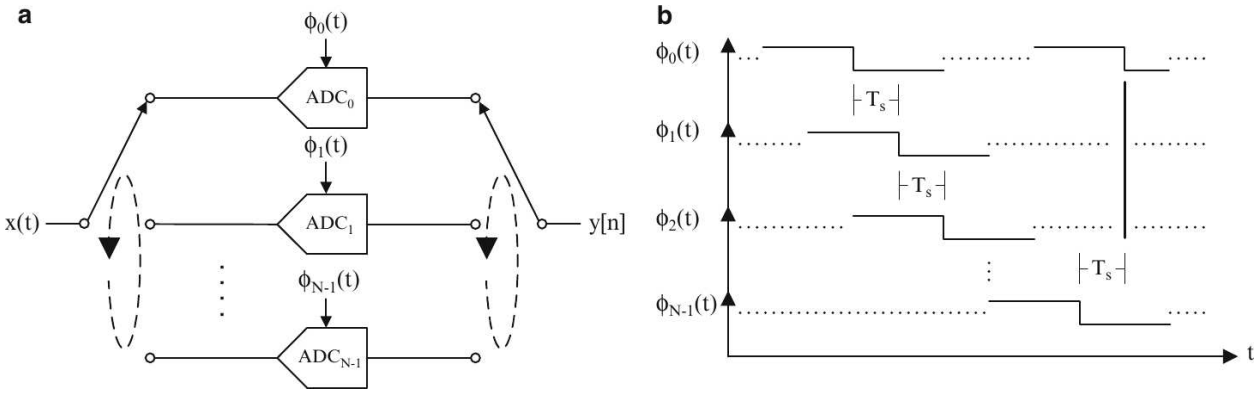

Figure 2.1: (a) Time-interleaved ADC, (b) Sampling edges of sub-ADC clocks. Courtesy of [87].

Time-interleaved digitizer architecture, as shown in Figure 2.1 employs many low bandwidth identical sub-ADCs operating concurrently to achieve very high sampling rates. If N

is the number of sub-ADCs used, each sub-ADC samples the same analog signal at a fraction (1/N) of the Nyquist rate. But each sub-ADC samples the same signal at a different time by using sampling clock signals that are offset in time by T_s [87]. The sub-ADC outputs are multiplexed to effectively result in a very high sampling rate of $N \times F_s$, where F_s is the sampling rate of a sub-ADC. Although time-interleaved digitizer architecture improves the sampling rate and resolution of ADCs, the mismatches across the individual sub-ADCs and the jitter associated with the clock distributed to all the sub-ADCs contributes to its resolution limits [88, 89].

Quantization noise in an ADC originates from the ambiguity in approximating and analog voltage to a fixed number of discrete levels. An N-bit ADC quantizes the full scale magnitude of the input analog signal to 2^N discrete levels, where N is the nominal number of bits of the ADC, also called resolution. For an ideal ADC, the quantization noise sets the upper limit to its signal-to-noise ratio (SNR) and is given by [90],

$$SNR(dB) = 6.02N + 1.76 \tag{2.1}$$

In real-world ADC devices, there are additional noise sources present. Thermal noise, shot noise, and aperture jitter noise due to the jitter in the sampling clock, contribute to reducing the SNR of the ADC. The non-linear effects in S/H circuits, amplifiers, mismatches among comparators, offsets errors, gain errors and timing mismatches in the clock distribution results in distortions in the digitized signal. Signal-to-noise-and-distortion-ratio (SNDR) is an important metric representing the ADC resolution that takes into account both the effects of noise and distortion and is given by,

$$SNDR(dB) = 20 \log \left(\frac{Signal}{Noise + Distortion} \right) \tag{2.2}$$

The combined effect of noise and distortion reduces the effective number of bits (ENOB) of the ADC, which is one of the most important metric of an ADC. ENOB is defined as,

$$ENOB = \frac{SNDR(dB) - 1.76}{6.02} \tag{2.3}$$

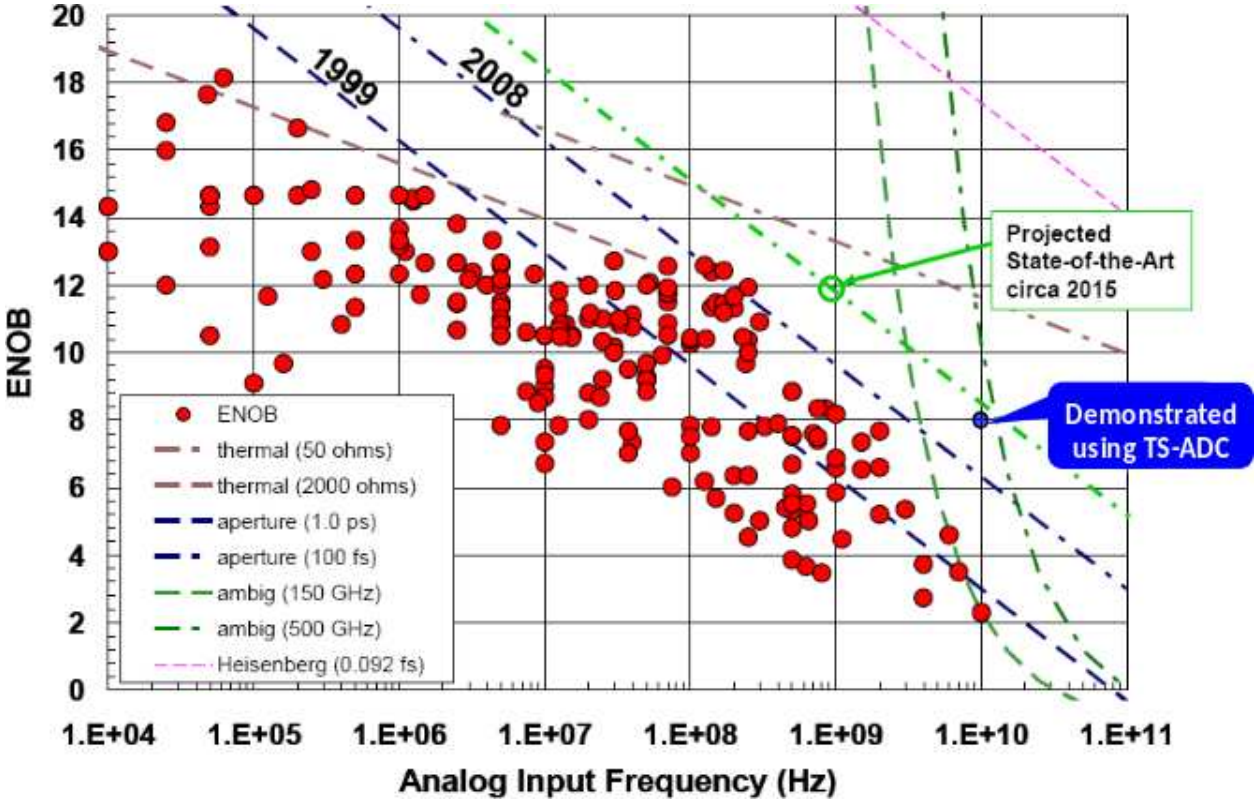

Figure 2.2: A modified Walden plot of ENOB vs analog bandwidth for the state-of-the-art ADCs. Courtesy of [90, 91]. The fundamental limits due to thermal noise, aperture jitter, and comparator ambiguity are indicated on the plot. The quantum limit due to Heisenberg's uncertainty is also plotted. The data point representing an ENOB $\geq$ 8 at 10 GHz by the latest implementation of photonic time-stretch ADC shows that it can help overcome the limitations of electronic ADCs [92, 93].

The ENOB of ADCs exhibits an inverse relationship with analog bandwidth due to the increasing effects of noise and distortion at higher frequencies. Figure 2.2 shows a modified Walden plot of ENOB vs analog bandwidth for the state-of-the-art ADCs [90, 91]. The fundamental limits due to thermal noise, aperture jitter, and comparator ambiguity are indicated on the plot. The quantum limit due to Heisenberg's uncertainty is also plotted. The data point representing an ENOB $\geq$ 8 at 10 GHz by the latest implementation of photonic time-stretch ADC shows that it can help overcome the limitations of electronic ADCs [92, 93] at higher analog bandwidths. High performance ADCs used in real-time

oscilloscopes that support very high analog bandwidths are also very power hungry and require expensive process technologies [90, 91, 94, 95].

In addition to resolution of the ADC, shorter test times for production-level testing of high bandwidth devices is also important. Longer test times result in higher test costs during the production phase. Vector network analyzers (VNA) are used to measure complex scattering parameters (S-parameter) of high bandwidth devices during production-level testing and also for post-production debugging and maintenance. Conventional VNAs utilize frequency sweeping employing a harmonic mixer to perform frequency domain measurements [96–98]. It becomes difficult, for example due to increased parasitic effects, to accurately measure the frequency responses of photo-diodes and electro-optic modulators using conventional swept-frequency technique as the bandwidths increase [99]. Also, swept-frequency techniques are slower which would increase test time.

Time domain network analysis (TDNA) has been used to measure frequency-domain network parameters [100, 101]. TDNA technique typically applies the test stimulus (a voltage step signal) to the device under test periodically for many cycles and uses an equivalent-time digitizer (or digital sampling oscilloscope) to sample the response every cycle. The sampling rate of the digitizer is very low (typically 100 kHz to 10 MHz) and the signal waveform is reconstructed digitally provided the signal analyzed is periodic or clock synchronous. Equivalent-time sampling oscilloscopes need several cycles of sampled data to be able to digitally reconstruct the original signal with high fidelity followed by digital signal processing to analyze the signal to measure the network parameters of the device under test (DUT). Large signal network analyzers (LSNA) are widely used to perform time domain non-linear device characterization [102, 103]. LSNAs down-convert high frequency signals to intermediate frequency (IF) using harmonic sampling followed by digitization to yield time domain data. However, the microwave signal to be analyzed using LSNA has to be periodic and its period must be known. Timing jitter and time base distortion significantly affects the performance of TDNA techniques [101, 104, 105]. In addition, TDNA techniques are also slower compared to real-time digitizers and suffer in terms of accuracy to capture dynamics that occur at nanosecond level.

Network analyzers are also used for measuring the complex permittivity of different materials which has paved way for new non-invasive bio-medical applications [106–109]. But the higher measurement time of both the conventional frequency-domain and time-domain network analyzers would render them ineffective for high throughput applications, such as real-time particle flow analysis for biological sample analysis. Such high-throughput applications demand very fast frequency dependent permittivity measurement techniques.

Photonic time-stretch is a technology that can fill the functional and performance gaps of both real-time digitizers, equivalent-time sampling oscilloscopes, and network analyzers.

2.2 Photonic Time-Stretch

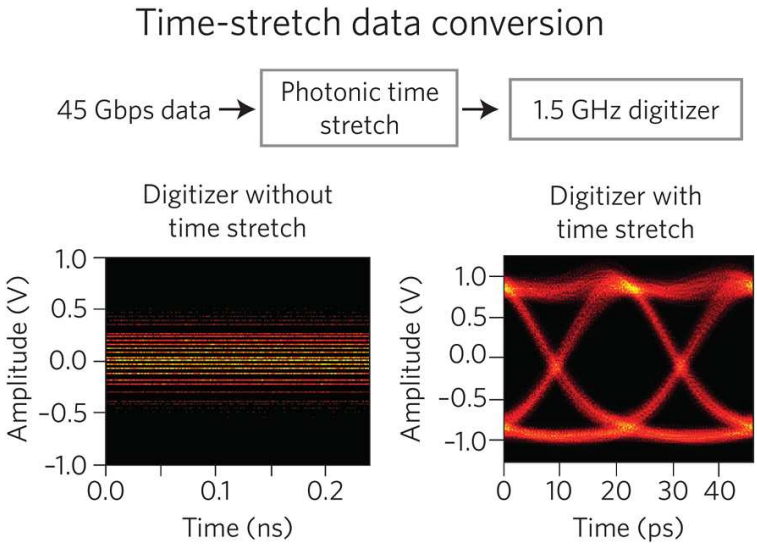

Figure 2.3: Photonic time-stretch linearly stretches the signal in time reducing its analog bandwidth significantly, allowing the analysis of ultra-fast data using slow but high resolution ADCs way below the required Nyquist rate. 45 Gigabit/s NRZ OOK data is analyzed using a digitizer with 1.5 GHz analog bandwidth directly and after photonic time-stretch. Adapted from [110].

Time-stretch technology is a fundamentally different approach to broadband digital receiver technology. Instead of increasing the speed of back-end ADCs and DSPs to keep up with ever accelerating data rates, time-stretch slows down incoming signals before digitization [110–

113]. This reduces the analog bandwidth of the signal much below the Nyquist bandwidth of the ADCs. By employing this technique, lower speed, higher resolution, more energy efficient ADCs and DSPs can be used to capture and process full wide-band signals in real-time. As shown in Figure 2.3, time-stretch technology was used to capture high-speed data using a much lower speed digitizer. The front-end time-stretcher effectively boosts the performance of the back-end ADC and DSP much more significantly and efficiently than can purely electronic techniques alone. In addition, the time-stretch architecture scales with ADC and DSP technology, continually improving in resolution and speed as the electronic back-end technology progresses.

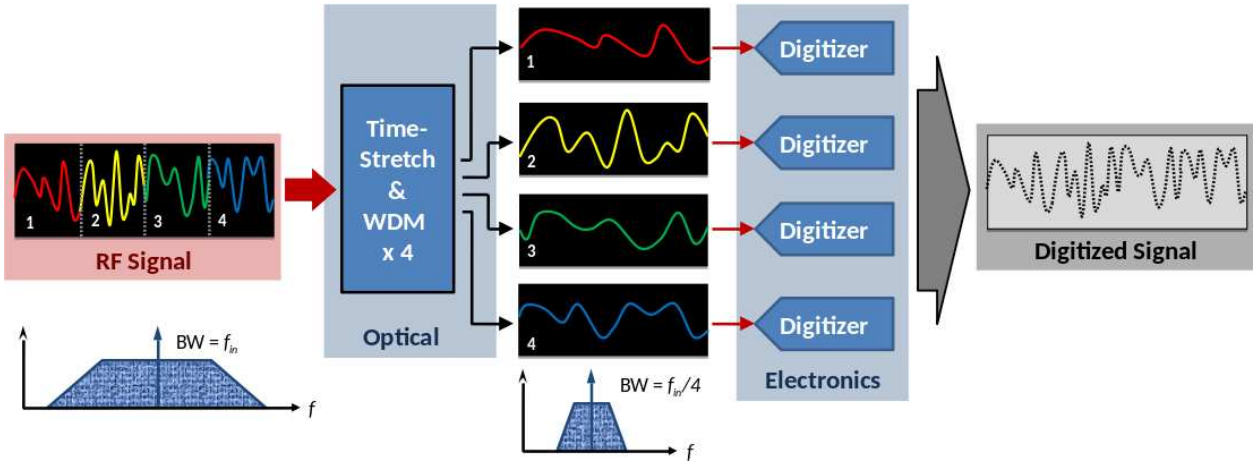

Figure 2.4: Conceptual diagram of the continuous-time photonic time-stretch ADC. Courtesy of [113].

Photonic time-stretch ADC (TS-ADC) uses an optical front-end to slow down analog signals before digitization by low speed, high resolution ADCs that are used concurrently [111, 112, 114, 115]. As shown in Figure 2.4, an optical front-end stretches and segments the analog input signal using a wavelength division multiplexer into four wavelengths. The stretched segments are digitized by the ADCs and the digitized segments are combined using DSP to obtain a digital copy of the analog signal.

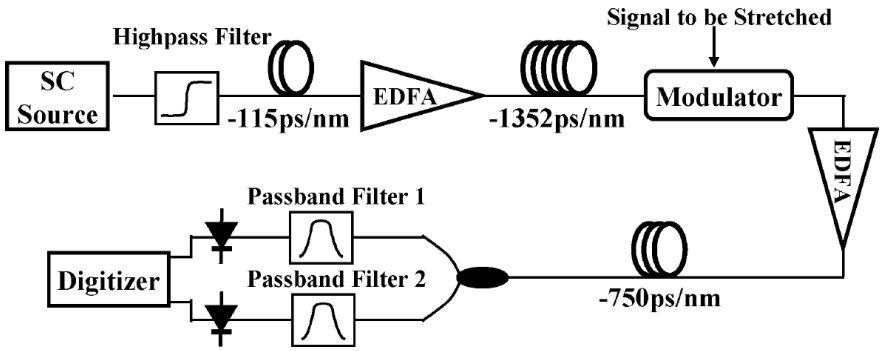

Figure 2.5: An implementation of two-channel time-stretch ADC. SC: Supercontinuum; EDFA: Erbium-Doped Fiber Amplifier; High pass filter: 1570 nm above; Passband filter 1: 1576 nm with 20-nm bandwidth; Passband filter 2: 1594 nm with 20-nm bandwidth. Courtesy of [116].

An implementation of a two-channel time-stretch ADC employing virtual gating [116] is shown in Figure 2.5. The optical front-end for this implementation consists of a supercontinuum source using a mode-locked laser, dispersive medium to chirp the pulse prior to transmitting to an intensity modulator, such as a Mach-Zehnder modulator which also receives the electrical analog signal to be stretched. The electro-optic modulator modulates the electrical signal onto the chirped laser pulses which undergoes amplification and are transmitted through another dispersive medium which stretches the laser pulses as well as the electrical signal superimposed onto it. The stretched optical signals are power-split using a 3-dB power splitter and the two channels are filtered by band-pass filters. In a TS-ADC system with more channels, a wavelength division multiplexer would be employed to avoid power by using a splitter. The two channels are subsequently photo-detected and digitized concurrently by two channels of a real-time oscilloscope. The digitized samples from both channels are combined using DSP.

The effective aperture jitter is reduced by the slowing down of the analog signals in TS-ADC. Since oversampling the signal reduces the quantization noise power, TS-ADC can overstretch the analog signals to increase sampling rates and thereby improve resolution. TS-ADCs with an ENOB of 7.2 GHz at 10 GHz analog bandwidth have been demonstrated [117]. An extremely high sampling rate of 10 Tera-samples/s was achieved by another implemen-

tation [118]. The record for the highest resolution ADC performance at 10 GHz analog bandwidth has been set by TS-ADC implementations with an ENOB of 8 [92] and ≥ 8 [93], which can be seen in the Walden plot shown in Figure 2.2.

2.3 Time Stretch Enhanced Recording Oscilloscope

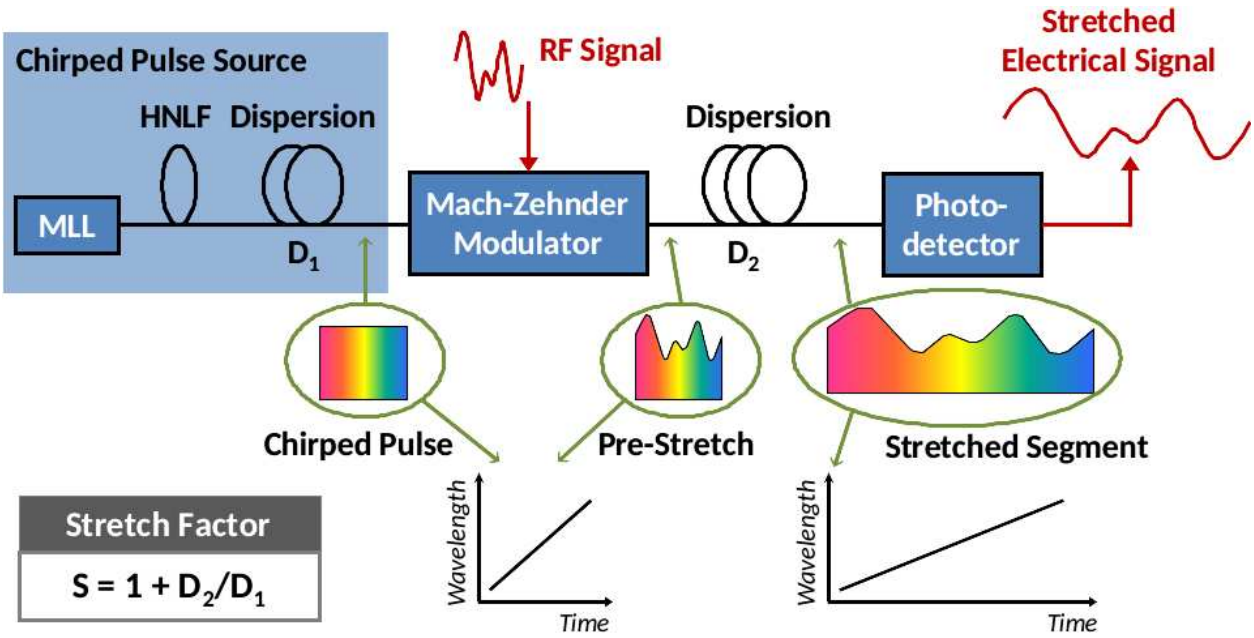

Figure 2.6: Time-stretch enhanced recording oscilloscope. MLL: Mode-locked laser; HNLF: Highly non-linear fiber; PD: Photo-detector. Courtesy of [113].

A single-channel implementation of TS-ADC enables it to be used in equivalent-time sampling mode but with much superior sampling throughput than a conventional equivalent-time sampling oscilloscope. Such a single channel implementation is called time-stretch enhanced recording (TiSER) oscilloscope [113, 119–121]. TiSER is implemented using commercial-off-the-shelf fiber optic components. It consists of a chirped optical pulse source, an electro-optic modulator which receives the RF signal as input, a dispersive medium to stretch the modulated optical pulse, a photo-detector, and a digitizer and DSP (not shown in the figure). The optical source is typically a 1550 nm mode-locked laser (MLL) that produces ultra-short (< 1 ps in length) optical supercontinuum pulses followed by a group velocity dispersive

(GVD) medium such as a dispersion compensating fiber (DCF) or chirped fiber Bragg grating (CFBG), or a chromo-modal dispersion device (CMD) [110, 122]. A supercontinuum pulse is generated using a highly non-linear fiber (HNLF) which results in spectral broadening of a high power narrow linewidth laser pulse through the non-linear interactions such as self-phase modulation, stimulated Raman scattering, modulation instability, etc [123, 124].

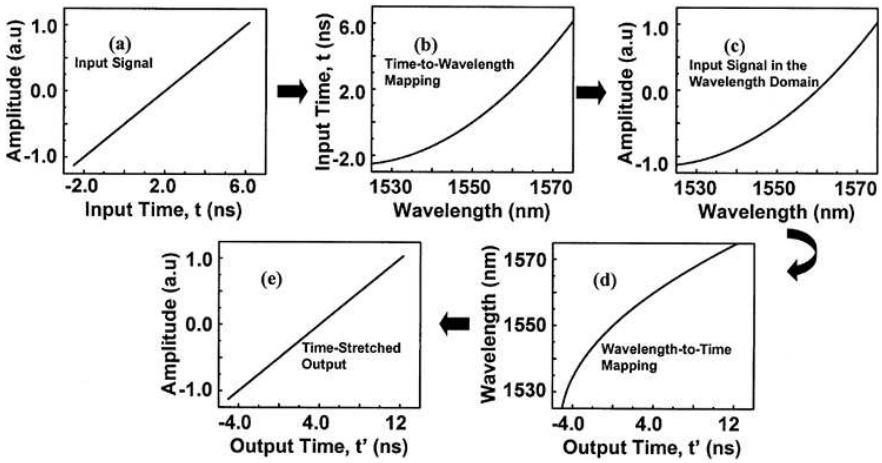

Figure 2.7: A graphical representation of the time–wavelength transformation. (a) Input signal. (b) Time–wavelength transfer function associated with nonlinear dispersion in the first dispersive fiber. (c) Input signal in the wavelength domain after time-to-wavelength mapping. (d) Wavelength–time transfer function of the second dispersive fiber. (e) Output time-stretched signal. The time-stretch process is linear (uniform) despite the non-linear fiber dispersion. Courtesy of [114].

The supercontinuum pulse is chirped by propagation through a dispersive medium such as a DCF fiber with a group velocity dispersion value of D_1. This is also referred to as pre-stretching. The chirping of the pulse results in time-to-wavelength mapping in the pre-stretched pulse since different wavelengths propagate with velocities due to GVD [114, 125]. The instantaneous frequency of the chirped pulse varies with time over a time window (aperture) that represents the sampling window for single-shot measurements. The analog RF input to be analyzed is modulated onto this chirped pulse using a Mach-Zehnder modulator, which maps the time-scale of the input signal into the optical frequency. The modulated chirped optical pulse, with the analog input signal superimposed on it, is further stretched by

propagation through a second DCF fiber with a GVD value of D_2. This time-stretch process in the second dispersive fiber results in wavelength-to-time mapping. Although the time-wavelength mapping process in D_1 is not linear and has a positive concavity, the time-stretch process is linear (uniform) due to the opposite curvature of the wavelength-time mapping in the second dispersive fiber as depicted in Figure 2.7.

The time-stretched signal from the output of the second dispersive fiber is band-pass filtered using a WDM (not shown in the figure) with 18 nm bandwidth and then applied to a photo-detector. Upon photo-detection using a photo-diode (PD), a slowed down copy of the original high bandwidth signal can be digitized in real-time bursts and analyzed using lower speed, higher resolution ADC and DSP. The stretch factor of TiSER is given by,

$$\begin{aligned} Stretch-factor, M &= \frac{Temporal\ pulse\ width\ after\ time-stretch}{Temporal\ pulse\ width\ after\ pre-stretch} \\ &= \frac{D_1+D_2}{D_1} = 1+\frac{D_2}{D_1} \end{aligned} \tag{2.4}$$

The equivalent real-time burst sampling (RBS) rate of TiSER, $f_{s,TiSER}$, is therefore given by [119],

$$\begin{aligned} f_{s,TiSER} &= M \times f_{s,ADC} \\ &= \left(1+\frac{D_2}{D_1}\right) \times f_{s,ADC} \end{aligned} \tag{2.5}$$

where $f_{s,ADC}$ is the sampling rate of the back-end ADC.

2.3.1 Real-time Burst Sampling

Conventional electronic digitizers can be broadly classified into equivalent-time digitizers or sampling oscilloscopes and real-time digitizers such as a real-time oscilloscope. The operation of a sampling oscilloscope relies on the periodic/repetitive or clock synchronous nature of the signals to reconstruct them in time after collecting a lot of samples. A sampling oscilloscope is typically operated at sampling frequencies less than or up to 10 MHz. After collecting many sample points over a long time, the original signal can be digitally reconstructed, as

shown in Figure 2.8(a). Although sampling oscilloscopes are available for operation above 100 GHz, this technique is incapable of capturing non-repetitive signals or single-event dynamics within a repetitive signal which occur at rates faster than a few MHz. Real-time digitizers on the other hand continually sample at regular intervals, but have limited analog bandwidths as shown in Figure 2.8(b). Even though the real-time oscilloscopes commercially available today can have very high analog bandwidths of over 80 GHz, the effective number of bits reduce significantly as frequencies increase [90, 91].

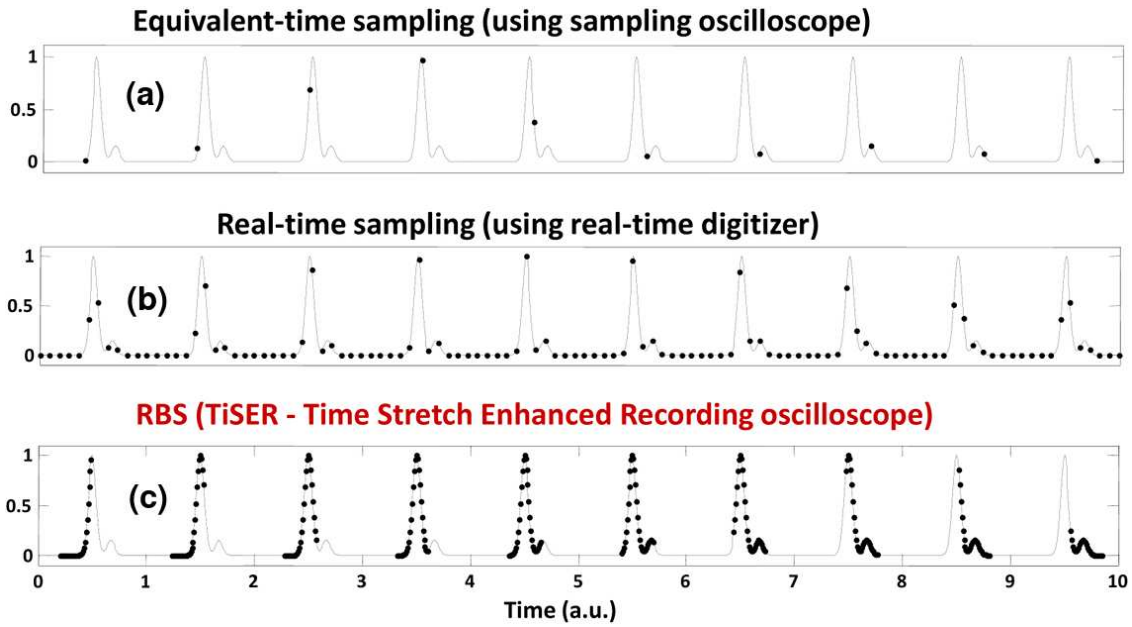

Figure 2.8: A comparison of different sampling techniques. (a) An equivalent-time oscilloscope samples signals at slow rates and can only reproduce signals that either clock synchronous or repetitive. (b) A real-time digitizer samples continuously at regular intervals but has limited bandwidth and resolution. (c) TiSER oscilloscope can capture very high speed segments in real-time bursts and quickly reproduce them on equivalent time scales. Courtesy of [119].

In contrast with an equivalent-time oscilloscope, which captures only a single sample at a time, TiSER captures many segments of the analog signal within the real-time burst window or the aperture time. TiSER can capture ultra-fast non-repetitive dynamics that occur within the real-time burst window as shown in Figure 2.8(c). Ultra-fast events cannot

be observed by a sampling oscilloscope because of its lack of real-time capture capability, or by a real-time digitizer because of its limited bandwidth and resolution. TiSER bridges the performance gap between sampling oscilloscopes and real-time digitizers

2.3.2 Eye Diagram Measurements using TiSER

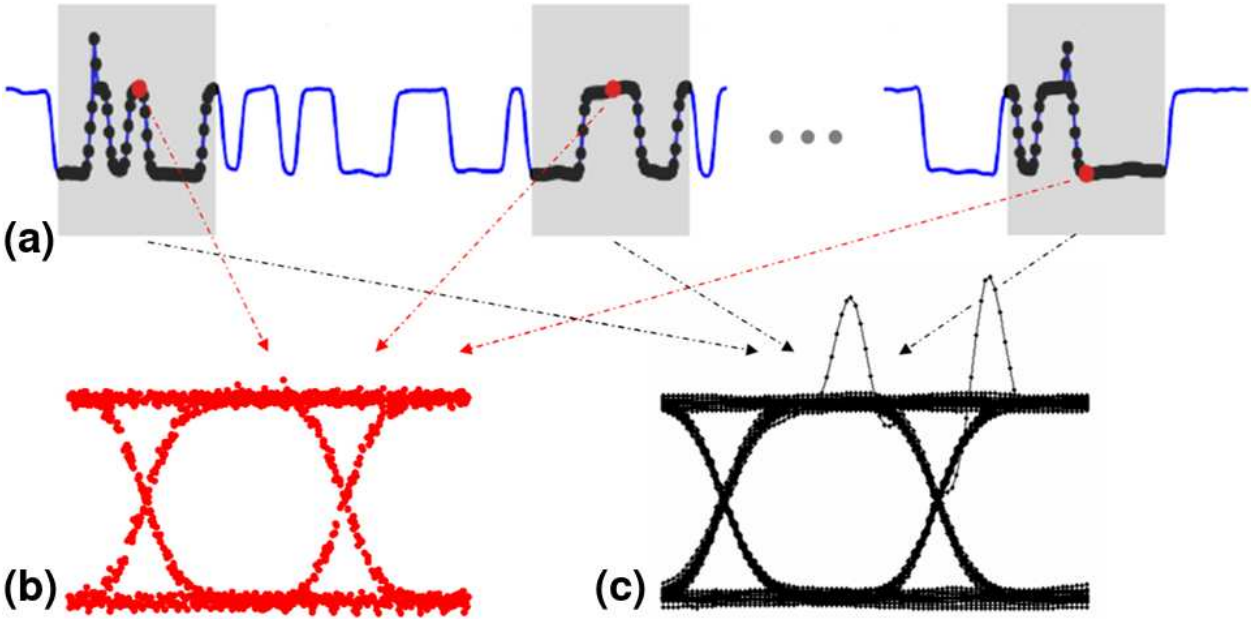

Figure 2.9: Comparison of eye diagram capture by sampling oscilloscope and TiSER. (a) Serial digital data waveform (in blue) can be captured by real-time digitizers at lower data rates. (b) Eye diagram captured by a sampling oscilloscope. (c) Eye diagram captured by TiSER oscilloscope, which can potentially capture non-repetitive dynamics such as spikes. Courtesy of [119].

An eye diagram is a way to represent the effect of amplitude noise and timing jitter present in data communication signals. In an eye diagram, many data voltage levels and edge transitions are superimposed over one unit interval (UI) range. The vertical eye opening indicates the margin for bit errors due to noise and the horizontal eye opening of the eye indicates the margin for timing errors due to an imperfectly recovered clock or jitter in the data. An eye diagram provides an overall statistical qualitative view of the quality of the signal under test [126]. This is vital information about the signal integrity in a serial data

communication link. Measurement of jitter using pseudorandom data patterns required for ensuring very high BER (10^{-12}) consumes a lot of time [127]. Eye diagram measurements using BER tester can take hours to more than a day to collect all the data needed for ensuring very high confidence levels in the testing. The eye diagram analysis can be done faster by statistically analyzing the eyes from a sampling oscilloscope. But a sampling scope also is very slow as only a fraction of the recorded samples lie close to the zero crossings for jitter measurements as shown in Figure 2.9.

TiSER on the other hand captures a continuous set of samples within the aperture time. The signal amplitudes within sample-to-sample time intervals can be obtained by interpolation since the samples are connected. The acquisition time for TiSER is three to four orders of magnitude better than the fastest sampling oscilloscopes. As shown in Figure 2.9, TiSER can also capture ultra-fast rare events and their dynamics in high data rate communication signals which is impossible using sampling oscilloscopes due to their limited sampling rates. TiSER has demonstrated very high sampling throughput that is two orders of magnitude better than the state-of-the-art sampling (equivalent-time) oscilloscopes [119–121, 128].

2.4 Measurement Jitter

Clock jitter or aperture uncertainty error generated by the clock source is the main limiting factor of resolution in a high-speed ADCs [90,91,94]. Clock jitter causes an inaccuracy in the sampling time window of the digitizer resulting in an inaccurately sampled voltage as shown in Figure 2.10. This sampling inaccuracy gets worse at higher frequencies of the sampled signal. The clock jitter limited signal-to-noise ratio (SNR_{jitter}) of a high-speed ADC for a root mean square (rms) jitter, τ_j has been statistically estimated to be [90]:

$$SNR_{jitter}(dB) = -20\log(2\pi f_{RF}\tau_j) \equiv \frac{1}{8\pi^2 f_{RF}^2 \tau_j^2} \tag{2.6}$$

where f_{RF} is the analog bandwidth of the signal.

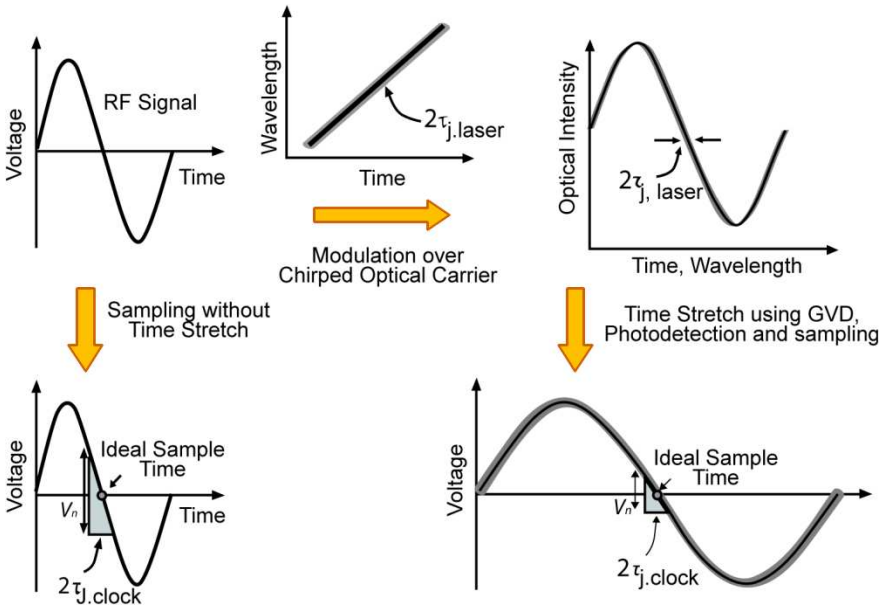

Figure 2.10: Comparison of the sampling a signal with and without time-stretch and its impact on clock aperture jitter. When time-stretch technique is used, the noise due to clock jitter becomes insignificant, and noise due to the mode-locked laser jitter dominates, which is typically much less than the electronic clock jitter (V_n represents the noise voltage). Courtesy of [113].

In an electronic ADC, the noise added due to sampling jitter increases with signal frequency as it is proportional to the square of the signal frequency and the clock jitter, based on equation 2.6. As can be seen from Figure 2.10, for faster signals, even a small amount of clock jitter can result in a significant error in the sampled voltage. In the case of time-stretch, the effective signal frequency is reduced, which in turn decreases the effect of electronic clock jitter by the stretch factor.

In a time-stretch system, there are two sources of timing jitters: inter-pulse optical jitter in the mode-locked laser and electronic jitter in the back-end ADC sampling clock. This laser timing jitter in the time-stretch system has the same effect as the clock jitter in ADCs [95]. But mode-locked lasers have much lower timing jitter than electronic clocks. A fiber laser with only 70 as (attosecond) timing jitter has recently been reported [129]. The best clock jitter achieved in state-of-the-art electronic ADCs are of the order of 110-fs [130],

which is more than three orders of magnitude compared to MLL laser jitter. Therefore, the noise limitation due to clock sampling jitter in high-speed ADCs can clearly be overcome by applying time-stretch. Since time-stretching of the signal reduces the effective signal frequency by the stretch-factor, M, the noise added to the system due to electronic jitter is reduced by a factor of M^2. The total effective jitter for a time-stretch system can be then be expressed as [114]:

$$\tau_{j,eff} = \sqrt{\tau_{j,laser}^2 + \left(\frac{\tau_{j,clock}}{M}\right)^2} \tag{2.7}$$

For high stretch factors, the MLL timing jitter dominates as the electronic ADC jitter is scaled down by the reciprocal of the stretch factor ($\tau_{j,laser}^2 \gg \left(\frac{\tau_{j,clock}}{M}\right)^2$) resulting in the effective timing jitter given by,

$$\tau_{j,eff} \approx \tau_{j,laser} \tag{2.8}$$

If a single-shot time-stretch measurement is performed using only one laser pulse, the inter-pulse optical jitter in the MLL is absent. Therefore from equation 2.7, the effective intra-pulse jitter for single-shot time-stretch instrumentation is given by:

$$\tau_{j,single-shot} = \left(\frac{\tau_{j,clock}}{M}\right) \tag{2.9}$$

Therefore, single-shot measurements using time-stretch are much more accurate than without time-stretch as time-stretch scales down the clock jitter in ADC by the reciprocal of the stretch factor. This enables very accurate single-shot time-domain measurements compared to conventional real-time and equivalent-time oscilloscopes and network analyzers, where the jitter added by the instrument has to be very accurately estimated and corrected.

2.5 Non-linearity

Time-stretch pre-processor is analogous to an analog optical link consisting of an optical source, an electro-optic modulator making up the transmitter, an optical fiber link, and

a receiver consisting of a photo-diode and back-end electronics. Time-stretch techniques also suffer from distortion due to non-linearity, like in any analog communication links. The sources of these distortions include non-linear transfer function of the electro-optic modulator, additional non-linearity when the modulation sidebands are dispersed during time-stretch, saturation at the photo-diode, optical non-linearities, and non-linearities of back-end electronics.

When an optical carrier is modulated by an electrical signal using an intensity modulator, it results in double sideband (DSB) modulation with the optical carrier and the upper and lower sidebands at the fundamental frequency. At the photo-diode these sidebands interfere with the optical carrier and with each other to generate the electrical signal and its harmonics. For an EOM biased at the quadrature point and without dispersion, all even-order harmonic components would cancel each other. However, either due to bias fluctuations or dispersion, the even-order harmonic components do not cancel each other due to asymmetry in the phase and amplitudes of sidebands introduced by dispersion. These distortion components can be suppressed by either differential or arcsine operations [131], or back-propagation algorithm [132, 133], and/or broadband linearization [134–136].

The non-linear effects in photo-diodes and electronics are important for high dynamic range applications. The non-linear squaring of the electric fields at the back-end photo-diode prior to the ADC also results in addition of distortions to the measured signal. To reduce photo-diode non-linearity, the optical input power must be significantly lower than the saturation power of the photo-diode. The second-order distortions added by the photo-detector can be suppressed by using differential operation. The odd-order components can be digitally suppressed using DSP or tunable electronic hardware [137, 138]. The optical non-linearities can be minimized by keeping the optical power levels below the non-linear threshold. If long dispersive fibers are used, the optical power at the output of the second dispersive fiber might not have enough SNR. In such cases, distributed Raman amplification has been employed successfully to improve the SNR significantly [139, 140].

Finite mismatches between the dispersion coefficients (D_1 and D_2) of the two dispersive fibers used can cause the stretch factor to be wavelength dependent and therefore, time

dependent due to the wavelength-time mapping, which results in a time-warping distortion. Optical non-linearity in the fiber can also be a source of time-warp distortion. Self-phase modulation effects in the first dispersive fiber with group velocity dispersion can distort the desired wavelength-time mapping resulting in time-warp distortions. Additionally, for the continuous-time TS-ADC implementation, the stitching of the signal segments from parallel wavelength channels requires them to be properly aligned in time, which is very challenging to achieve using optical hardware. Fortunately, all the time-warp effects and the channel misalignment issues are static over time and deterministic and has been corrected digitally after characterizing it [117].

2.6 Power Scaling of Time-Stretch ADC

Even though the bandwidth of analog circuits have improved with CMOS technology scaling, power dissipation for the same functionality does not always scale because of lower intrinsic gains in shorter channel CMOS transistors [141]. Most improvements in power efficiency of analog circuits can be attributed to architectural improvements and scaled voltages. Thermal noise $\left(\frac{kT}{C}\right)$ limitations prevent arbitrary reductions in analog full-scale voltages of ADCs. Therefore, technology scaling has not significantly resulted in decreased analog power dissipation, and increased speed of digital circuits has allowed extensive use of digital correction and calibration techniques, which have led to significant improvements in performance. The most commonly used figure of merit (FOM) for ADC efficiency is the energy required per conversion step and is defined as,

$$FOM = \frac{P_{diss}}{2^{ENOB} \times 2 \times ERBW} \tag{2.10}$$

where P_{diss} is the power dissipation, ENOB is the effective number of bits, and ERBW is the effective resolution bandwidth of the ADC, which defined as the frequency at which SNDR of the ADC degrades by 3-dB [90].

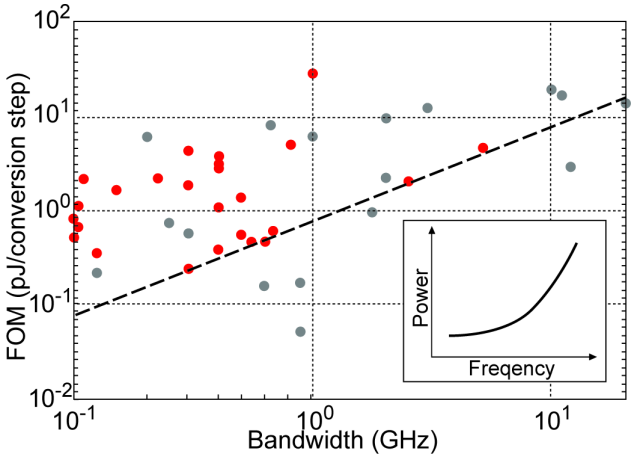

Figure 2.11: Energy per conversion step versus performance for state-of-the-art high-speed ADCs with moderate to high resolution. Courtesy of [95].

The plot in Figure 2.11 clearly shows that above 100-MHz, energy per conversion step for the best ADCs increases rapidly with bandwidth. It has been estimated that the power dissipation in high-speed ADCs increases quadratically with sampling frequency with Nyquist rate sampling [95]. This work also shows that with time-stretch technology, one can obtain linear power scaling of future ADCs to much higher frequencies.

As discussed in Section 2.4, in high-speed ADCs, aperture jitter is a significant source of noise and time-stretch reduces the effective sampling jitter in the system. This makes the time-stretch digitizer architecture very well suited for high frequency applications, where aperture jitter is the dominant source of noise. Additionally, when employing time-stretch, none of the back-end digitizers "see" the original high frequency signal since the signal frequency scales down upon stretching. Time-stretch therefore, also allows for the use of low power, high resolution, slow ADCs with much lesser power dissipation. As a result, the power scales linearly with the sampling frequency of the ADC.

2.7 Dispersion Penalty

In the conventional TS-ADC, when double-sideband modulation is used to modulate radio frequency signals onto the optical pre-chirped carrier, a frequency-fading phenomenon due

to dispersion occurs [114]. This is due to the fact that dispersion introduces different phase shifts to the sidebands and leads to constructive and destructive interference beating of the sidebands with the carrier at the photo-detector as illustrated in Figure 2.12(a). The destructive interference results in nulls in the RF transfer function of the time-stretch system as shown in Figure 2.12(b), which is a simulation of the effect without any attenuation. The overall effect known as dispersion penalty is to limit the 3-dB RF bandwidth of time-stretch system, which is given by [142],

$$\Delta f = \sqrt{\frac{1}{8\pi|\beta_2|L_1}} \tag{2.11}$$

where β_2 is the GVD parameter and L_1 is the length of the first dispersive fiber.

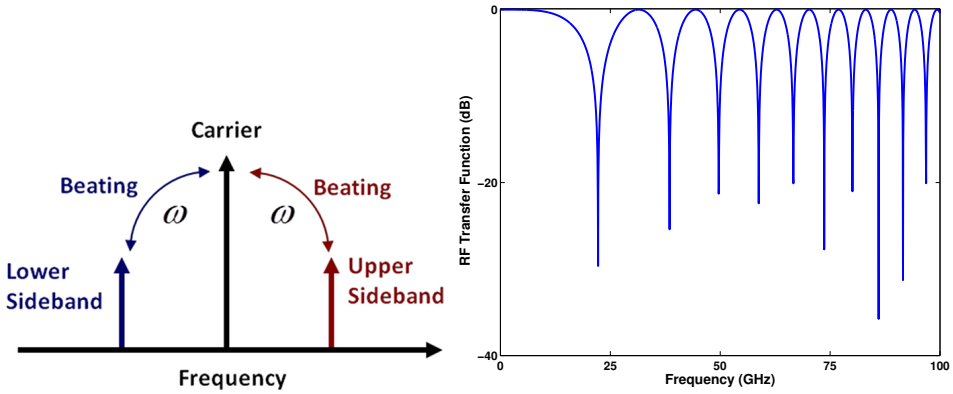

(a) (b)

Figure 2.12: (a) Destructive interference caused by the beating of the optical carrier with the upper and lower sidebands at the photo-detector results in dispersion penalty. Courtesy of [143]. (b) A simulation of the effect of dispersion penalty on the RF transfer function assuming no attenuation in the fiber.

The 3-dB RF bandwidth is proportional to the inverse square root of the initial dispersion fiber length. Therefore, for the same stretch factor, the 3-dB RF bandwidth decreases with time aperture resulting in a trade-off between between the RF bandwidth and the aperture length. This time-bandwidth product (TBP) increase with optical bandwidth. There are various techniques to overcome the effects of dispersion penalty and extend the bandwidth of the time-stretch based instrumentation systems. Three such techniques are phase diversity,

single sideband modulation, and coherent detection.

2.7.1 Phase Diversity

The dispersive fading phenomenon seen in the RF transfer function of the time-stretch instrumentation system is similar to the channel fading effects in wireless communication due multipath propagation or weather (particularly rain), or shadowing from obstacles [144]. The effects of channel fading in wireless systems can be combated by spatial diversity employing multiple antennae. To overcome RF fading in time-stretch systems, phase diversity employing a single-arm dual-output Mach-Zehnder (MZ) modulator is used [145], as shown in Figure 2.13(a). The fading in time-stretch systems being deterministic allows for very simplified system design and signal processing for employing phase diversity, unlike channel fading in wireless communication which is stochastic in nature.

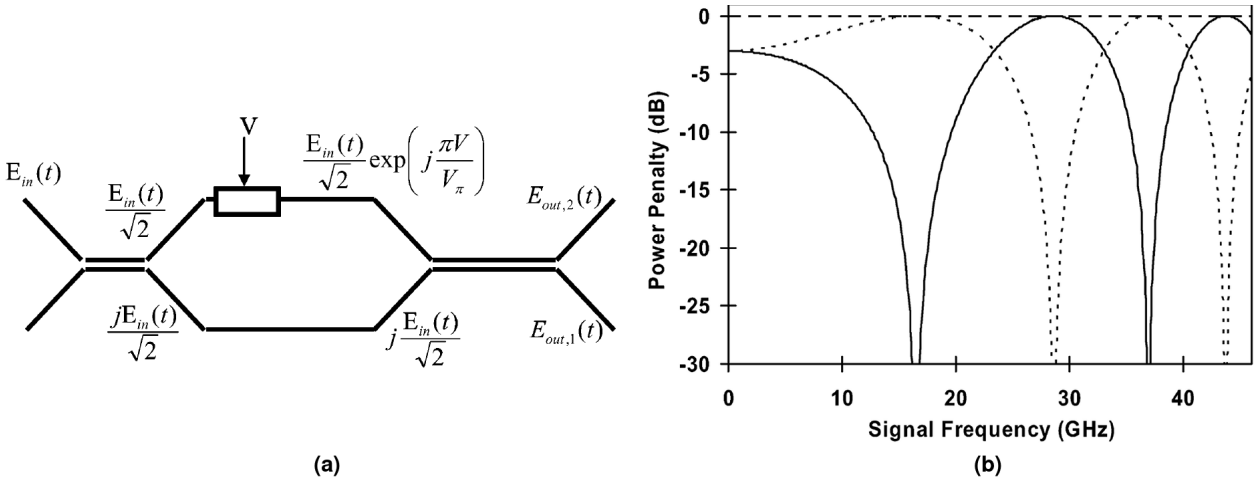

Figure 2.13: (a) Single-arm dual-output Mach-Zehnder modulator. (b) Calculated dispersion penalty for two outputs of the modulator. Courtesy of [145].

The output optical fields $E_{out,1}$ and $E_{out,2}$ at the two output ports of the single-arm dual-output modulator are given by,

$$E_{out,1} = jE_{in}exp\left(j\frac{\pi V}{2V_\pi}\right)cos\left(\frac{\pi V}{2V_\pi}\right) \tag{2.12}$$

and

$$E_{out,2} = jE_{in}exp\left(j\frac{\pi V}{2V_\pi}\right) sin\left(\frac{\pi V}{2V_\pi}\right) \tag{2.13}$$

where E_{in} is the input optical field.

The optical signals from the two output ports of the MZ modulator differ in phase by 90° in the phase and therefore their fading characteristics will also be different as shown in Figure 2.13(b). The RF power spectrum of the two outputs is given by [114, 142],

$$H_1(f) = cos^2\left(\phi_{DIP} - \frac{\pi}{4}\right) \tag{2.14}$$

and

$$H_2(f) = cos^2\left(\phi_{DIP} + \frac{\pi}{4}\right) \tag{2.15}$$

where the dispersion induced phase (DIP) is given by,

$$\phi_{DIP} = \frac{2\pi^2\beta_2 L_2 f^2}{M} \tag{2.16}$$

where f is the signal frequency, L_2 is the length of the second dispersion compensating fiber (D_2), β_2 is the the fiber group velocity dispersion parameter, and $M = \left(1 + \frac{L_2}{L_1}\right)$ is the stretch factor where L_1 is the length of the first dispersion compensating fiber (D_1).

As shown in Figure 2.13(b), when the frequency response at one of the output port experiences a minimum or a null, the other output port experiences a maximum. The dispersive RF fading effect can be overcome by exploiting this complementary diversity behavior when the outputs from both the ports are captured. Analytically,

$$H_1(f) + H_2(f) = cos^2\left(\phi_{DIP} - \frac{\pi}{4}\right) + cos^2\left(\phi_{DIP} + \frac{\pi}{4}\right) = 1 \tag{2.17}$$

which is free of any fading.

Antennae combining algorithms that are utilized to maximize the signal-to-noise ratio of the signal in a wireless system is applied to combine the outputs from the two ports. The maximum ratio combining (MRC) algorithm can be used to add the outputs from the two MZ modulator ports with a weight proportional to the voltage SNR of the channel. The

weights used for phase diversity time-stretch system are such that,

$$W_1 = cos\left(\phi_{DIP} - \frac{\pi}{4}\right) \tag{2.18}$$

and

$$W_2 = cos\left(\phi_{DIP} + \frac{\pi}{4}\right) \tag{2.19}$$

such that,

$$W_1 cos\left(\phi_{DIP} - \frac{\pi}{4}\right) + W_2 cos\left(\phi_{DIP} + \frac{\pi}{4}\right) = 1 \tag{2.20}$$

The complementary characteristics of the two output ports ensure that the combined output is independent of frequency, thereby eliminating the RF fading effects. Phase diversity with maximum ratio combining successfully demonstrated the digitization of a 26 GHz signal in a time-stretch system which had a dispersion null at 26 GHz [145].

2.7.2 Single Side-band Modulation

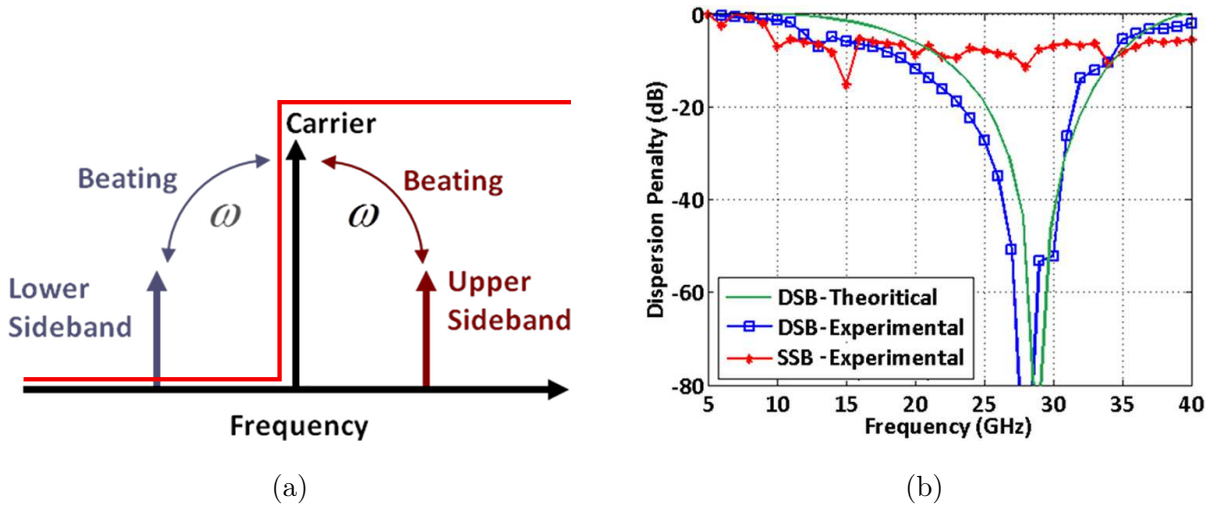

(a) (b)

Figure 2.14: (a) Single sideband modulation implemented using a filter profile to reject the lower sideband component; (b) Mitigated dispersion penalty in red curve. Courtesy of [143].

Single-sideband (SSB) modulation before time-stretching can also mitigate the effects of dispersion penalty as it eliminates one of the sidebands resulting in [143, 146]. This can be performed by using an optical bandpass filter to suppress one of the optical sidebands as

shown in Figure 2.14(a). In order to demonstrate mitigation of dispersion penalty using SSB modulation conversion, a programmable optical processor, Finisar WaveShaper 100, was used to implement the desired filter profile [143]. As shown in Figure 2.14(b), the RF fading due to dispersion penalty is mitigated (red curve). Also, complete sideband rejection is not necessary as even a partial rejection of one of the sidebands will eliminate the null. The remaining "soft" roll-off in the frequency response can be equalized digitally.

2.7.3 Coherent Detection

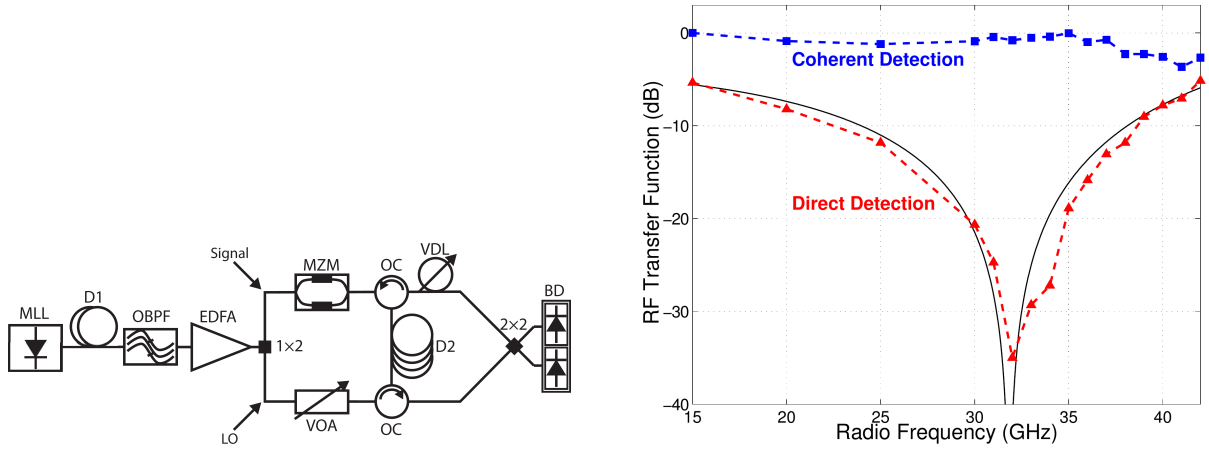

(a) (b)

Figure 2.15: (a) Single sideband modulation implemented using a filter profile to reject the lower sideband component; (b) Mitigated dispersion penalty in red curve. Courtesy [121,147].

In optical communication links, two detection schemes can be employed: direct detection and coherent detection. In direct detection, a photo-detector (PD) captures an optical signal and the power, proportional to the amplitude squared of the electric field, is converted to a current. Direct detection is the most straightforward receiver system and has been exclusively employed in TiSER thus far. Along with simplicity, however, come drawbacks. All phase information of the signal is lost and the output signal lies at baseband where it is susceptible to interference from low frequency noise. In coherent detection receivers, the optical signal is mixed with a reference beam, termed the local oscillator (LO), before detection. The LO is designed to be stable and at a higher power than the signal. Since the PD responds to

the optical electric field squared, a cross term is generated which is linearly proportional to the electric field of the signal and LO. Although more complicated to implement, coherent detection offers many advantages over direct detection. Amplitude and phase information can be extracted, the cross term can be up-shifted away from low frequency noise, and the signal is effectively amplified by the strength of the LO. All of these benefits result in a receiver with up to 20 dB greater sensitivity [121, 147].

2.8 Technologies Enabled by Time-Stretch

Photonic time-stretch was originally developed to overcome the speed and resolution limitations of high-speed ADCs. The time-stretch technology is at the heart of various high-throughput, real-time instruments developed for science, medicine, and engineering applications, as shown in Figure 2.16. Time-stretch has been employed for the characterization of "rare events" such as the discovery of optical rogue waves [148] and soliton explosions [149, 150]. Time-stretch has enabled the study of the buildup of mode-locking in mode-locked laser [151] and internal dynamics of soliton molecules [152] and has transformed the understanding of the mechanisms behind these phenomena. Time-stretch was used to directly observe the electron bunch microstructures with sub-picosecond resolution in a storage ring accelerator [153–155]. It has enabled the record throughput of instruments such as serial time-encoded amplified microscopes (STEAM) [156, 157]. This technology enabled the detection of cancer cells in blood with sensitivity of one cell in a million [157–159]. Record-breaking instruments for vibrometry and velocimetry were implemented using time-stretch [160].

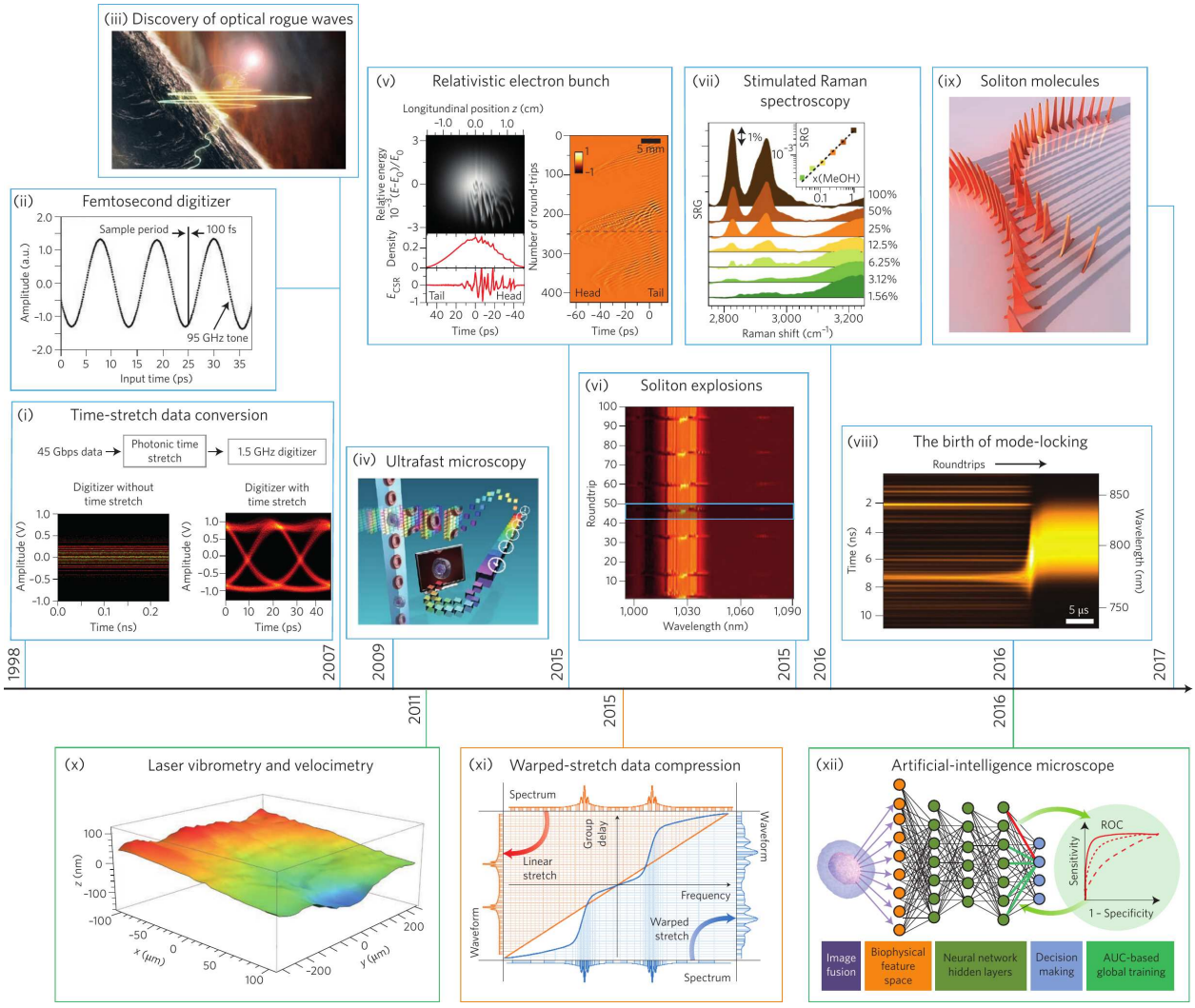

Figure 2.16: A time-line of the various applications enabled by time-stretch. Courtesy of [110].

Various research groups across the world have adopted time-stretch as a technique for characterization of ultra-fast phenomena. "We also stress the simplicity of the dispersive time-stretch technique and the straightforward way in which the statistical and correlation metrics can be extracted from experimental data. We suggest that this technique of real-time spectral noise characterisation should now become the standard approach to analysing noise effects in nonlinear fibre propagation as it provides a powerful means of allowing rapid experimental optimization, and generating large data sets from experiment in this way is orders of magnitude more efficient than stochastic simulations. Indeed, we anticipate wide

application of this technique for detailed studies of noise in broadband pulse propagation, the characterization of quantum-optical intensity-correlations in soliton dynamics, and in the study of spectral instabilities in ultrafast nonlinear optics in general" [161].

A time-stretch accelerated processor (TiSAP) was implemented for BER based optical performance monitoring to implement agile optical networks. This system relays the BER information of the signals in the network as a feedback to the software-defined networking controller to perform rapid corrective actions for network disasters. This technology was also used to perform real-time, in-service signal integrity analysis of 10 Gbit/s streaming video packets for the first time on a commercial optical networking platform [56]. Time-stretch technology was also used to implement an extremely fast, ultra wide-band instantaneous frequency measurement instrument [76]. A single-shot network analyzer for ultra-fast characterization of the frequency response of high-bandwidth electronic, electro-optic and opto-electronic devices/modules/systems was developed using time-stretch [86]. These technologies will be discussed in detail in the subsequent chapters.

We have developed an intuitive web based calculator tool for quickly designing time-stretch systems by characterizing dispersion penalty, the time-bandwidth product, spectral resolution, and time-wavelength mapping for a set of system parameters [162, 163]. The website based tools were released publicly and can be used anyone online.

CHAPTER 3

Time-Stretch Accelerated Processor (TiSAP)

TiSER can capture high-speed data with high-throughput and apply digital signal processing to recover the original signal. All the previous TiSER demonstrations have performed this DSP in software on a PC after manually transferring the digitized data from a real-time oscilloscope. In this chapter, I introduce the development of time-stretch accelerated processor for in-service signal analysis which uses a custom developed digitizer board with a powerful field programmable gate array capable of real-time processing of time-stretched digitized data streams from the ADC. We report an in-service, digital signal analysis of up to 40 Gigabit/s data using an up to 2 Terabit/s (equivalent) burst-mode processor for enabling agile optical networks. The processor comprises a time-stretch front-end and a custom data acquisition and real-time signal processing back-end. Experimental demonstration of real-time, in-service, signal integrity analysis of streaming video packets at 10 and 12.5 Gbit/s is also presented. The measurement of parameters such as jitter, rise and fall times, based on the eye diagrams reported by the time-stretch systems is compared with equivalent-time sampling and real-time oscilloscopes.

3.1 Introduction

The rapidly increasing demand for higher data rates in Internet data communication demands better network performance. This in turn requires the implementation of faster ways to monitor degradation/faults in the system and to perform efficient, automated corrective actions to the affected unit in the optical fiber communication network [47,164]. Burst-mode real-time, in-service, signal analysis for degradation/fault detection can meet these challenge

and help improve quality of transmission of the optical network. It also can benefit radio frequency communication technology by enabling adaptive modulation schemes based on the ultra-fast estimated in-service bit-error rate [165]. Real-time, in-service, eye diagram generation and BER estimation has always been a challenging problem. Prior art utilizing a front-end analog-to-digital converter [166] to digitize the data signal in real-time and then perform BER estimation on in-service data has considerable limitations. Performing real-time signal analysis on high-speed data (> 5 Gbit/s) requires very high bandwidth digitizers with very high resolution, which is difficult to achieve [90] and also a real-time processing platform that could handle the huge amount of data that is being generated by sampling at a rate much higher than the bandwidth of the signal. High performance ADCs that support very high analog bandwidths are also very power hungry and require expensive process technologies [90, 91, 94, 95].

Bit error rate testers have been a popular instrument for BER measurements of devices, channels, and systems. Although BERTs can take very high accurate measurements, it can only be used for out-of-service measurements and cannot test the performance of a device while in service. A sampling oscilloscope performs signal integrity measurements by relying on the repetitive or clock synchronous nature of the input signal for digital reconstruction. An equivalent-time oscilloscope samples signals at megahertz frequencies (up to 10 MHz) and then reconstructs the signals digitally, which requires a long time for accurate measurements. Real-time oscilloscopes and digitizer are gaining popularity for use in signal integrity measurements due to the availability of ADCs with high analog bandwidth and high sampling rates. However, these oscilloscopes are very expensive, suffer from high power consumption and have very limited resolution at high signal bandwidths.

As opposed to traditional approaches, the time-stretched enhanced recording (TiSER) digitizer [95, 110–115, 119–121, 147] enables ultra-high throughput and precision capture of wide-band analog signals by slowing them down so they can be digitized in real-time with a slower, higher-resolution, more energy efficient analog-to-digital converter. By contrast, a sampling or equivalent-time oscilloscope performs signal integrity measurements by relying on the repetitive or clock synchronous nature of the input signal for digital reconstruction.

An equivalent-time oscilloscope samples signals at megahertz frequencies (up to 10 MHz) and then reconstructs the signals digitally, which requires a long time for accurate measurements. Even though it can achieve equivalent-time bandwidths of up to 110 GHz, it cannot capture single, rare and non-repetitive signal events. The TiSER oscilloscope, on the other hand, features an extremely fast acquisition time and employs real-time burst sampling modality to achieve much higher sampling throughput compared to conventional communication signal analyzers. It can also record ultra-fast, non-repetitive dynamics that occur within the burst period, which is impossible to achieve in a conventional sampling oscilloscope [119].

We report a 2 Terabit/s burst-mode time-stretch accelerated processor (TiSAP) for optical performance monitoring and RF signal integrity analysis for enabling the development of next-generation software-defined networks for optical and RF communication. The TiSAP combines the time-stretch pre-processing, analog-to-digital conversion, clock recovery from the data and digital processing on a single physical platform [56]. The system eliminates read/write transfer bottlenecks and software processing latencies, using parallel digital signal processing. The in-service, captured time-stretched data is digitally processed in real-time, using a field programmable gate array (FPGA) with a large local random access memory (RAM) bank. It can also be streamed to a host PC or to a remote computer via network for post-processing and additional analysis.

We demonstrate real-time digitization and processing of 10 Gigabit/s and 40 Gigabit/s RF signals generated by a pseudo-random bit sequence (PRBS) generator to generate real-time eye diagrams. The recovered data, along with synchronization information, is streamed to a computer, where eye diagrams are analyzed in software to estimate the BER.

3.2 TiSAP System Design

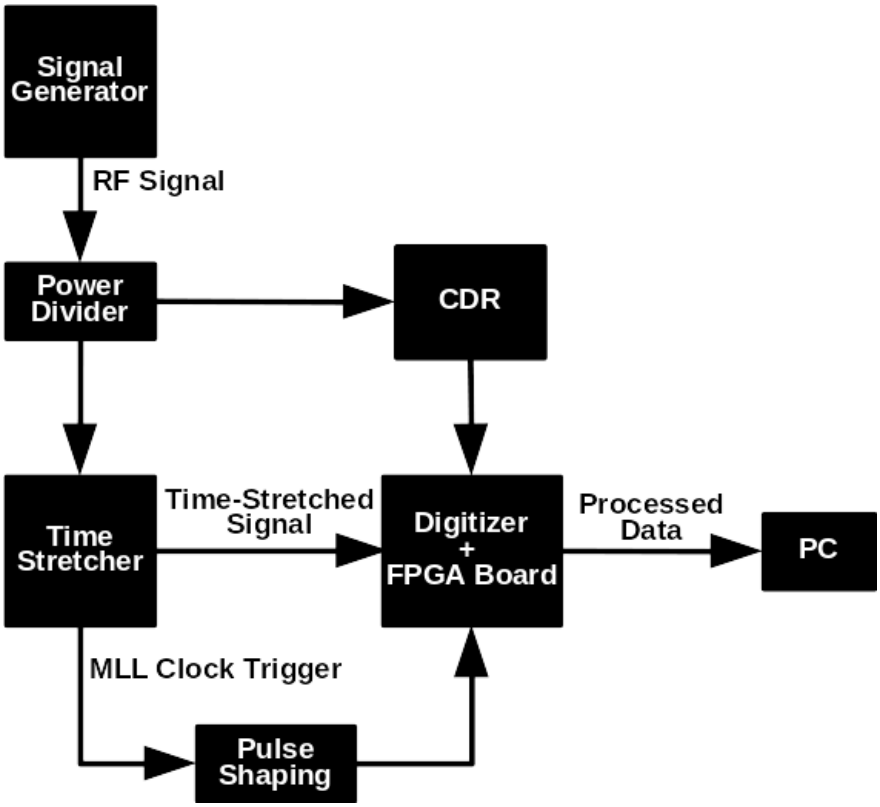

Figure 3.1: Block diagram of the time-stretch accelerated processor (TiSAP) for high-speed signal analysis. [56]

The TiSAP prototype system developed includes a photonic time-stretch front-end and a custom designed high-speed electronic back-end with an on-board 3 Giga-samples/s ADC, a clock and data recovery (CDR) module for in-service mode of operation, an FPGA (Xilinx Virtex 6, XC6VLX240T), a high-speed RAM bank, and high-speed PC interfaces as shown in Figure 3.1 [56].

3.2.1 Time-Stretch Front-end System

The photonic time-stretch front-end, as shown in Figure 3.2, consists of a femto-second mode locked laser (MLL) operating at ~36.7 MHz with 30 mW output power, and < 1 ps pulse width. A linearly chirped optical signal, obtained by dispersing the pulses in a dispersion

compensating fiber (DCF), D1, is modulated by the incoming electrical data, using a Mach-Zehnder modulator, EOM, which supports up to 40 Gbit/s. As a second step, the data signal is stretched in time by the propagation through a second dispersive fiber (D2), which reduces its analog bandwidth to fit within that of the 2.5 Giga-samples/s digitizer. The stretch factor, M, is given by equation 2.4.

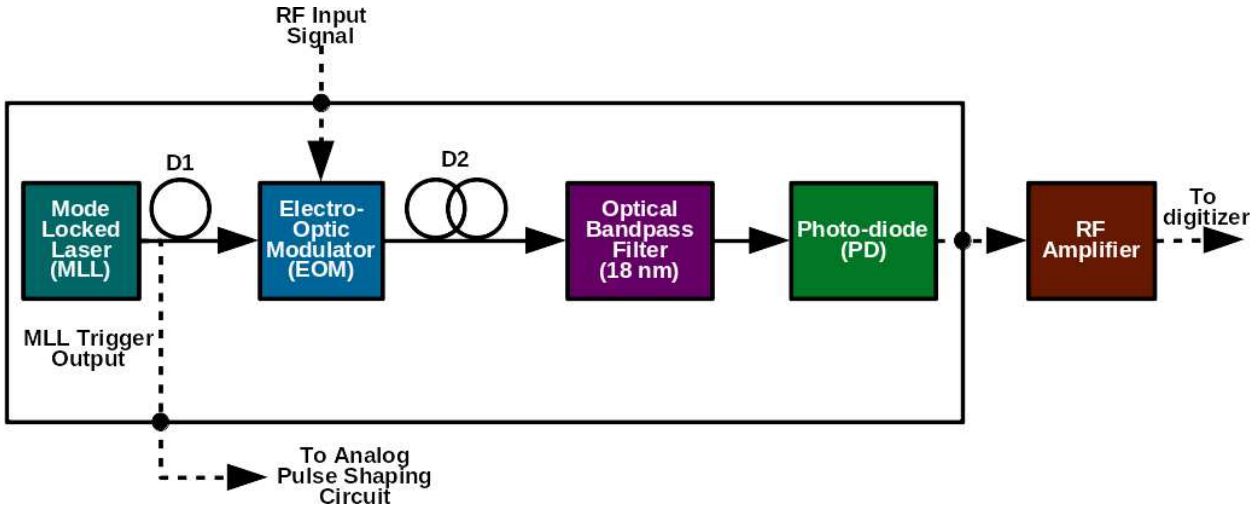

Figure 3.2: A detailed block diagram of the time-stretch front-end referred to as Time-Stretcher in Figure 3.1. Courtesy of [121].

With this approach, fast data can be captured in real-time by using a slow, high-resolution ADC. The effective temporal resolution of real-time TiSER after time-stretch, however, scales with the stretch factor, which results in an effective sampling rate of stretch factor times the sampling rate of the back-end digitizer. The dispersion for D1 and D2 was chosen to have a stretch factor of 100 for testing 40 Gigabit/s data and the sampling rate of the digitizer was selected to be 2.5 Giga-samples/s, therefore the effective sampling rate of the system is 250 Giga-samples/s (100*2.5 Giga-samples/s).

The time-stretched signal after propagation through D2, is sliced by an optical bandpass filter with 18 nm to center the optical spectrum at 1571 nm. The optical signal from the bandpass filter is converted to an electrical signal by a photo-diode (PD) with 0.85 A/W responsivity and transimpedance gain of 500Ω. The output of the photo-diode is amplified, DC shifted and fed as an analog input to the electronic back-end board shown in Figure 3.4.

3.2.2 Electronic Back-end System

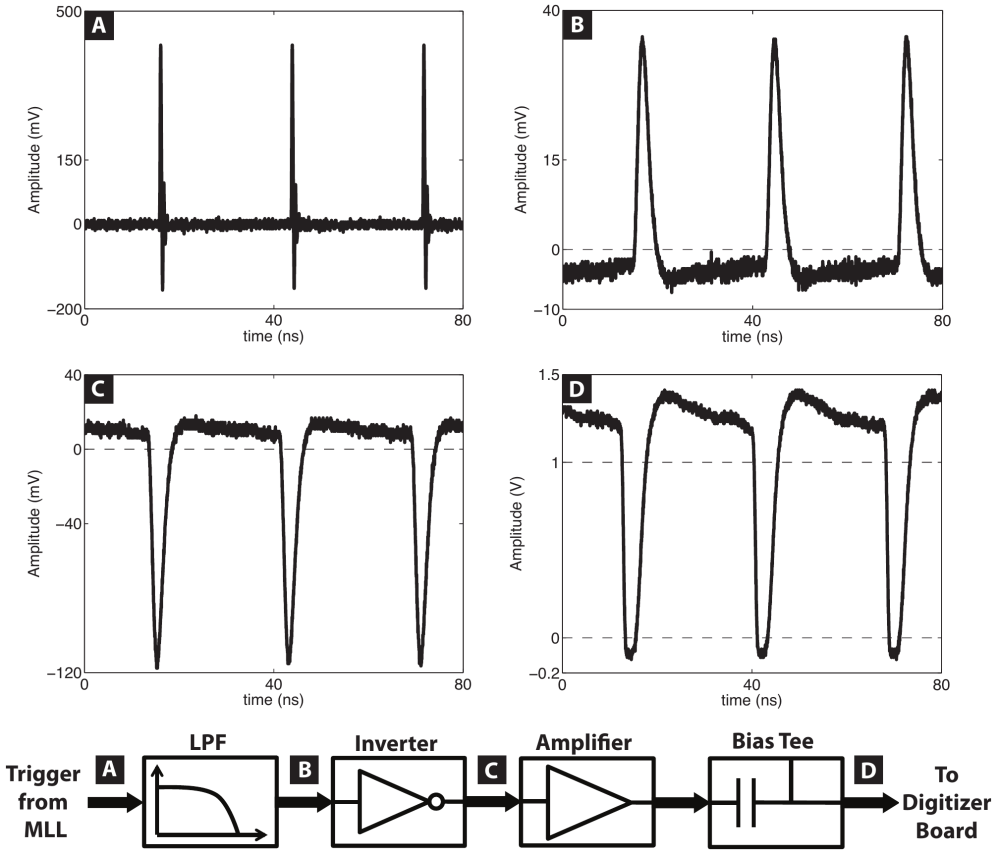

Figure 3.3: The pulse shaping circuit for processing the trigger signal (SYNC) from the mode-locked laser. Courtesy of [121].

A small fraction of the laser signal from the MLL is sent to a separate photo-detector (not shown in Figure 3.2) and it's impulse response is used to generate a synchronization (SYNC) pulse train that is inputted to the general-purpose I/O terminals of the FPGA as the trigger input to the system. Analog pulse conditioning as shown in Figure 3.3 is necessary in order to appropriately trigger the FPGA, i.e., to comply with the FPGA input terminal logic levels and the minimum pulse widths. To this end, the impulse response of the photo-detector with a pulse width < 1 ns is broadened in time by using a 117 MHz analog low pass filter which significantly attenuates the signal. The broadened pulse is inverted by using an inverting amplifier to create a high duty cycle signal. The inverted signal is amplified using a 500 MHz low noise amplifier (LNA) with 25 dB gain and DC shifted using a bias tee to raise the

logic HIGH signal level to appropriate voltage.

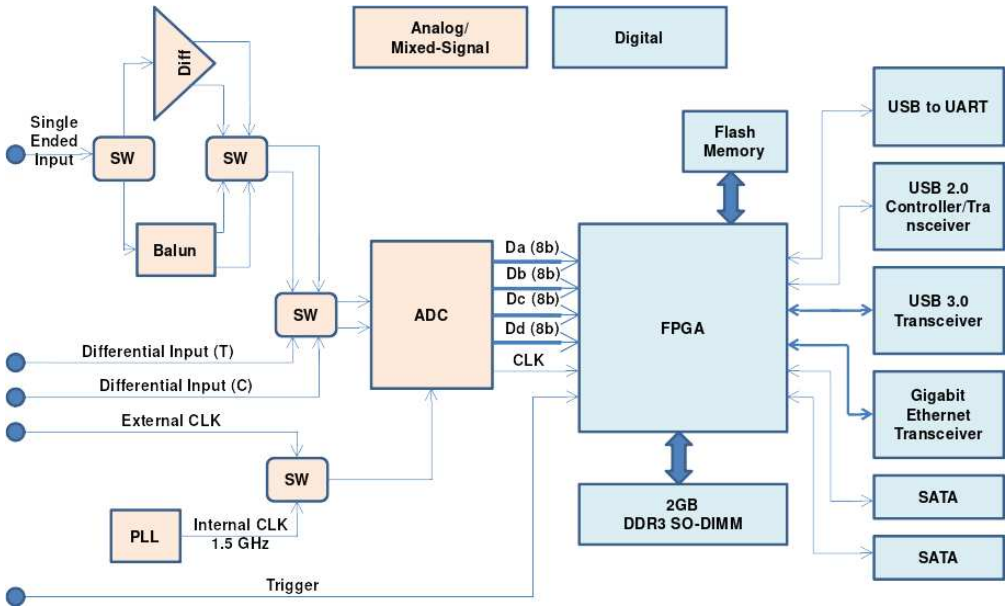

Figure 3.4: A block diagram of the custom designed 3 Giga-samples/s digitizer-FPGA board. [56]

The custom digitizer-FPGA board shown in Figure 3.4 uses an 8-bit ADC (National Semiconductors ADC083000), which supports a maximum sampling rate of 3 Giga-samples/s. The digitizer is operated in a mode that utilizes both the rising and falling edge of the input clock, resulting in the overall sample rate being twice the input clock frequency [167]. The external clock frequency used is 1.25 GHz which results in a sampling rate of 2.5 Giga-samples/s. The external clock is obtained by dividing the clock signal generated by either a PRBS generator or a clock and data recovery module. The digitized outputs in the ADC are demultiplexed to four 8-bit ports, each of which outputs four bytes of digitized sample points at double the data rate (DDR) of the 312.5 MHz differential output clock. This differential output clock is divided by two inside the FPGA, which consequently comprises the main computation clock of 156.25 MHz. The total number of 8-bit digitized sample points captured by FPGA in a computation clock cycle therefore is 16. The FPGA device on the board is a Xilinx Virtex 6 XC6VLX240T device which has more than 240,000 logic blocks with 768 DSP48E1 slices and over 14 Mb of integrated block RAM [168].

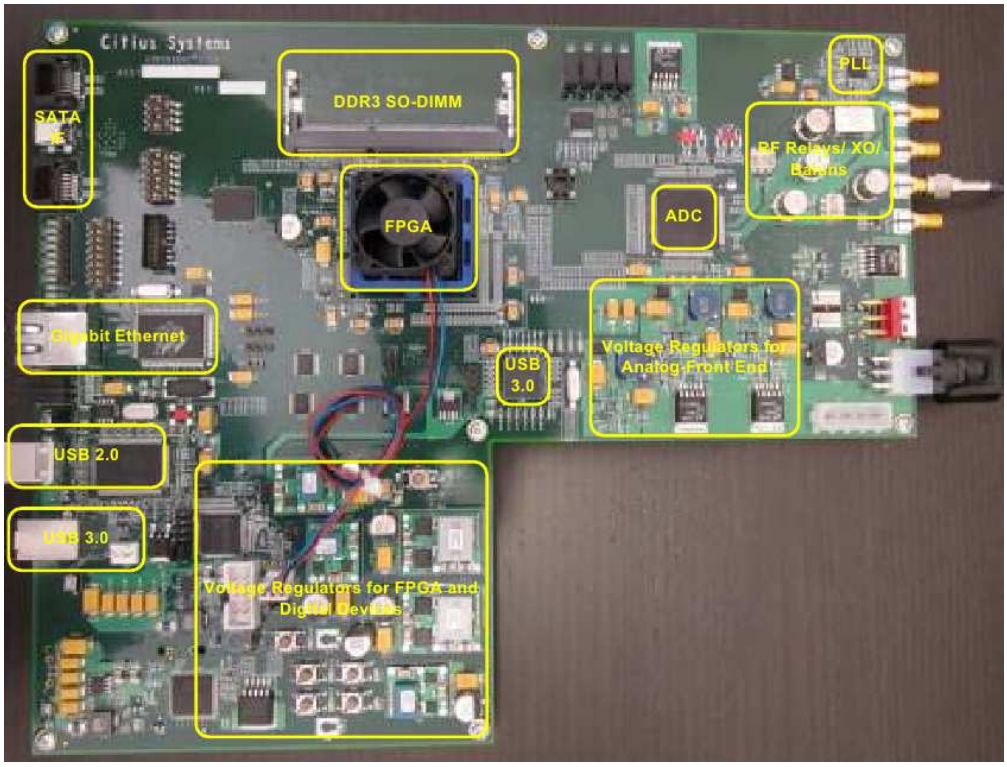

Figure 3.5: A photograph of the custom designed 3 Giga-samples/s digitizer-FPGA board with 2 GB of DDR-III SO-DIMM RAM module, support for USB 2.0, USB 3.0, SATA, and Gigabit Ethernet interfaces to computer or network. Courtesy of [121].

The ADC and FPGA system are synchronized to the same clock signal. The digitizer board has an on-board clock generator and an internal PLL to generate a 1.5 GHz clock signal that can be used to operate the ADC at its maximum sampling rate of 3 Giga-samples/s. However for the system described here, the digitizer-FPGA board was externally clocked. An an appropriate clock divider circuit is used to generate a 1.25 GHz clock signal from either the clock output of a PRBS generator or from a clock and data recovery module for in-service operation of the system. When the system is used in in-service mode, i.e. to analyze the signal integrity of a functioning network or a communication channel, a CDR module is used to recover clock from the incoming data signal. When using the system in out-of-service mode with a pseudo-random bit sequence generator, the clock output of the generator can be used directly instead of employing the CDR module to recover clock from data input.

A photograph of the custom digitizer-FPGA board is shown in Figure 3.5. The FPGA can be interfaced to a computer using any of the multiple types of interfaces available including USB 2.0, USB 3.0, SATA, or Gigabit Ethernet. The Gigabit Ethernet interface to the FPGA device enables transmission of collected digitized samples or processed data to a remote computer or to the cloud network for additional analysis and archival. The digitizer-FPGA board also has an interface to a 2 GB Micron DDR-III small outline dual in-line memory module (SO-DIMM) RAM compatible with the FPGA device. A DDR controller intellectual property (IP) core can be instantiated into the FPGA design for enabling buffering up to 2 GB of 3 Giga-samples/s sampled or digitally processed data.

3.3 FPGA Logic Implementation

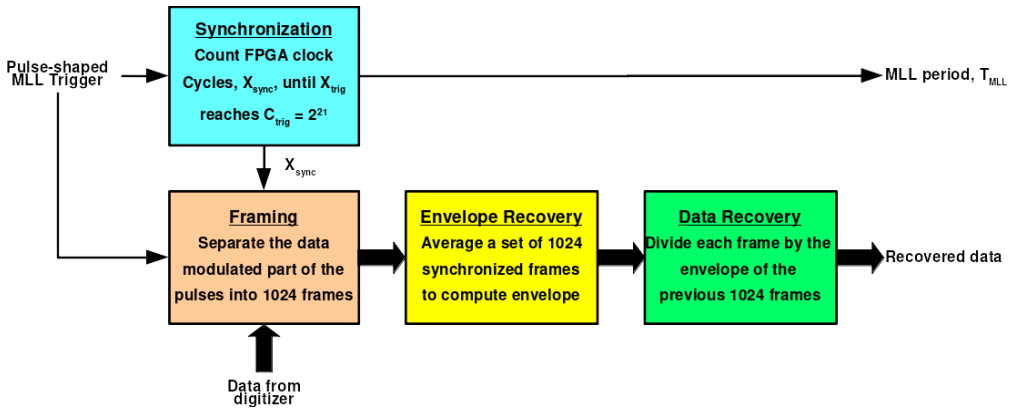

Figure 3.6: A block diagram of the pipelined logic modules implemented on FPGA.

Digitally recovering the time-stretched data poses significant challenges, including dynamically synchronizing the FPGA to the MLL pulse, determining the envelope of the time-stretch carrier pulse, and removing the envelope from each captured modulated pulse. The custom logic implemented on the FPGA consists of four modules which run concurrently and in a pipeline and can be in seen in Figure 3.6. A pictorial representation of the data flow between the pipelined modules can be found in Figure 3.7. The synchronization module counts the laser pulses to precisely determine the laser repetition rate for synchronizing the FPGA to the time-stretched pulses. The framing module uses the precisely computed laser repetition

rate to synchronize the frames of time-stretch pulse data by performing a modulo operation in the time-domain. This module also consists of a part of the FPGA logic, running at a much higher clock rate compared to the rest of the logic in order to sample the incoming trigger signal from the MLL and estimate the starting point of the frame data.

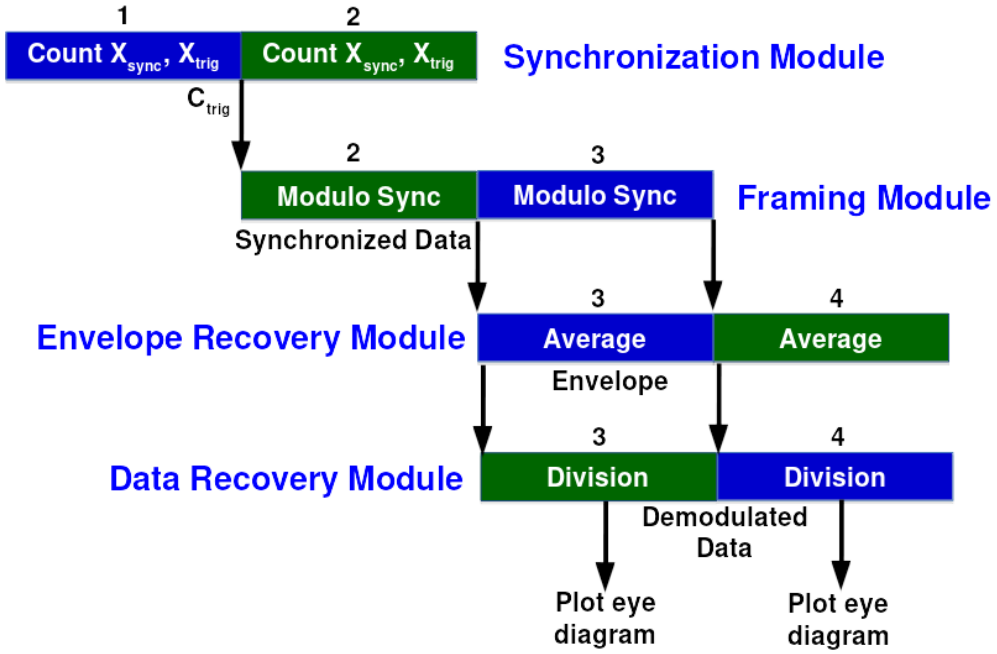

Figure 3.7: A pictorial representation of the pipelined logic implemented on FPGA. Each block represents 1024 laser pulses ∼4403.2 clock cycles ≈ 28.18 µs.

The envelope recovery module performs averaging of every 1024 synchronized frames of the data modulated, time-stretched pulses to estimate the envelope of the time-stretched signal. The data recovery module divides the next incoming synchronized frames by the previously computed envelope to recover the high-speed data signal to be analyzed. This section is adapted from [56,121], for which I jointly developed the logic design described here with Brandon Buckley.

Table 3.1: A glossary of the variables used in the design description

Variable	Description
C_{trig}	The fixed number of mode-locked laser trigger pulses to be counted in the synchronization module to start synchronization.
X_{trig}	Trigger Counter: Counts the number of mode-locked laser trigger pulses.
X_{sync}	Synchronization Counter: Counts the number of FPGA clock cycles at 156.25 MHz corresponding to the fixed C_{trig} MLL trigger pulse count. When X_{trig} reaches the fixed C_{trig} count, the synchronization module stores the corresponding X_{sync} value and resets the count.
N_{sample}	Keeps a count of the number of digitized sample points from the ADC since the first trigger pulse in the framing module and resets once 1024 frames have been reached.
T_{MLL}	The number of sample points representing the mode-locked laser period.
N_{clk}	Counts the number of FPGA clock cycles at 156.25 MHz within the framing module to obtain the number of sample points given by, $N_{sample} = 16 \times N_{clk}$.
N_{frame}	Frame counter: Incremented every time a synchronized frame has been formed.
R_{trig}	Trigger Register Value

A glossary of the various variables used in the FPGA logic design element description can be found in Table 3.1.

3.3.1 Synchronization Module

The purpose of synchronization module is to synchronize the digitized time-stretched data modulated MLL pulse with the digital data, FPGA, and ADC clock domains. If we recall Section 3.2.2, the FPGA and ADC are synchronized by the same clock derived from the data signal. The synchronization module accomplishes this by computing the period of the asynchronous MLL pulse very accurately in terms of the number of the digitized sample

points, which are synchronized to the FPGA clock. The period of the MLL pulse can be computed with respect to FPGA clock by counting a large number of input MLL trigger pulses, C_{trig}, and dividing it from the corresponding number of FPGA clock cycles, X_{sync}. For any specified trigger count, the corresponding synchronization count specifies the average MLL pulse period. If we can estimate this pulse period very accurately we can synchronize the operations on the digitized laser pulses and the modulated data in all the subsequent modules in the pipeline.

The synchronization module is implemented by concurrently operating two counters, one counting the laser pulses via trigger signal, X_{trig}, and the other counting the number of the FPGA clock pulses, X_{sync}. Once the trigger counter reaches a fixed number, C_{trig} (typically $= 2^{21}$), the corresponding FPGA clock count is stored into a register, both counters are reset, and it starts counting again. The mode-locked laser pulse period can therefore be given by,

$$T_{MLL}(clock\ cycles) = \frac{X_{sync}}{C_{trig}} \tag{3.1}$$

$$T_{MLL}(sample\ points) = \frac{X_{sync}}{C_{trig}} \times 16 \tag{3.2}$$

A simple state diagram representation of the state machine is shown in Figure 3.8. Since the MLL repetition rate is ∼36.7 MHz and the FPGA clock frequency is 156.25 MHz, the MLL pulse period can be given by $\frac{X_{sync}}{C_{trig}} \approx 4.25$ clock cycles. To obviate the need for a decimal divider implementation, C_{trig} was chosen to be a power of two, which would enable division by shifting the decimal point.

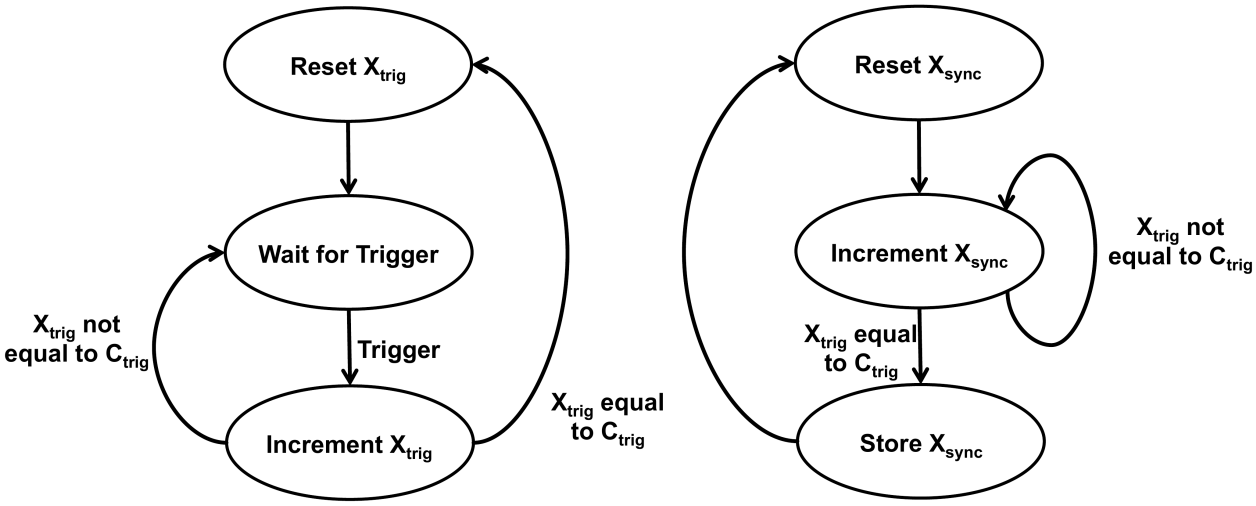

Figure 3.8: State machine diagram for the synchronization module. Courtesy of [121].

Intuitively, using a larger trigger count would result in a more accurate determination of the MLL pulse period. Quantitatively, the main cause for the inaccuracy in synchronization can be attributed to the integer granularity of the synchronization counter, X_{sync}. Since 16 digitized sample points are received from the ADC at every FPGA clock cycle, the MLL pulse period can also be given by $T_{MLL} = (X_{sync} / C_{trig}) \times 16 \approx 69$ sample points. For a maximum error in X_{sync} of one clock cycle, the uncertainty in T_{MLL} is given by $16/C_{trig}$. The accuracy can be improved by using a larger trigger to obtain, X_{sync}, with slower synchronization response time, which is given by C_{trig} /36.7 MHz = C_{trig} × 27 ns. But the MLL pulse repetition rate slowly drifts over time. Therefore, to account for temperature fluctuations, we selected a response time faster than 100 ms, which gives us $C_{trig} = 2^{21}$ (as $\log_2 C_{trig} < 22$).

3.3.2 Framing Module

The framing module receives the digitized data from the ADC and creates frames containing 48 sample points each of the time-stretched pulses. It was found that for the dispersive fiber and optical bandwidth configuration used in the system, 48 samples from the ADC corresponding to 3 FPGA clock cycles, is sufficient to collect the usable portion of the time-stretched pulse.

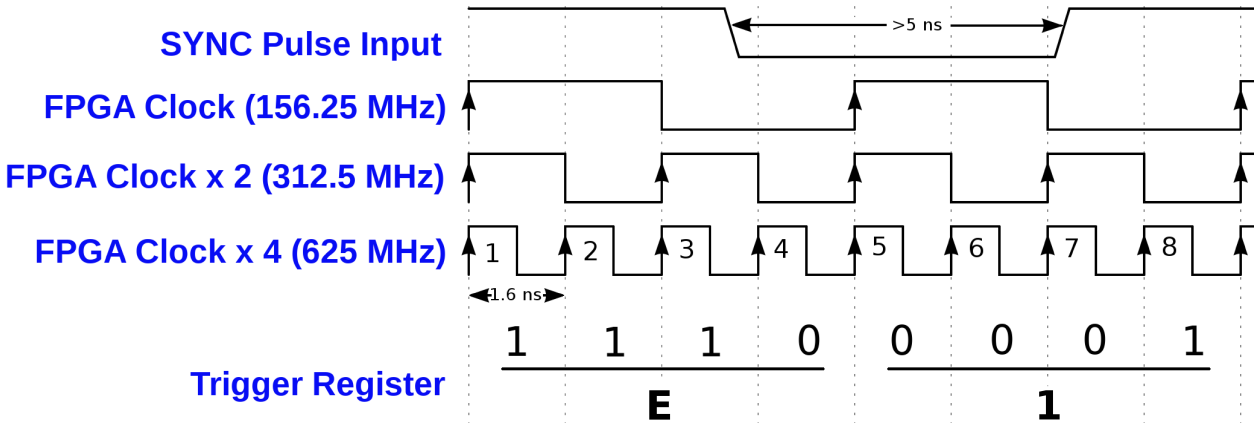

Figure 3.9: An example timing diagram for the 1-bit quantizer operating at 625 Mega-sample/s enabled by the flip-flop synchronizer circuit running at four times the FPGA clock frequency.

The framing module also has a special trigger pulse sampling logic implemented inside the FPGA that runs at 625 MHz which is four times the FPGA clock frequency to accurately determine an approximate start point of the trigger pulse. The I/O terminal of the FPGA receiving the analog pulse shaped trigger (see Section 3.2.2) signal is synchronized by using cascaded flip-flops running at 625 MHz. To this end we used the Xilinx Mixed-Mode Clock Manager, employing integrated phase locked loops (PLL) [169], to generate a clock frequency that is four times that the main FPGA clock frequency. The flip-flop based synchronizer logic effectively function as 1-bit quantizer running at 625 Mega-sample/s producing four sequentially sampled bits of the trigger pulse at the main FPGA clock frequency of $625/4 = 156.25$ MHz. We combine two such nibbles (4- bits) from two consecutive FPGA clock cycles in time to create a byte of trigger pulse sample bits which is stored to a trigger register, R_{trig}, as shown in an example timing diagram on Figure 3.9. Based on this sampling rate and the duty cycle of the analog pulse shaped trigger shown in Figure 3.3 and the example timing diagram shown in Figure 3.9, we can observe that there are only eight possible trigger register values which can be seen in Table 3.2. Please note that only the flip-flop based synchronizer logic for sampling the trigger pulse operates at 625 MHz clock, whereas all the other computational logic operates at the main FPGA clock frequency of 156.25 MHz.

Table 3.2: The only eight potential values of the trigger register, R_{trig}, in binary and hexadecimal representation

Trigger Register Values (Binary)	**Trigger Register Values (Hexadecimal)**
0000 1111	0F
1000 1111	8F
1000 0111	87
1100 0111	C7
1100 0011	C3
1110 0011	E3
1110 0001	E1
1111 0000	F0

Each of the eight trigger register values has a corresponding sample point position closer to the starting of the rising edge of the time-stretched pulse. The offset for the starting sample point of the pulse for these eight possible trigger register values depends on the delays of the RF cables used in the setup. Once the sample point offset is estimated for these eight possible positions for a fixed experimental setup, the framing logic can use the trigger register value to determine the approximate starting sampling point in time to begin storing the data frames. But the analog pulse-shaped MLL trigger is only sampled at 1/4th of the ADC sampling rate which would lead to an unacceptable jitter of 4 sample points. Therefore we cannot use this approach alone for creating the data frames at the occurrence of every trigger.

Instead of only using the trigger register value for every frame, we only use it for starting the sample point of the first frame at the beginning of 1024 frame sequences. For the subsequent starting sample points within the next 1023 frames, we make use of the FPGA clock count stored previously by the synchronization module, X_{sync}. By performing a modulo operation on the digitized samples count since the first MLL trigger, N_{sample}, with the MLL

period in sample points, T_{MLL}, the time to begin the next data frame is precisely estimated with one sample point resolution. Modulo operation can be a very logic resource consuming operation. We designed an optimized implementation of modulo computation logic with significantly lesser resources than conventional approaches. The modulo operation to be performed is given as,

$$N_{sample} \pmod{T_{MLL}} = N_{sample} - T_{MLL} \times floor\left(\frac{N_{sample}}{T_{MLL}}\right) \tag{3.3}$$

We obviate the need for the divider in equation 3.3 by using a frame counter N_{frame} which gets incremented every time a frame is formed, which is equivalent to the operation of floor$\left(\frac{N_{sample}}{T_{MLL}}\right)$. A second counter, N_{clk}, counts the number of the sample points and gets incremented every clock cycle such that $N_{sample} = 16 \times N_{clk}$. Therefore using equation 3.2, 3.3 can be written as [121],

$$\begin{aligned} N_{sample} \pmod{T_{MLL}} &= N_{sample} - T_{MLL} \times floor\left(\frac{N_{sample}}{T_{MLL}}\right) \\ &= 16 \times N_{clk} - \left(\frac{X_{sync}}{C_{trig}}\right) \times 16 \times N_{frame} \\ &= 2^4 \times N_{clk} - \left(\frac{X_{sync}}{2^{log_2 C_{trig} - 4}}\right) \times N_{frame} \\ &= \left(\frac{2^{log_2 C_{trig}} \times N_{clk} - X_{sync} \times N_{frame}}{2^{log_2 C_{trig} - 4}}\right) \end{aligned} \tag{3.4}$$

As seen in the final form of equation 3.4, the operation only a multiplication, subtraction, and a division. The multiplication operation of $X_{sync} \times N_{frame}$ is implemented by incrementing another counter by the X_{sync} count for every frame. The division in the equation is by a number that is a power of two which is accomplished by right shifting and decimal point truncation. Whenever the modulo operation for equation 3.4 yields a value less than 16, the framing module starts creating a new frame. The corresponding modulo value points to starting sample point out of the 16 sample points in the current FPGA clock cycle. A state diagram of the state machine implemented for this logic is shown in Figure 3.10.

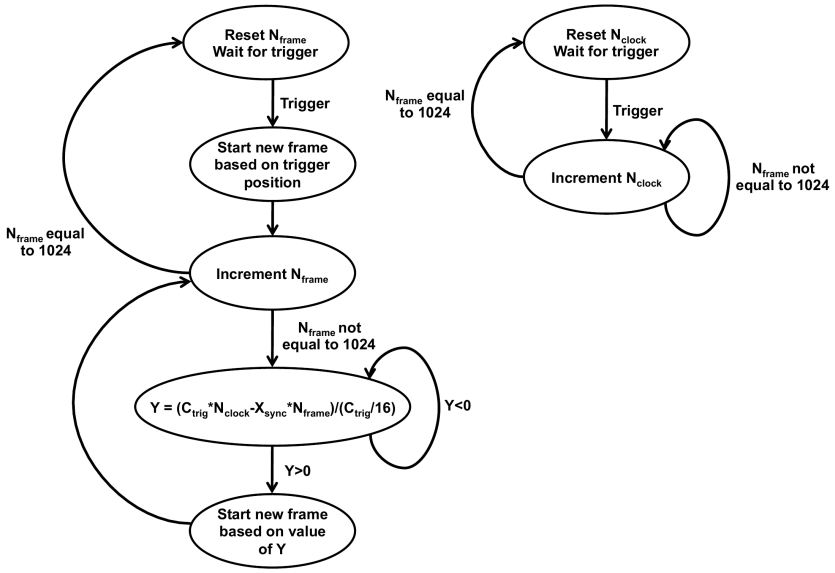

Figure 3.10: State machine implemented for the framing module. Courtesy of [121].

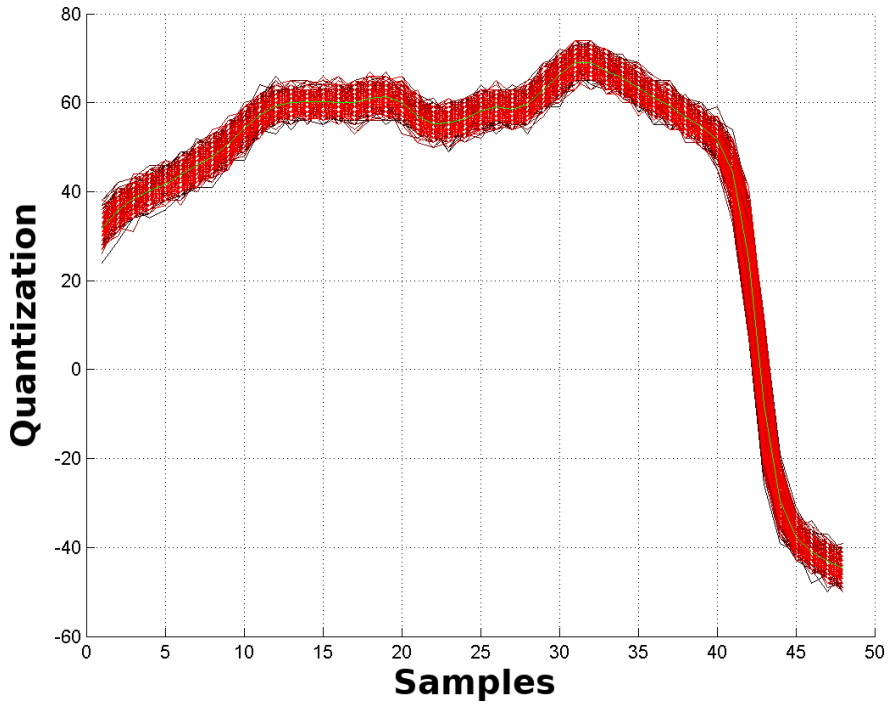

Figure 3.11: The successful synchronization of 330 overlayed frames of unmodulated time-stretched pulses with one sample point jitter.

The accuracy in the synchronization of the frames corresponding to the unmodulated time-stretched mode-locked laser pulses can be visualized by overlaying synchronized con-

secutive frames as shown in Figure 3.11. A source of jitter in the synchronized frames is the error in the computation of N_{clk}. As the frames are being formed for 1024 pulses, the deviation from the true starting point can accumulate and cause a walk-off of the frame starting. Since we reset and find the new trigger position based on the trigger register every 1024 frames, we do reduce the walk-off jitter periodically. The average walk-off jitter is given by $2^{-\left(log_2 C_{trig}-14\right)}$, which for $C_{trig} = 2^{21}$ to have sub-100 ms response time, is ~0.008 sample points, which is negligible. The truncation operation during division in the implemented modulo logic, results in a minimum of one-sample point jitter as can be seen in Figure 3.11. This limits the resolution with which the time-stretched pulse can be synchronized.

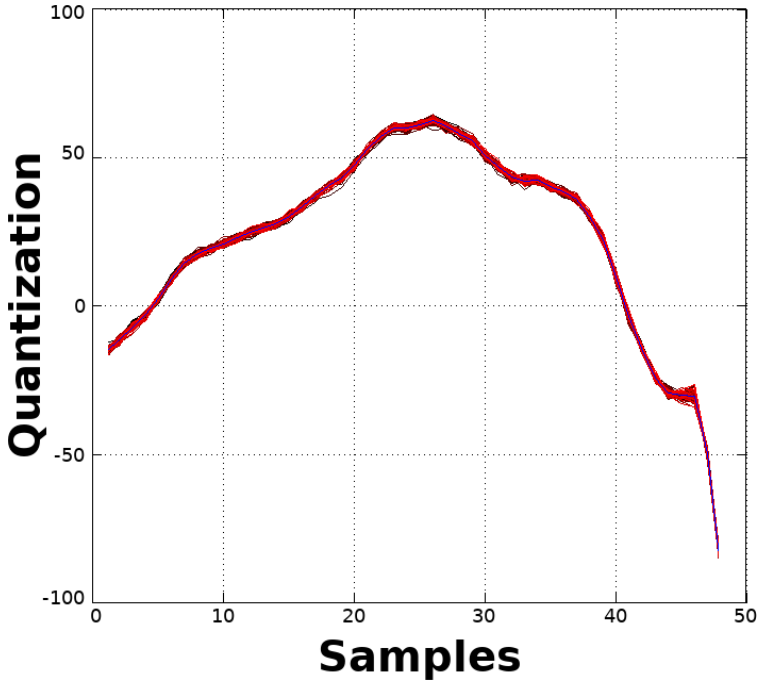

Figure 3.12: The successful synchronization of numerous overlayed frames of unmodulated time-stretched pulses after interpolation resulting in extremely low jitter.

The resolution of synchronization of the time-stretched pulses can be significantly improved by applying linear interpolation on the digitized samples. After performing linear interpolation, we find that the jitter due to truncation of modulo is extremely low as can be seen in Figure 3.12. Although the interpolation of synchronized frames was implemented on the FPGA to prove that it can reduce the jitter due truncation, it was not implemented in

the complete system design for generating eye diagrams and this work is to be done in the future.

3.3.3 Envelope Recovery Module

The envelope recovery module averages each set of synchronized frames of time-stretched pulses carrying the digital data to be analyzed to compute an envelope. The envelope of the time-stretched pulse is used for recovering the modulated digital data by dividing the synchronized modulated pulses with it. Each modulated laser pulse after time-stretching can be represented by the following equation:

$$Pulse(t) = Env(t)[1 + Sig(t)] \tag{3.5}$$

$$\Rightarrow Sig(t) = \frac{Pulse(t)}{Env(t)} - 1 \tag{3.6}$$

where $Env(t)$ is the spectral envelope of the MLL pulse after dispersion and $Sig(t)$ is the time-stretched signal of interest [121].

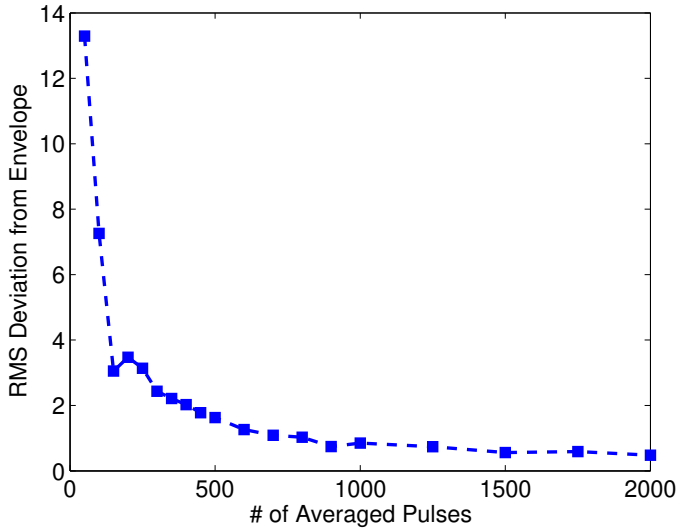

Figure 3.13: The RMS deviation of the envelope calculated after averaging a varying number of synchronized pulses. The RMS deviation flattens out after increasing the number of frames beyond 1000. Courtesy of [121].

To ensure an accurate envelope calculation, a sufficient number of pulses have to be

averaged. To determine an appropriate number of frames averaged, we calculated the root mean square (RMS) deviation from the reference envelope (generated by averaging > 3000 frames) for varying numbers of frames averaged. This analysis demonstrated that the RMS deviation flattens out beyond 1000 Frames as seen in Figure 3.13. We consequently chose an averaging over 1024 pulses to compute the envelope obviating the division operation which reduces FPGA resource consumption.

3.3.4 Data Recovery Module

The data recovery from the time-stretched pulses is performed by dividing the synchronized frames by the computed envelope using a single precision floating-point (SPFP) divider logic. The fixed point data received from the ADC in bipolar offset binary (BOB) format is first converted to signed twos-complement format. The two-complement format data is then converted to IEEE 754 format for single-precision floating point representation in 32 bits, consisting of a 24-bit mantissa and an 8-bit exponent [170]. We used the Xilinx floating point IP core to divide each frame with the envelope computed from the previously synchronized 1024 pulses. The latency of the SPFP divider IP core was 28 clock cycles (mantissa bit width, $24 + 4$ clock cycles). The prototype logic with the divider core dropped three out of every four pulses resulting in a throughput reduction by a factor of four. A carefully selected and designed fixed point divider can be used in the future to reduce the logic resource consumption as well the drop in throughput.

3.3.5 FPGA Logic Resource Utilization

Table 3.3: FPGA Device Utilization Summary

Slice Logic Utilization	Used	Available	Utilization
Number of slice registers	20,762	301,440	6%
Number of slice look-up tables (LUT)	25,445	150,720	16%
Number of occupied slices	8,975	37,680	23%
Number of RAMB18E1/FIFO18E1s	8	832	1%
Number of ILOGICE1/ISERDES1s	38	720	5%
Number of OLOGICE1/OSERDES1s	18	720	2%

The FPGA logic resource utilization summary can be found on Table 3.3. The implemented FPGA logic utilized only 6% of the slice register and 16% of the slice look-up tables. The FPGA outputs the mode-locked laser pulse period, T_{MLL}, in term of sample points and each of the 48 sample point frame of the recovered data using eight 18 bit wide first-in, first-out (FIFO) buffers, outputting 2 bytes worth of data each. The logic resource utilization could be further optimized by custom designing the right fixed point divider instead of using the available Xilinx single-precision floating point divider IP core.

3.4 Testing of PRBS Data

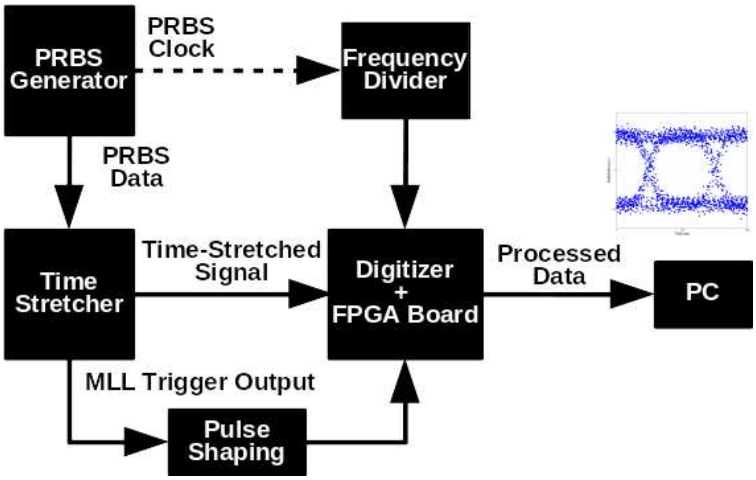

Figure 3.14: The setup for testing PRBS data. The stretch factor for 10 Gbit/s and 40 Gbit/s PRBS data setup were 50 and 100 respectively. The clock divider used for 10 Gbit/s and 40 Gbit/s PRBS data setup were 8 and 16 respectively.

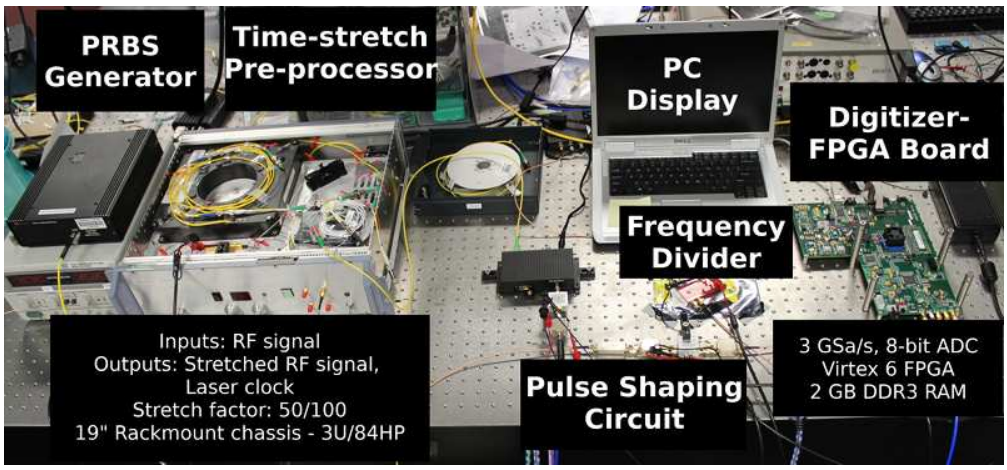

Figure 3.15: A photograph of the setup for testing PRBS data.

The setup for testing PRBS data at 10 Gbit/s and 40 Gbit/s is shown in Figure 3.14 and in 3.15. The stretch factor for 10 Gbit/s and 40 Gbit/s PRBS data setup were 50 and 100 respectively. The clock divider used for 10 Gbit/s and 40 Gbit/s PRBS data setup were 8 and 16 respectively.

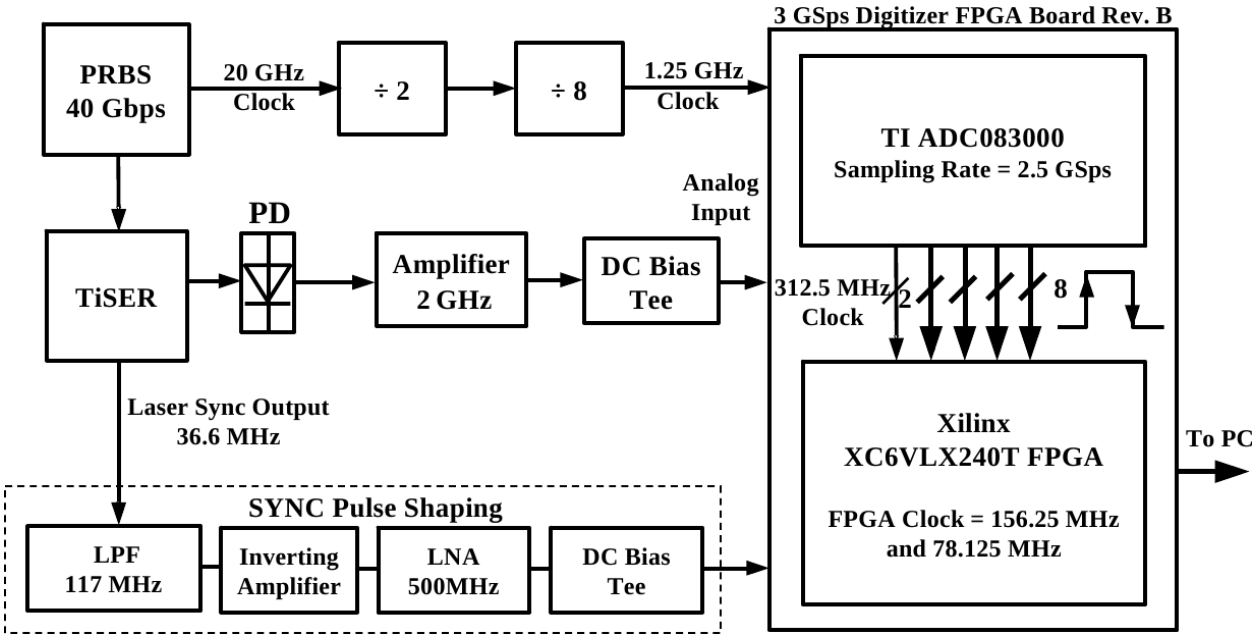

Figure 3.16: A detailed block diagram of the time-stretch accelerated processor for analyzing 40 Gigabit/s PRBS data.

A detailed block diagram of the TiSAP system for analyzing 40 Gigabit/s PRBS data is shown in Figure 3.16. The time-stretch front-end system is composed of TiSER which receives a high-speed electrical signal, in this case 40 Gigabit/s PRBS data, and produces two outputs: an optical output of the time-stretched laser pulse with the electrical signal modulated on it, and an electrical SYNC output from an internal photo-detector. The PRBS also outputs a clock signal at half it's data rate, which is 20 GHz, which is divided to produce the ADC sampling clock signal of 1.25 GHz, resulting in a sampling rate of 2.5 Giga-samples/s. For using the same system for 10 Gigabit/s PRBS data, the output clock from the PRBS generator was 10 GHz. Therefore, we would divide this 10 GHz clock output from the PRBS using a divide by 8 divider to generate the ADC sampling clock of 1.25 GHz.

The FPGA outputs the mode-locked laser pulse period, T_{MLL}, in term of sample points (see equation 3.2), and the 48 sample points corresponding to a frame to a local computer via USB 2.0 or to a remote computer or cloud via Gigabit Ethernet. Since the PRBS clock synchronizes both ADC and FPGA, the number of sample points that make up one unit interval (UI) of the PRBS can be determined. A MATLAB code uses this synchronization

count to generate the eye diagrams from the recovered data to measure the various signal integrity parameters.

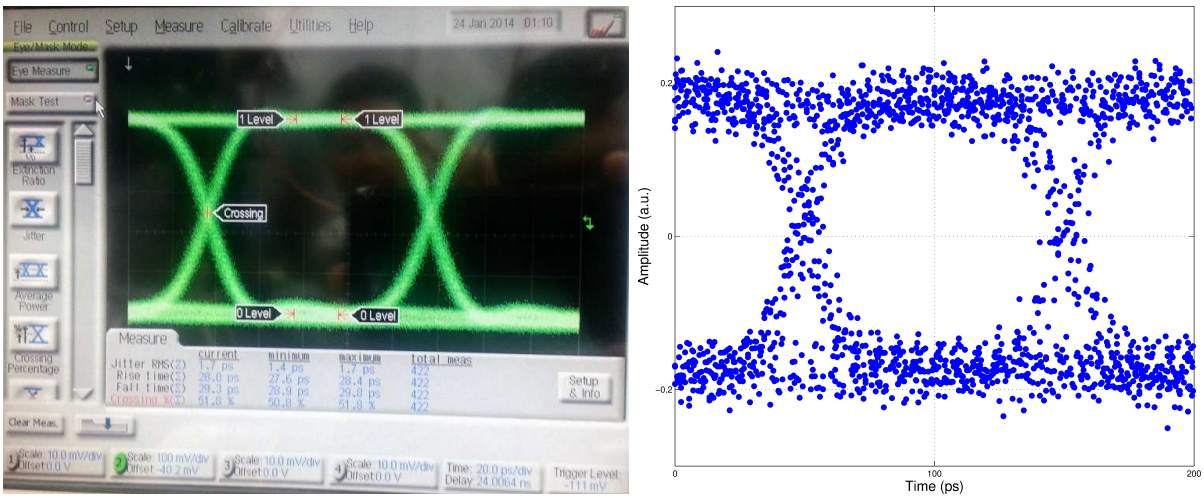

(a) Equivalent time sampling oscilloscope. (b) TiSAP.

Figure 3.17: Eye diagram of 10 Gigabit/s PRBS data

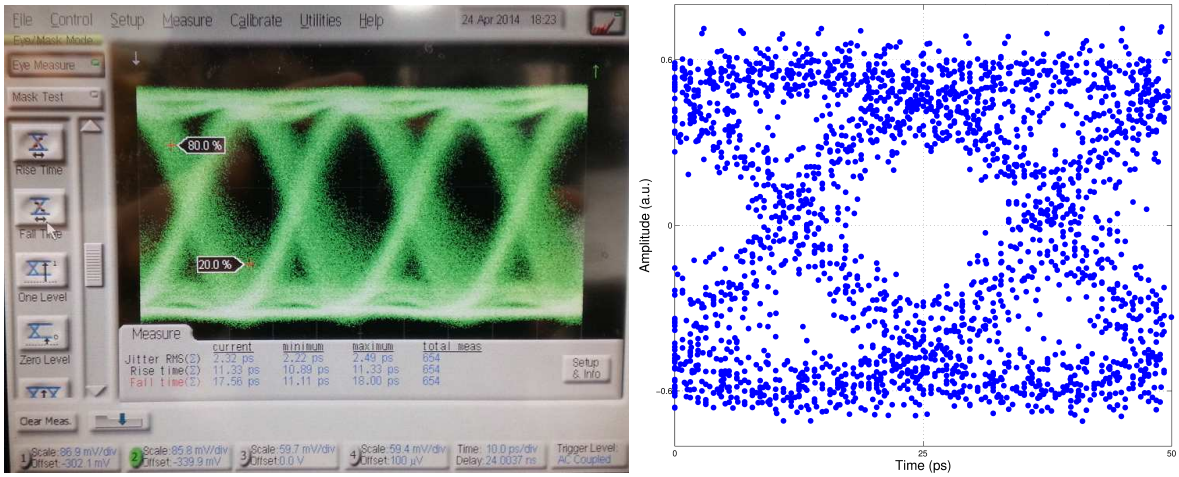

(a) Equivalent time sampling oscilloscope. (b) TiSAP. Courtesy of [121].

Figure 3.18: Eye diagram of 40 Gigabit/s PRBS data.

The eye diagrams obtained using TiSAP and the corresponding measurements employing an equivalent time sampling oscilloscope can be found at Figures 3.17 and 3.18. The jitter present in the eye diagrams in Figures 3.17(b) and 3.18(b) is primarily due to the one-sample point jitter in the framing module (see Section 3.3.2). The one-sample point jitter

corresponds to approximately less than one-tenth and one-sixth of a UI for 10 Gbit/s (stretch factor = 50) and 40 Gbit/s data (stretch factor = 100), respectively. The PRBS source used for 40 Gbit/s data had inherent rms jitter of 2.4 ps, the effect of which can be seen on the eye diagrams in Figure 3.18(a) and 3.18(b). Implementing interpolation on sample points can significantly reduce the jitter added by the framing module and thereby improving the quality of the eye diagrams produced for a low jitter PRBS generator.

3.5 Eye Pattern Measurements

The real-time burst sampling modality of TiSAP allows us to capture real-time long segments of the signal to be analyzed in a very short acquisition time of ∼28 µs. The captured samples within the real-time burst window of TiSAP are effectively sampled with one hundred times the sampling throughput of conventional techniques. This enables us to observe ultra-short single-events, transient effects, etc., which cannot be captured by conventional oscilloscopes. This section is adapted from [171], for which I jointly performed the experimental setups and data collection with Daniel Lam.

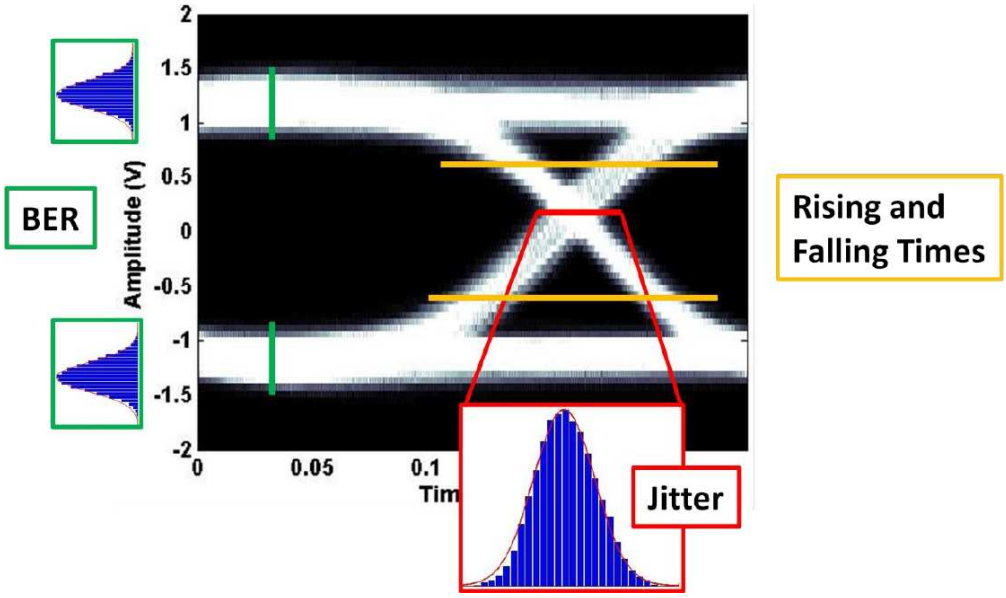

Figure 3.19: A sample eye diagram of 10 Gigabit/s data with the regions where statistical analyses are performed to estimate bit-error rate, jitter, and rise and fall times. Courtesy of [171].

The eye diagrams or otherwise called eye patterns of the modulated digital data generated by TiSAP can be used to perform various measurements. These measurements include but are not limited to bit-error rate (BER), jitter, rise and fall times, Q-factor, etc. Statistical analyses are performed on the eye diagrams as depicted in Figure 3.19 to estimate all these parameters representing the quality of transmission [171]. The measurements performed with TiSAP on 10 Gigabit/s PRBS/BERT data is compared with that from a BERT for BER and sampling oscilloscope for other parameters.

3.5.1 Bit-Error Rate Measurement

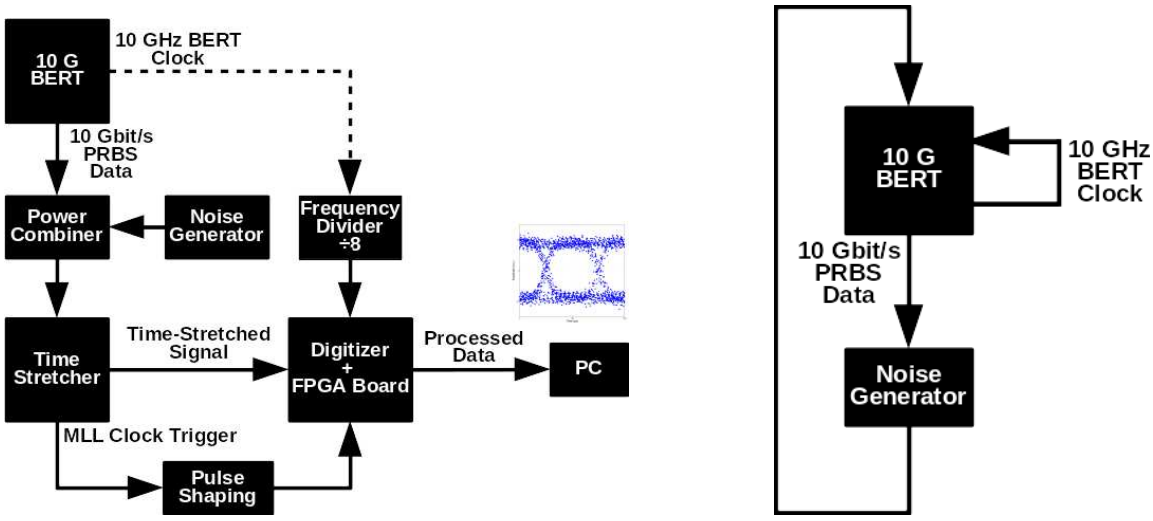

(a) TiSAP (b) BERT

Figure 3.20: The test setups for measuring BER using TiSAP and BERT for the same PRBS output.

The BER measurements performed using TiSAP on 10 Gigabit/s PRBS data generated by the BERT was compared against that reported by the BERT in loop-back mode. The BERT used was a Keysight Technologies' Centellax TG1B1-A, which is a 10 Gigabit/s pseudo-random bit sequence generator and bit error rate tester [172]. A bit error rate tester essentially consists of a pattern generator, which transmits a fixed test pattern to the device under test, an error detector connected to the output of the device under test counts the errors, and a clock generator to synchronize the pattern generation and error detection process. Some BERTs may have an optional communication analyzer to display the eye diagrams or optical-electrical or electrical-optical converters for supporting optical signals. The block diagram of the test setups using TiSAP and the BERT as the measurement instrument are shown in Figures 3.20(a) and 3.20(b) respectively.

(a) BERT

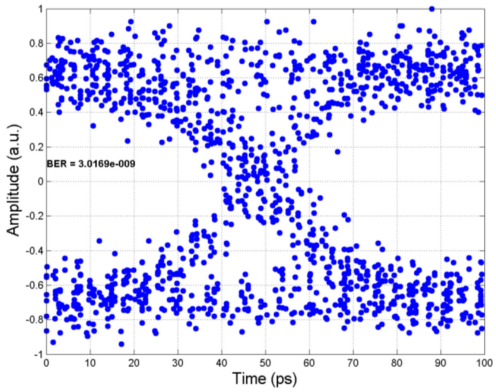

(b) TiSAP

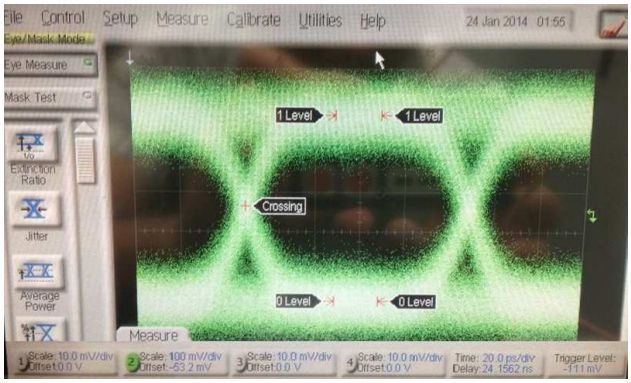

(c) Equivalent time sampling oscilloscope

Figure 3.21: The comparison of a BER measurement of 10 Gbit/s data using TiSAP and BERT for the same PRBS output with noise as well the eye diagrams obtained using TiSAP and an equivalent time sampling oscilloscope. Courtesy of [171].

We used a wideband avalanche diode noise generator, Agilent 346C, to add noise to the PRBS output of the BERT to increase the bit error rate. This noise source produces an output with a noise spectrum from 10 MHz to 26.5 GHz, when 28V is applied to it's DC power terminals [173]. The noise output combined with the signal was sent to the TiSAP and also in a separate experiment, as seen in Figures 3.20(a) and 3.20(b), to the receiver and error detector unit of the BERT where the bits were compared to the transmitted signal obtain the BER. Experiments were conducted to sweep the signal BER values within the range of $10^{-}3$ to 10^{-12}. For extremely small BER values, less than 10^{-12}, the BER reported by TiSAP were three orders of magnitude off from the BERT. This is due to the statistical nature of BER estimation from eye diagrams as opposed to the deterministic error counting for every

data symbol by the BERT. For larger BER conditions of the signal, the BER estimated by the TiSAP matched within less than an order of magnitude of the BERT. More extensive comparison of the BER for various test environments for optical fiber communication systems is reported in Section 4.3.

3.5.2 Jitter, Rise, and Fall Time Measurement

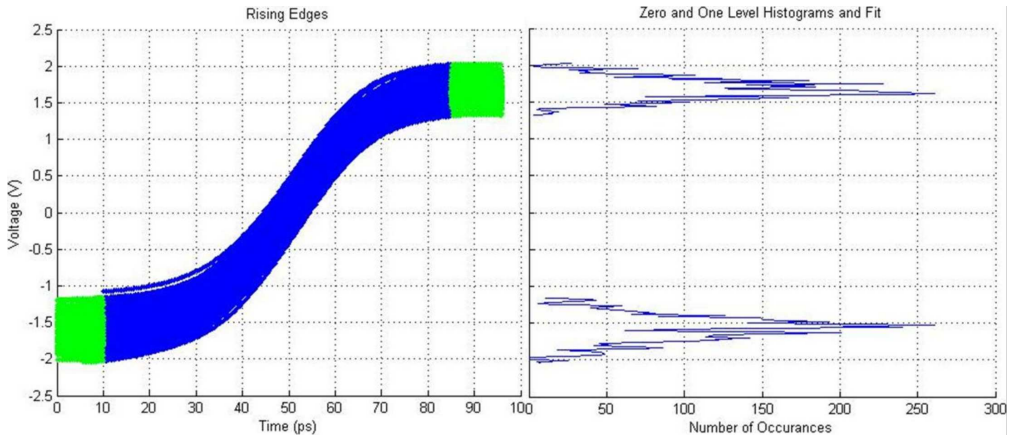

Figure 3.22: The determination of the mean value of logic HIGH and LOW levels from the eye diagram of 10 Gigabit/s data. Courtesy of [171].

Jitter is an important parameter of integrity of transmitted data and severely degrades the signal-to-noise ratio. Jitter in the signal is assumed to be due to random noise following a Gaussian distribution. Therefore the data jitter is estimated by generating a histogram of the eye diagram and applying a Gaussian curve fit on the histogram at the crossing point of the eye diagram. The mean value of the HIGH and the LOW levels of the signals are determined from the histogram as shown in Figure 3.22 [171].

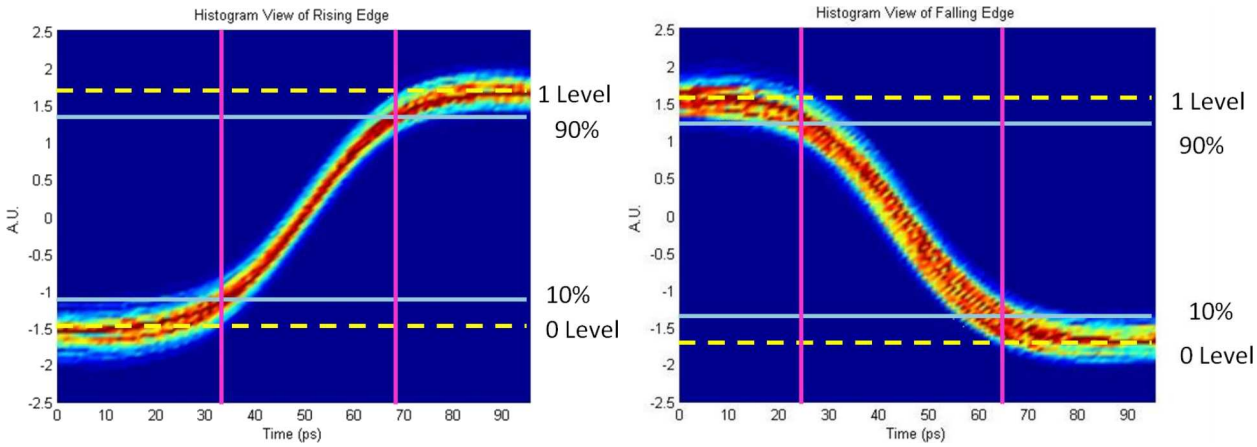

(a) Rise time estimation

(b) Fall time estimation

Figure 3.23: The rise and fall time estimation from the histograms of the rising and falling edges in the eye diagram, respectively. The time interval between the purple lines gives the rise and fall times from the respective histograms. Courtesy of [171]

The rise and fall times are also estimated from the histogram of the eye diagrams. The rise time was measured by determining the time it takes for the signal level on the rising edge to reach from 10% to 90% of the mean HIGH level and vice versa for fall time estimation as shown in Figure 3.23 [171]. The time interval between the purple lines gives the rise and fall times from the respective histograms.

Table 3.4: Comparison of TiSAP estimated jitter, rise and fall time for 10 Gigabit/s data with that reported by 16 GHz analog bandwidth, 50 Giga-samples/s real-time oscilloscope, Tektronix DPO71604C [171].

Parameter	**TiSAP**	**Real-time Oscilloscope**
Jitter (ps)	3.6	3.5
Rise time (ps)	39.3	42
Fall time (ps)	39.5	42.4

The statistically estimated jitter, rise, and fall times from the eye diagram measurements obtained using TiSAP were compared to that from a real-time oscilloscope, Tektronix

DPO71604C, which has an analog bandwidth of 16 GHz and 50 Giga-samples/s sampling rate. A comparison of the estimated jitter, rise, and fall times by TiSAP with the measurements observed on the real-time oscilloscope is shown on Table 3.4 [171]. We find that the estimated signal integrity parameters by TiSAP is comparable to the measurements performed using a real-time oscilloscope. The better rise and fall times reported by TiSAP over the real-time oscilloscope can be attributed to the higher sampling throughput of TiSAP (2.5 times) which results in having lot more sample points in the rising and falling edges of the signal.

3.6 Discussion

Table 3.5: Comparison of the specifications of TiSAP with a sampling oscilloscope

Specification	**Sampling Oscilloscope**	**TiSAP**
Measurement time	seconds to minutes.	28 µs for eye diagram 27 ns – single-shot
Equivalent sampling rate	Several Mega-sample/s	250 GSps Burst sampling throughput using time-stretch.
Maximum bandwidth	100 GHz	40 GHz (limited by modulator which can go up to 110 GHz) and dispersion penalty (can be mitigated to extend to Terahertz)
Jitter	1 ps RMS	150 fs; 5.5 fs RMS (single-shot)
Power	400–700 W	50 W

TiSAP is extremely power efficient, consuming only 50 W when used with a 3 GSps digitizer and an FPGA to perform digitization and measurement analyses as compared to over 400

W for a commercial bench-top equivalent-time sampling oscilloscope. A comparison of the various features and specifications of TiSAP with a sampling oscilloscope can be found on Table 3.5.

3.6.1 Acquisition Time

The MLL repetition rate was ∼27.2 ns, and real-time eye diagrams are generated for every 1024 laser pulses. Therefore, the acquisition time of TiSAP is ∼28 microseconds (1024*27.2 ns), which is significantly lower than that of equivalent-time oscilloscopes. For the eye diagrams shown in Figure 3.17(b) and 3.18(b), as mentioned earlier, the acquisition time for real-time TiSAP is ∼28 microseconds, while the acquisition time for sampling oscilloscope exceeds two minutes. This makes TiSAP ideally suited for feedback control in optical networks employing software-defined network (SDN) controllers. The effective burst-mode sampling rate for TiSAP is 250 GSamples/s for 40 Gigabit/s data testing, which is considerably higher than real-time oscilloscopes for the same degree of resolution, thereby implementing an equivalent 2 Terabit/s (2.5*100*8) burst-mode processor for signal integrity measurements.

3.6.2 Bandwidth and Dispersion Penalty

The analog bandwidth of time-stretch techniques are limited by dispersion penalty [113,114]. There are various techniques to overcome the dispersion penalty limit on the bandwidth of time-stretched ADC and are discussed in Section 2.7. Overcoming the dispersion penalty would result in an intrinsic bandwidth of 16 GHz × 100 = 1.6 THz. However, the practical bandwidth is limited by the electro-optic modulator used which is 40 GHz in the reported implementation. EOM bandwidth well above 100 GHz has been reported [80–82] and therefore can be used to extend the TiSAP measurement bandwidth to beyond 100 GHz. Even though commercial real-time oscilloscopes have attained analog bandwidths of over 80 GHz, the resolution of ADCs at very high frequencies diminish due to reduction in the effective number of bits [90,91,94].

3.6.3 Measurement Jitter

The timing jitter for the mode-locked laser was 150 fs (rms). The aperture jitter of the back-end digitizer used, National Instruments' ADC083000, was 550 fs (rms) and the stretch factor (M) of TiSAP implementations were ∼50 and ∼100 for 12.5/10 G-bit/s and 40 Gbit/s PRBS data, respectively. Therefore, based on equation 2.8, the measurement jitter is ∼150 fs.

If TiSAP is used in single-shot mode, the intra-pulse jitter of TiSAP, based on equation 2.9, is therefore ∼11 fs (550/50) and ∼5.5 fs (550/100) for stretch factors of 50 and 100, respectively, which is extremely low compared to the intrinsic jitter suffered in state-of-the-art conventional electronic digitizers [130]. This results in very accurate single-shot time-domain measurements compared to measurements by real-time oscilloscope, where the jitter added by the instrument has to be very accurately estimated and corrected.

3.7 Future Work

Future work needs to be done to improve the throughput and performance of the TiSAP system. Replacing the floating point divider IP core with a custom designed fixed point divider with the sufficient precision can reduce the FPGA logic resource utilization and increase the throughput of the system. Gigabit Ethernet can be employed to speed up the transfer speed of processed data to the computing platform, which may be either locally or remotely available. A PCI-Express 3.0 interface based digitizer FPGA board can be designed to significantly increase the data transfer rate to a local PC.

Interpolation in the time-domain on the synchronized frames has shown to improve the single-point jitter arising from the framing module. This interpolation step needs to be integrated with the rest of the FPGA logic to significantly reduce the jitter caused by the framing module. The post processing of the eye diagrams for signal integrity analysis are performed on the computer in the presented system. These signal integrity measurements on the generated eye diagrams could also be integrated within the FPGA without using

the on-board RAM or software. An optical time-stretch system can be employed with a coherent receiver and used at the front-end to enable a modulation format agnostic optical performance monitoring system that avoids the need for optical to electrical conversions. Such a system would also extend the usability of TiSAP to coherent optical communication applications.

3.8 Conclusion

We have demonstrated in-service eye diagram generation and BER estimation of 40 Gbit/s data using a 2 Terabit/s burst-mode processing TiSAP system, consisting of a time-stretch front-end and a customized electronic back-end. TiSAP has an effective sampling rate of 250 GSamples/s, and a very fast acquisition time of ∼28 microseconds. The time-stretch accelerated processor can perform BER estimation for data rates up to 40 Gbit/s, which is limited by the bandwidth of the electro-optic modulator and dispersion penalty. This technology is well suited for and aimed at ultra-fast, in-service, digital performance monitoring for optical networks such as degradation/fault detection, correlation and localization, reliable signaling to notify other nodes, efficient routing algorithms, bandwidth management, fast network restoration schemes, and as a high bandwidth RF signal analysis tool. The proposed burst-mode real-time, in-service, optical performance monitoring solution can provide necessary feedback to the SDN control plane to implement agile optical transport networks. Extension of the single channel time-stretch front-end to a parallel array can extend the current burst-mode operation to continuous-time [115].

CHAPTER 4

Applications of TiSAP

The applications of time-stretch accelerated systems for enabling ultra-fast monitoring of optical and electrical signals and for production-level device testing in high bandwidth communication systems are reported. The presented bit error rate based optical performance monitoring system has an acquisition speed of ∼28 µs. The ultra-fast measurements by TiSAP enables advanced device-level software-defined networking features to implement agile optical networks. Integration of TiSAP to an optical test-bed to study the performance of optical aggregation networking including the effects of amplified spontaneous emission noise and self phase modulation is presented. The experimental demonstration of TiSAP implementing an agile optical network which adapts based on the quality of transmission is reported. Experimental demonstration of the first real-time, in-service, signal integrity analysis of 10 Gigabit/s non-return-to-zero on-off keying modulated streaming video packets in a commercial platform is also presented. A TiSAP based production-level opto-electronic/electro-optic device testing system is proposed. An instantaneous frequency measurement system based on time-stretch is also reported.

4.1 Introduction

The goal to implement efficient agile optical networks is a multi-university collaboration involving the University of Arizona (UA), Columbia University, University of California Los Angeles (UCLA), University of Southern California (USC), and Cornell University. Testbed for Optical Aggregation Network (TOAN) located in the College of Optical Sciences at the University of Arizona, Tucson. TOAN testbed is part of the National Science Foundation

(NSF) funded Engineering Research Center (REC), Center for Integrated Access Networks (CIAN). CIAN is a multi-institutional research effort consisting of the University of Arizona (Lead), University of California at Los Angeles, University of California at San Diego, University of California at Berkeley, University of Southern California, Columbia University, California Institute of Technology, Cornell University, Norfolk State University, and Tuskegee University.

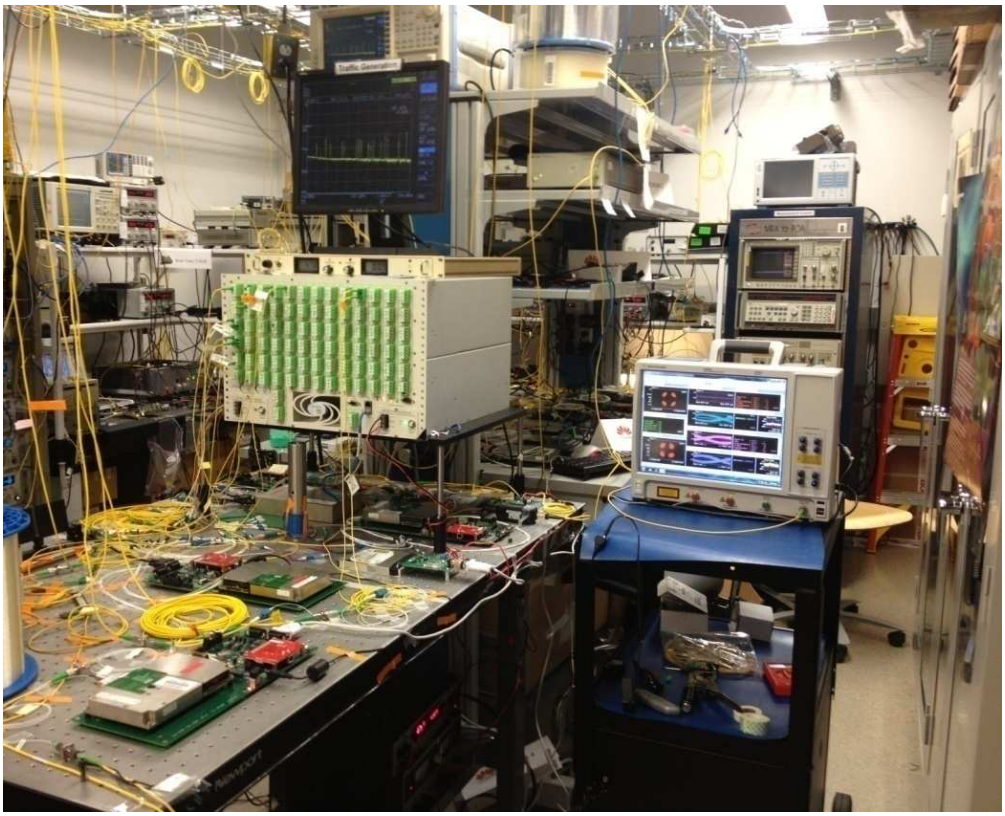

Figure 4.1: Photograph of the Testbed for Optical Aggregation Network (TOAN) located in the College of Optical Sciences at the University of Arizona. Courtesy of [171].

TOAN, shown in Figure 4.1, is a network emulation testbed for studying performance of a non-ideal, metro-scale aggregation networks and for developing and testing agile optical software-defined networks. TOAN testbed provides multiple programmable network elements including microelectromechanical systems (MEMS) based optical space switches, wavelength selective switches (WSS), reconfigurable optical add-drop multiplexers (ROADM), etc., and a customizable control plane to enable implementation of dynamically reconfig-

urable optical networks. The TOAN testbed has the capability of generating a variety of optical traffic such as 1-10 Gigabit Ethernet, OOK, dual-polarization quadrature phase-shift keying (DP-QPSK), orthogonal frequency-division multiplexing (OFDM), synchronous optical networking (SONET)/synchronous digital hierarchy (SDH), etc. [174].

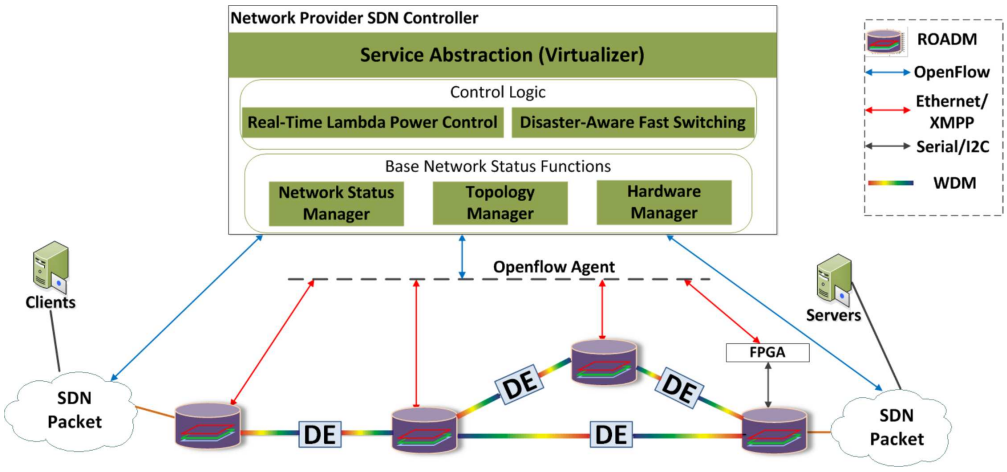

Figure 4.2: Block diagram of the TOAN testbed and its control and management protocols employing an SDN controller

The testbed network topology shown in Figure 4.2 consist of four nodes which are connected using distance emulators (DE), which enables generation of transmission impairments to study the associated instability and uncertainty in a full-scale metro-area network. The testbed includes over 20 WSS and more than 10 erbium-doped fiber amplifiers (EDFA) with a total of 17 wavelengths injected into the network. Multiple 10 Gigabit/s OOK signals, an OFDM signal, as well a 40 Gigabit/s dual-polarization QPSK signal are among the various signals injected into the network. The testbed is also connected to a Fujitsu Flashwave 9500 optical networking platform utilizing a 10 Gigabit/s NRZ OOK transmission. The testbed consists of a software-defined networking controller employing the OpenFlow protocol [70]. The interface connecting the various network elements to the control plane is either using Ethernet or via Extensible Messaging and Presence Protocol (XMPP). This section, especially the description of the distance emulator, is adapted from [175].

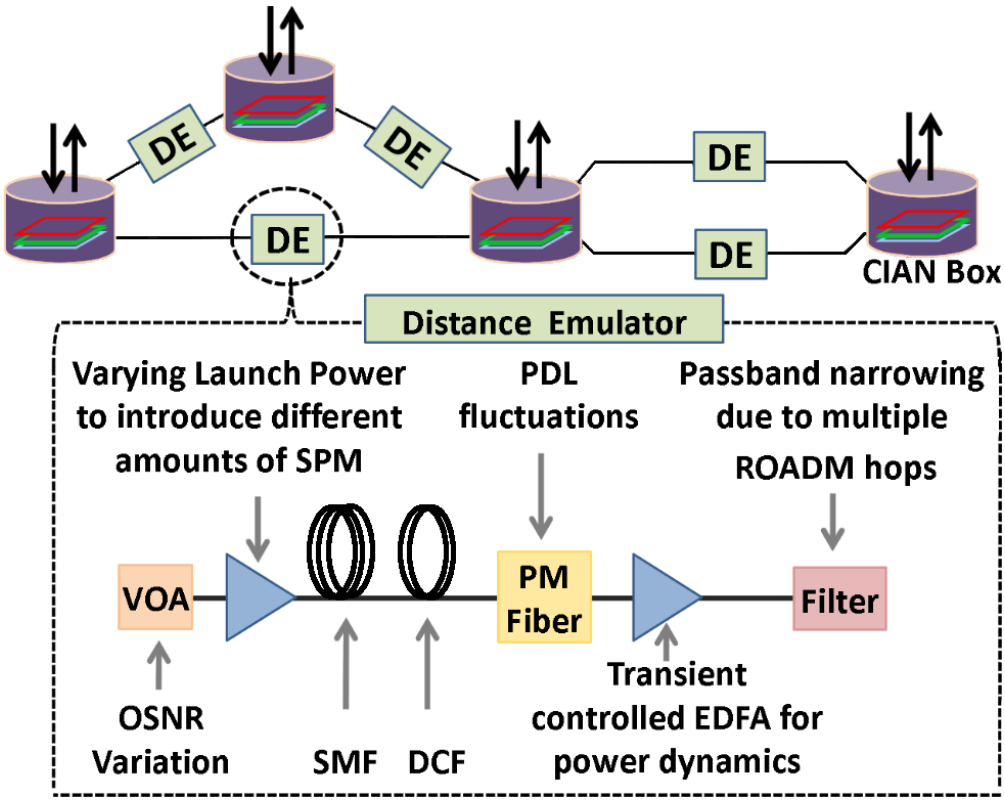

Figure 4.3: Distance emulator setup and its operation. Courtesy of [175].

Distance emulator employed in the testbed, shown in Figure 4.3 allows for injecting individual or multiple transmission impairments to study their impact and test the agility of the implemented re-configurable network. The implemented distance emulator can produce the effect of up to 20 hops of transmission. The various impairments introduced using the distance emulator are: (i) Self-Phase Modulation (SPM), (ii) OSNR degradation, (iii) Amplified Spontaneous Emission (ASE) noise, and (iv) Polarization Dependent Loss (PDL). The quality of transmission in the distance emulator is limited by OSNR at low optical launch powers and by non-linear effects at high launch powers. The distance emulator consists of a 40 km single-mode fiber (SMF) spool with dispersion compensation, and a tightly coiled polarization maintaining (PM) fiber to introduce PDL fluctuations in the signal. OSNR of the input signal can be degraded by injecting ASE noise. The ASE noise added signal is transmitted through a transient controlled EDFA in which the transients occur due to dynamic channel add-drop and PDL fluctuations [175].

4.2 Integration of TiSAP into TOAN Testbed

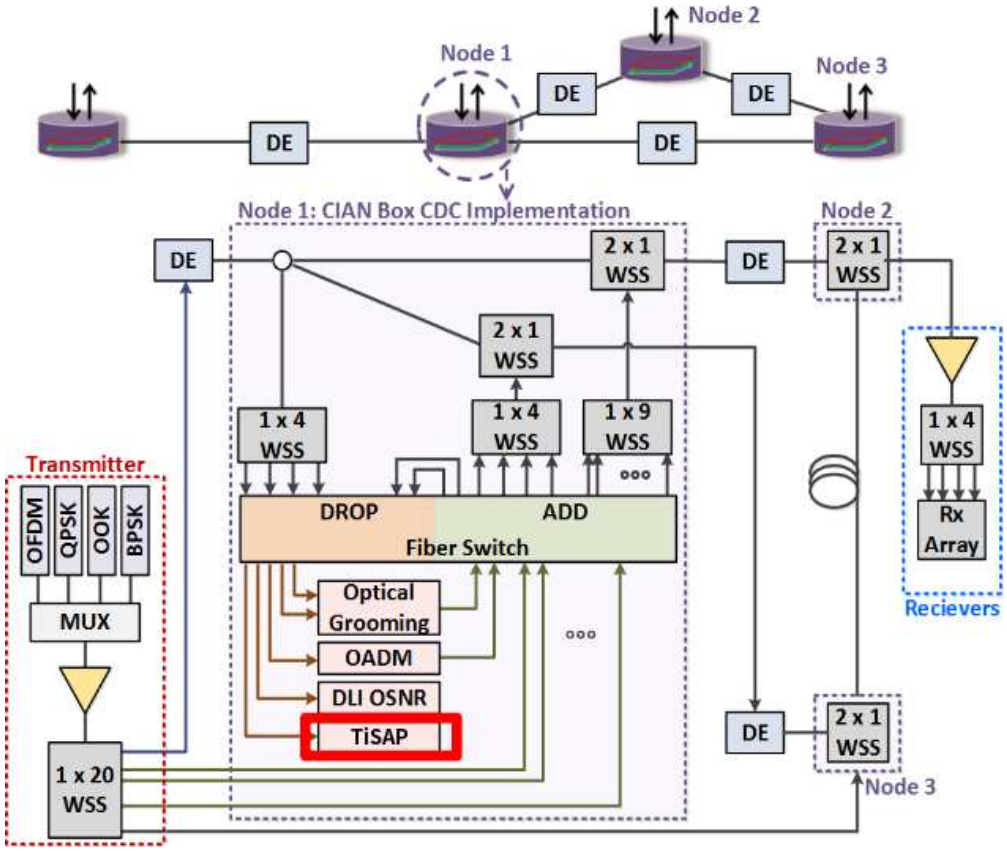

Figure 4.4: A detailed block diagram of CIAN Box used in the TOAN testbed. DE: Distance Emulator, WSS: Wavelength Selective Switch, OADM: Optical Add/Drop Multiplexer, DLI: Delay Line Interferometer, OSNR: Optical Signal-to-Noise Ratio, TiSAP: Time-Stretch Accelerated Processor, OFDM: Orthogonal Frequency-Division Multiplexing, DP-QPSK: Dual-Polarization Quadrature Phase Shift Keying, OOK: On/Off Keyed. Courtesy of [171].

Dynamic reconfiguration in the networking nodes is enabled by inserting into each node a unique platform called, CIAN Box, developed by the teams from Columbia University and University of Arizona. A detailed block diagram of the testbed with the CIAN Box architecture can be found in Figure 4.4. The CIAN Box consists of switching plane utilizing a Calient Technologies 260x260 fiber switch to implement a colorless, directionless, and contentionless (CDC) ROADM architecture. An optical performance monitoring plane is necessary to detect degradation in the quality of transmission due to impairments. Therefore, an OPM

plane consisting of an optical signal-to-noise ratio (OSNR) measurement technique employing a delay-line interferometer (DLI) developed by the team from University of Southern California, and a BER estimation employing TiSAP were integrated into the CIAN Box to consistently monitor the quality of the optical signals. TiSAP performs ultra-fast measurements on the optical signals to estimate signal integrity parameters such as BER, jitter, and rise and fall times. The CIAN Box also consist of a control plane implemented using an SDN controller, which receives the OPM measured data to perform appropriate dynamic reconfiguration of the network parameters and topology.

4.3 Optical Performance Monitoring for Agile Networks

Next generation fiber optical communication networks are expected to have very low time to repair in the presence of impairments. This would require such networks to be smart, robust, re-configurable, flexible and secure [48]. The service protection in Dense Wavelength Division Multiplexed (DWDM) networks require efficient and accurate degradation/fault detection, correlation and localization, reliable signaling to notify other nodes, efficient routing algorithms, bandwidth management, etc. Optical performance monitoring (OPM) techniques that can execute fast measurements is necessary for implementing agile optical networks. TiSAP can perform signal integrity analysis of in-service data with an ultra-fast acquisition speed of ∼28 µs and provide feedback to the SDN control plane to initiate the corrective action. As shown in Figure 4.4, TiSAP integrated into the CIAN box to perform in-service BER measurements on a 10 Gigabit/s NRZ OOK optical data. TiSAP periodically sends the estimated BER of the optical data via XMPP to the SDN controller for enabling it to tune the network parameters appropriately to ensure high QoT. We demonstrated the ability of the implemented agile network to recover from disaster by switching the affected wavelengths to another route based on the OSNR and BER of the optical signals [175].

4.4 Characterization of Amplified Spontaneous Emission Noise

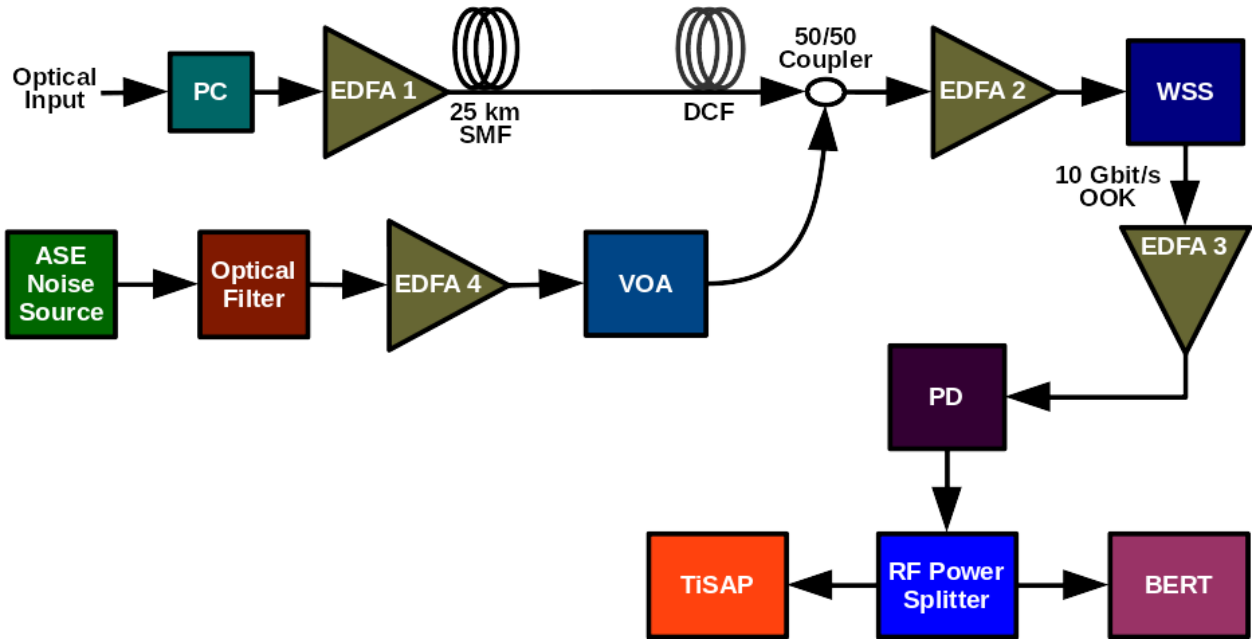

Figure 4.5: The setup for studying the effect on BER of 10 Gigabit/s NRZ OOK optical signal due to ASE noise using TiSAP and comparison with a BERT. PC: Polarization Controller, EDFA: Erbium Doped Fiber Amplifier, VOA: Variable Optical Attenuator, WSS: Wavelength Selective Switch, PD: Photo-diode, TiSAP: Time-Stretch Accelerated Processor, BERT: Bit-Error Rate Tester

The erbium-doped fiber amplifiers used in optical communication networks introduce amplified spontaneous emission noise. Amplification occurs in EDFAs when an input optical signal photon arrives at an excited erbium (Er^{3+}) ion along the optical fiber core and stimulates its decay from the metastable level to the ground state. However, if the Er^{3+} ions that do not interact with the input optical signal photon, it can decay to the ground state spontaneously, emitting photons in random phase and direction. These randomly emitted photons after getting amplified results in amplified spontaneous emission degrading the OSNR of the input optical signal [176]. ASE noise degrades the performance of intensity modulation direct detection (IM/DD) as well as coherent receivers. The extent of degradation depends on the number of amplifiers employed, which would be extremely severe for long-haul networks

that use tens of EDFAs along the fiber link. Even for short-range fiber links with in-line EDFAs, an optical pre-amplifier is often employed to amplify the signal or local oscillator [6]. Therefore it is very important to estimate the effect of ASE noise in the optical networks and to design the links to minimize degradation in OSNR due to it.

The experimental setup for performing optical performance monitoring of a metro-scale network subjected to ASE noise and SPM, shown in Figure 4.5, is implemented by modifying the distance emulator shown in Figure 4.3. The optical signal from a node which includes multiple wavelengths including the 10 Gigabit/s NRZ OOK data is amplified by EDFA 1 optical amplifier, and transmitted through a 25 km single-mode fiber spool with dispersion compensation. The dispersion compensated optical signal is combined with the output of a filtered and amplified (EDFA 4) ASE noise source with variable optical attenuation using a 50/50 optical coupler. The combined signal is further amplified using EDFA 2 before input to a wavelength selective switch while performing ASE noise injected testing of the network. While testing the for effect of SPM, the optical signal from the VOA(from ASE noise source) to the coupler is turned OFF and the output power of EDFA 1 is increased to cause SPM. The WSS at the output of EDFA 2 selects the wavelength corresponding to the 10 Gigabit NRZ OOK signal to be analyzed and is further amplified (EDFA 3) and converted to an electrical signal using a photo-diode. The output of the photo-diode is amplified electrically, power-split, and input to both TiSAP and a BERT for comparing the BER measurements.

The ASE noise source signal path in the experimental setup shown in Figure 4.5 is utilized to characterize the effect on signal BER to various OSNR degradation levels due to the injected ASE noise. The launch power of the optical signal amplified by EDFA 1 has to be low enough to ensure that no SPM is injected into the link. The filter and EDFA 4 are used in combination to boost the ASE noise around the wavelength of the signal of interest, which is the 10 Gigabit/s NRZ OOK data. The noise is filtered to be within 5 nm bandwidth around the signal wavelength. The received electrical signal is inputted to both TiSAP and a BERT to compare the results. The OSNR of the signal can also be measured using an optical spectrum analyzer (OSA) to analyze the signal at the output of the 50/50 optical coupler.

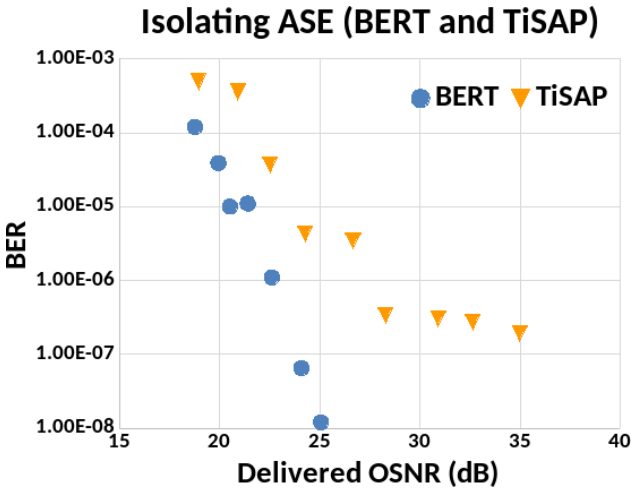

Figure 4.6: The comparison of the BER measured for various levels of OSNR degradation based on ASE noise injection. The BER estimated by TiSAP is comparable to that measured by the BERT at high ASE noise levels, i.e., at lower BER. At very low or no ASE noise injection to the system, the BER estimated using TiSAP will be higher than BERT. This is due to the statistical nature of BER estimation from eye diagrams in TiSAP as opposed to the deterministic error counting for every data symbol by the BERT.

The ASE noise source is first turned OFF with maximum attenuation setting for the variable optical attenuator for ensuring the best quality of transmission and the corresponding eye diagram are generated using TiSAP and the BER is estimated. The BER is also measured using a BERT concurrently to compare with TiSAP. The ASE noise source is then turned ON and the attenuation of the variable optical attenuator is gradually decreased and the corresponding eye diagrams and BER measurements are performed until the BER falls to 10^{-3}. A comparison of the BERs for various levels of ASE noise injection measured by TiSAP and a BERT can be found in the plots of BER vs delivered OSNR shown in Figure 4.6. The BER reported by TiSAP is comparable to that reported by the BERT at high ASE noise levels, i.e., at lower BER. When there is extremely low or no ASE noise injected into the system, the BER estimated using TiSAP will be higher than what is measured by the BERT. This is due to the statistical nature of BER estimation from eye diagrams in TiSAP as opposed to the deterministic error counting for every data symbol by the BERT as can

be seen in Section 3.5.1.

4.5 Characterization of Self Phase Modulation

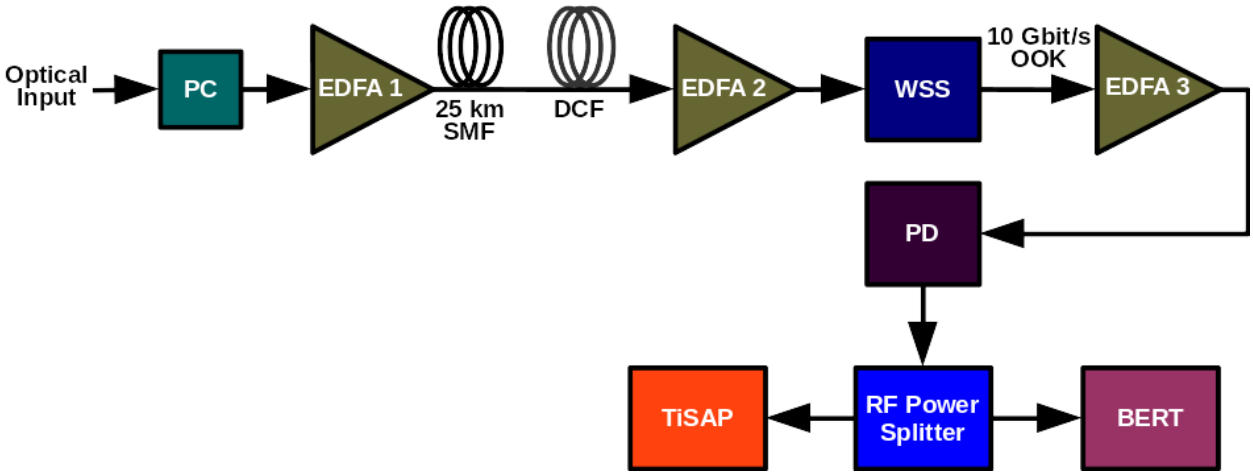

Figure 4.7: The setup for studying the effect on BER of 10 Gigabit/s NRZ OOK optical signal due to self phase modulation in the link, using TiSAP and for comparing it with a BERT. PC: Polarization Controller, EDFA: Erbium Doped Fiber Amplifier, WSS: Wavelength Selective Switch, PD: Photo-diode, TiSAP: Time-Stretch Accelerated Processor, BERT: Bit-Error Rate Tester

Self phase modulation is a non-linear optical effect that arises because of the refractive index of the fiber having an intensity-dependent component. An ultra-short pulse of light propagating through an optical fiber can induce a variation in the refractive index of the fiber due to optical Kerr effect [177]. This nonlinear refractive index results in an induced phase shift which is proportional to the intensity of the pulse. This gives rise to chirping of the pulses which in turn increases the pulse-broadening effects due to chromatic dispersion. The pulse chirping effect is also proportional to the transmitted signal power, therefore optical networks suing high transmitted powers suffer from high SPM effects. High-bit-rate systems have strict chromatic dispersion limitations and therefore SPM-induced chirp is a very important impairment to be mitigated. For optical links employing transmission rates of 10 Gigabit/s and beyond, or for lower-bit-rate systems that use high transmitted powers,

SPM can significantly increase the pulse-broadening effects of chromatic dispersion [178]. Therefore, an accurate and fast method for optical performance monitoring that can detect SPM based impairments in such optical networks will be very beneficial.

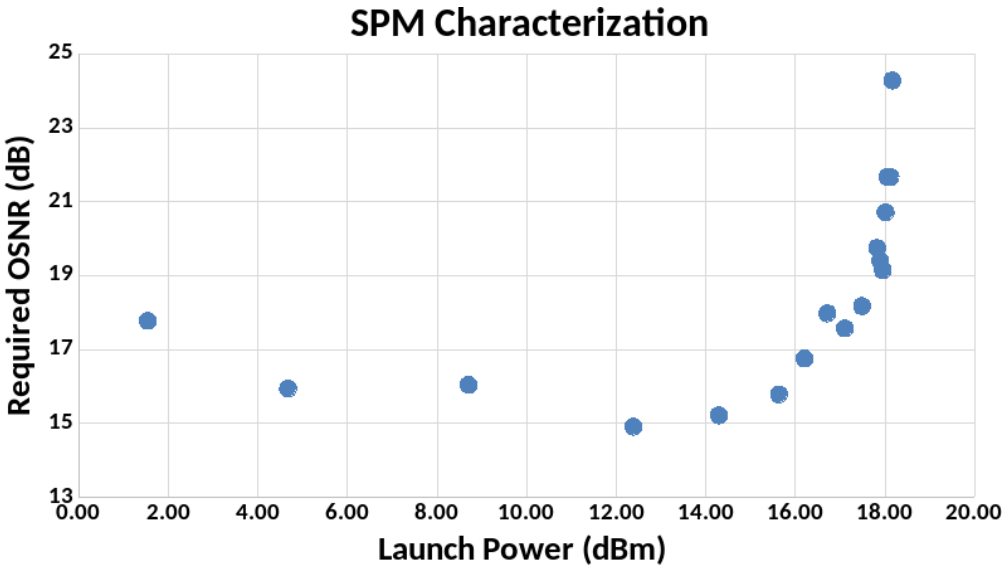

Figure 4.8: Characterization of SPM for the optical network. The required OSNR increases at higher launch powers due to increased SPM effects. As can be seen from the plot the effect of SPM increases significantly for fiber input powers higher than 12 dBm.

The experimental setup shown in Figure 4.7 is used to isolate the effects of SPM on the BER of the signal of interest, 10 Gigabit/s NRZ OOK transmission. This setup is very similar to the one shown in Figure 4.5, except for the absence of ASE noise injection signal path and the associated 50/50 coupler. The amplifier, EDFA 1, allows launching of different signal power into the long SMF fiber allowing us to control the injection of SPM into the optical network. For higher launch power, the amount of injected SPM into the network will be higher. Before studying the effect on BER, it is important to characterize the required OSNR in the presence of SPM in the link for various launch powers and this is accomplished by varying the gain of EDFA 1. The OSNR of the signal is measured by employing an optical spectrum analyzer at the output of the wavelength selective switch. A plot of the required OSNR vs. launch power is shown in Figure 4.8. As can be seen from the plot, launch powers over 12 dBm into the fiber will inject high enough self phase modulation

effects to significantly degrade the OSNR of the signal of interest. The effect of SPM on the eye diagram can be seen as vertical shifts in the amplitude of the signal resulting in an asymmetric eye diagram. Higher optical launch power into the fiber input induces an asymmetrical eye at the receiver and degrades the eye-opening resulting in higher bit-error rates [179, 180].

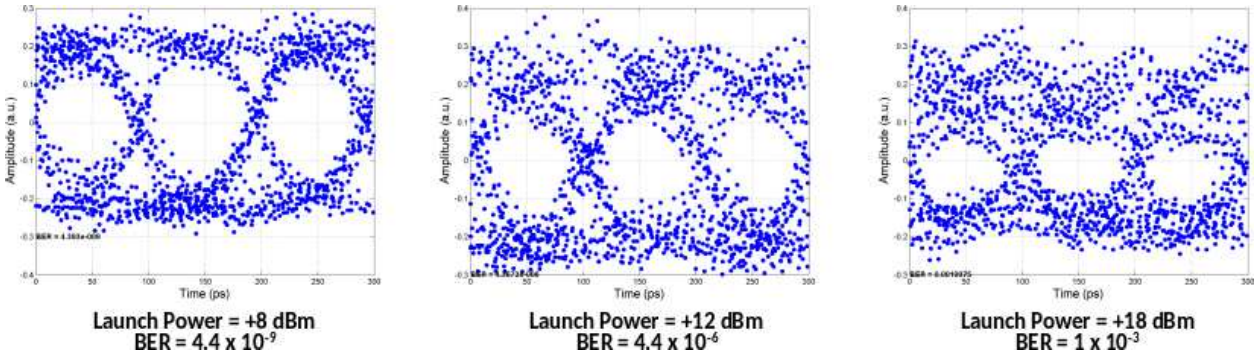

Figure 4.9: A comparison of the 10 Gigabit/s NRZ OOK eye diagrams captured by TiSAP for various launch power levels and the corresponding BERs.

Once SPM characterization is performed, the input is set to the lowest for ensuring the best quality of transmission with no SPM and the corresponding eye diagram are generated using TiSAP and the BER is estimated. The BER is also measured using a BERT concurrently to compare with TiSAP. The launch power is gradually increased and the corresponding eye diagrams and BER measurements are performed until the BER falls to 10^{-3}. Figure 4.9 shows the degradation in the eye diagrams captured by TiSAP and the estimated BER as the launch power is increased. These eye diagrams were recorded by TiSAP at a fast acquisition time of $\sim$28 µs. As expected, the eye patterns at high launch powers become asymmetric and degrade the quality of the signal.

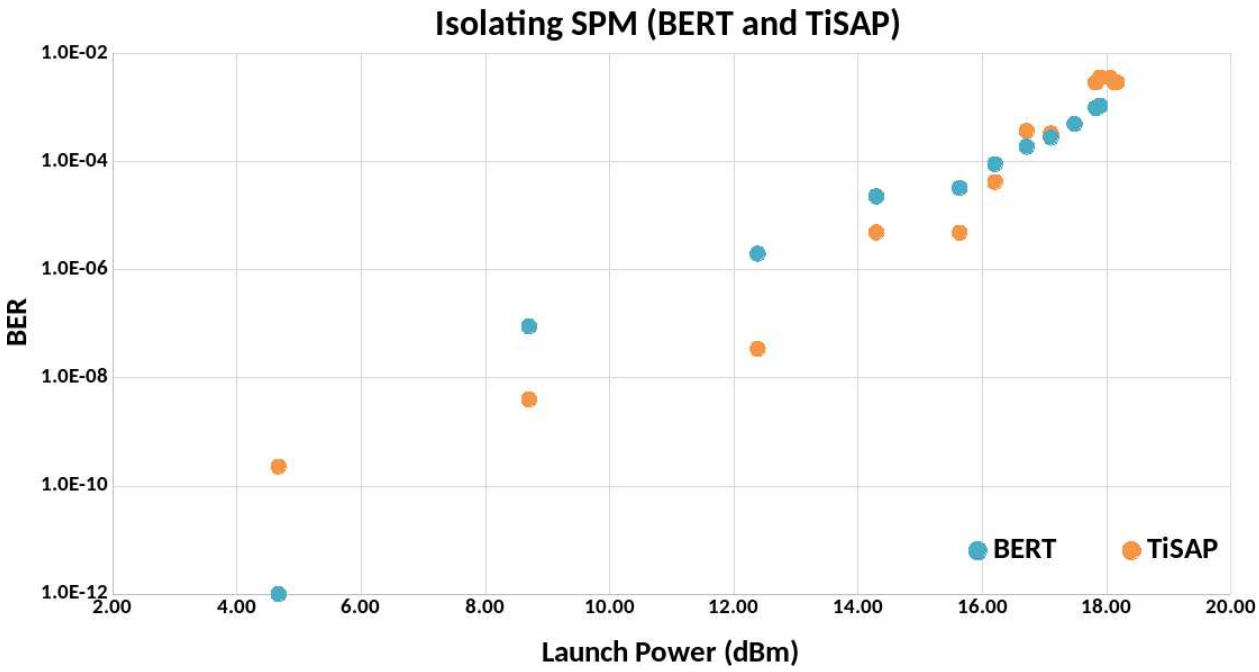

Figure 4.10: The comparison of the BER measured for various levels of OSNR degradation based on SPM injection. The BER estimated by TiSAP is comparable to that measured by the BERT at higher SPM injection, i.e., at lower BER. At very low or no SPM injection to the system, the BER estimated using TiSAP will be higher than BERT. This is due to the statistical nature of BER estimation from eye diagrams in TiSAP as opposed to the deterministic error counting for every data symbol by the BERT.

A comparison of the BERs for various levels of SPM injection measured by TiSAP and a BERT can be found in the plots of BER vs delivered OSNR shown in Figure 4.10. The BER reported by TiSAP is comparable to that reported by the BERT at high SPM noise levels, i.e., at lower BER. When there is extremely low or no SPM injected into the system, the BER estimated using TiSAP will be higher than what is measured by the BERT. This is due to the statistical nature of BER estimation from eye diagrams in TiSAP as opposed to the deterministic error counting for every data symbol by the BERT as can be seen in Section 3.5.1.

4.5.1 Time Traces of Optical Data Subjected to SPM

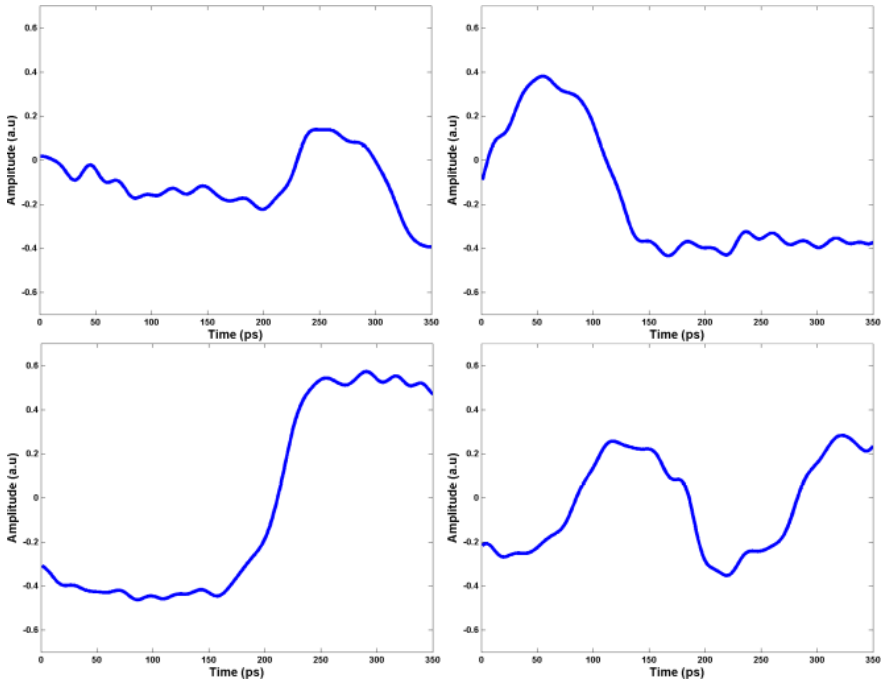

Figure 4.11: The time traces of the 10 Gigabit/s symbols captured by TiSAP in ∼28 µs. This cannot be achieved using conventional equivalent-time sampling oscilloscopes or real-time digitizers with limited sampling throughput.

A single time-stretched laser pulse contains multiple data symbols modulated on it depending on the pulse aperture time or the real-time burst window of TiSAP, which in turn depends on the dispersion value of the first dispersion compensating fiber (D1). The high sampling throughput (up to 250 Giga-samples/s) within this real-time burst window of TiSAP allows us to plot time traces of adjacent symbols in the data stream being analyzed. This is a very unique feature enabled by TiSAP which is impossible to achieve using equivalent-time sampling oscilloscopes. Real-time oscilloscopes on the other hand do not have high enough sampling rates to produce accurate time traces of very high-speed data. Figure 4.11 shows the real-time capture of the effects of SPM, at higher launch power, on 10 Gigabit/s NRZ OOK data transmission. As expected, the vertical shifts in the amplitudes of the adjacent symbols in time can be seen from the time traces of adjacent symbols captured in real-time within the aperture time window of TiSAP, which is impossible to capture or not accurate

enough using conventional techniques. The effect of SPM on the eye diagram of the received data can be captured using an equivalent time sampling oscilloscope, but after collecting data over long time periods of up to many minutes, whereas TiSAP only takes ∼28 µs. This unique feature of TiSAP enables the observation and study of ultra-fast events occurring in the signal due to non-linearity or even single-events if it is within the aperture time.

4.6 In-service Optical Performance Monitoring on a Commercial Platform

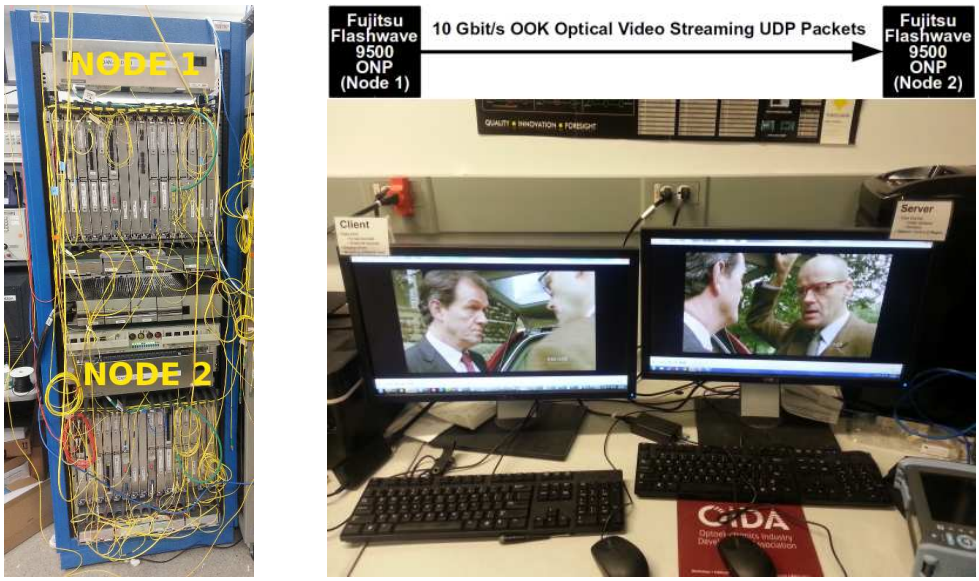

(a) (b)

Figure 4.12: Two Fujitsu Flashwave 9500 nodes at the TOAN laboratory.

Fujitsu Flashwave 9500 Packet Optical Networking Platform (ONP), shown in Figure 4.12(a), is a commercial optical networking platform by Fujitsu that can support up to 100 Gbit/s transponder and muxponder line cards. This platform can implement optical transport networks (OTN), 100G coherent optics, 88-channel pluggable ROADM, MEF-certified Carrier Ethernet, SONET, SDH, and Layer 1/2 traffic interworking [181]. This commercial platform is used by Internet and mobile service providers for mobile backhaul networks and residential broadband backhaul as well as various regional and metro-scale applications such as

enterprise networking services, flexible mesh optical networks etc.

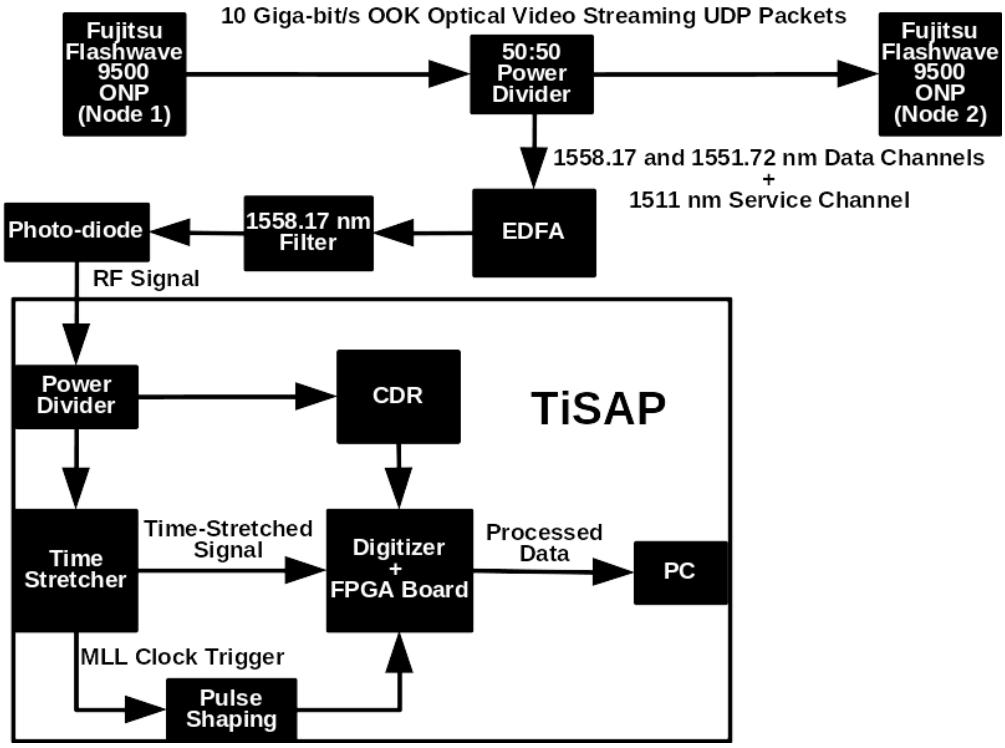

Figure 4.13: The experimental setup for real-time, in-service eye diagram analysis of 10 Gigabit/s NRZ OOK streaming video packets between two Fujitsu Flashwave 9500 nodes [56].

For the real-time, in-service, optical performance measurement, two such Fujitsu Flashwave 9500 nodes at the TOAN laboratory in the College of Optical Sciences, University of Arizona were used. Each node used a 10 Gigabit/s NRZ OOK modulation based transponder line card. From node 1, a high definition (HD) video was streamed to node 2 using User Datagram Protocol (UDP) packets as shown in Figure 4.12(b). As shown in Figure 4.13, the optical power going from node 1 to node 2 is tapped using a power divider and amplified by an Erbium Doped Fiber Amplifier (EDFA). There are three wavelengths present in the link that connect node 1 to node 2: the data channel at 1558.17 nm, another data channel at 1551.72 nm and a service channel at 1511 nm. The data channel wavelength, which has the video data, i.e., 1558.17 nm is filtered to remove the service channel wavelength and is then provided as input to a photo-diode receiver to obtain the electrical RF signal. The output of the photo-detector is power-divided and provided as an input to both the TiSER and the

CDR module. This is done in order to recover the data rate clock, which subsequently undergoes frequency division to generate the ADC clock frequency, which is half of its sampling rate [56].

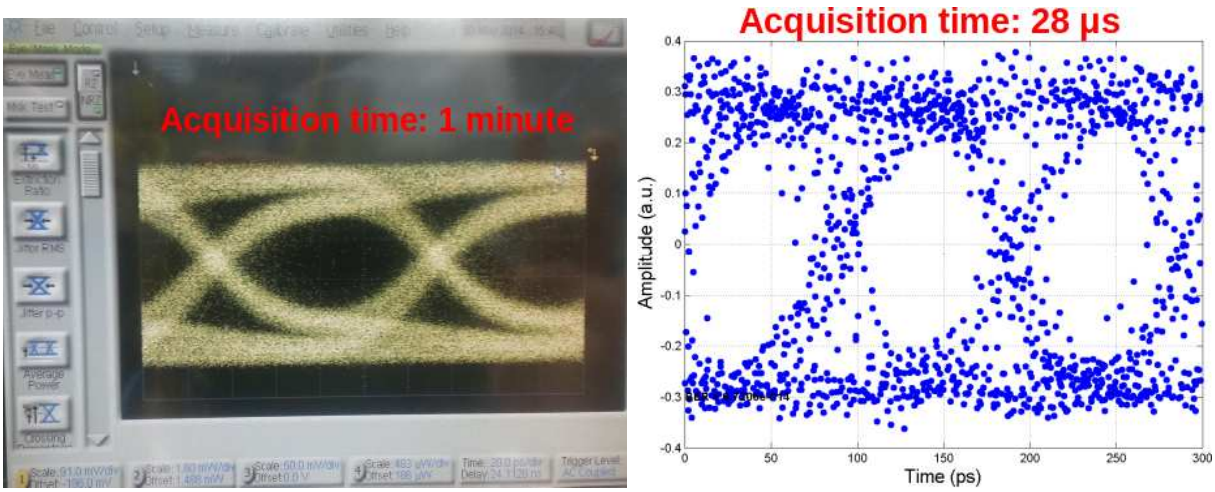

(a) Equivalent time sampling oscilloscope. (b) TiSAP.

Figure 4.14: Eye diagram of 10 Gigabit/s NRZ OOK streaming video packets between two Fujitsu Flashwave 9500 nodes. TiSAP generates the eye diagram of the 10 Gigabit/s NRZ OOK streaming video packets in an ultra-fast acquisition speed of ∼28 µs, whereas the equivalent time sampling oscilloscope takes a couple of minutes [56].

The eye diagrams captured by both the the equivalent time sampling oscilloscope and time-stretch accelerated processor are shown in Figure 4.14(a) and 4.14(b), respectively. As seen before, TiSAP generates the eye diagram of the 10 Gigabit/s NRZ OOK streaming video packets in an ultra-fast acquisition speed of ∼28 µs, whereas the equivalent time sampling oscilloscope takes a couple of minutes [56]. The experimental demonstration of real-time, in-service, optical performance monitoring on 10 Gbit/s video packets on the commercial platform exhibits the capability of real-time TiSER to be used as a feedback signal to the software-defined networking control plane to enable agility in the optical network to perform automated network restoration, disaster recovery, efficient routing, and bandwidth management, etc.

4.7 Ultra-wideband Instantaneous Frequency Measurement

Instantaneous frequency measurement (IFM) receivers have been used extensively for wideband monitoring of radar signals in naval, airborne, and ground-based electronic support measures (ESM) systems as well as for radio astronomy applications for over 60 years [182]. IFM receivers are used to measure RF frequency, amplitude, phase, pulse width and time of arrival (ToA) also known as time of flight (ToF) for radar applications, electronic warfare, and signal intelligence. A wideband IFM receiver will have high probability of frequency interception over wide instantaneous RF bandwidths and high dynamic range. Such a wideband IFM receiver should also have high sensitivity, and frequency measurement accuracy to be useful for most applications. A time-stretch based high-speed, ultra-wideband IFM technique is presented here. This section is adapted from [76, 121, 171], for which I jointly performed the experimental setups and data collection with Daniel Lam and Brandon Buckley.

4.7.1 Introduction to IFM Techniques

A typical IFM receiver consists of power divider, RF couplers and delay lines to perform electrical delay line interferometry to measure the rate of change of phase of the signal which is the instantaneous frequency of the signal of interest [183]. However, such an interferometer has limited RF bandwidth and can only intercept one frequency at a time. It would require many such interferometers operated concurrently to enable multiple frequency measurements. There are also IFM receivers which use multiple frequency discriminators operated in parallel [184] to enable amplitude and frequency measurements. Such receivers measure the largest RF signal in the band and must be above other signals by several dB in power. Also if there are multiple signals present in this receiver, two signals cannot be too close in frequency as it would result in amplitude and frequency estimation errors [185]. But such IFM receivers are also limited in bandwidth due to frequency limits of the components used and have increased hardware complexity.

Digital IFM (DIFM) receivers can perform wideband instantaneous frequency measure-

ments for multiple frequencies, measure complicated signals, and do not rely on delay lines. Instead, DIFM systems use a digital filter bank with multiple channels having detectors at the output of each channel to convert the signal into a video signal and a digital encoder converts the video signal into signal parameters such as frequency, pulse width, and amplitude. [186]. The availability of high bandwidth digitizers have increased the popularity of DIFM receivers in the recent years. However, the DIFM receiver performance is limited by the sampling rate and resolution of the ADC, which reduces as the input signal frequency increases.

A number of photonics based IFM techniques have been proposed in the recent years. One such technique employs frequency-to-intensity mapping to generate a signal detected by a low bandwidth photo-diode, the amplitude of which corresponds to the RF frequency of the input signal [187,188]. But this technique suffers from limited bandwidth of up to 10 GHz due to losses in RF delay line used. Some of the other photonic IFM techniques proposed includes employing polarization-domain interferometry [189], frequency-to-time mapping [190], multi-channel spectral multiplexing [191], and four-wave mixing (FWM) in a highly non-linear fiber (HNLF) [192]. Although these techniques can perform frequency measurements, they are incapable of measuring both frequency and amplitude.

The spectrally cluttered environments of today demand an IFM system that can perform ultra-fast measurements across wider bandwidths and also detect the frequencies of interest efficiently. The time-stretch instantaneous frequency measurement (TS-IFM) receiver presented here overcomes these challenges to provide an ultra-fast solution for performing RF frequency and power measurements across a wide bandwidth of input signals.

4.7.2 Time-Stretch Instantaneous Frequency Measurement Receiver

We implement an ultra-fast, wideband time-stretch instantaneous frequency measurement (TS-IFM) receiver using TiSER described in Section 2.3. Photonic time-stretch compresses the signal analog bandwidth which allows for ultra-fast single-shot measurement across a very high bandwidth using a slow, high resolution ADC. We apply Fast Fourier Transform (FFT)

on the digitized segment of time-domain data captured by TS-IFM to analyze the signal in the spectral domain which allows us to perform multiple frequency and amplitude measurements over an ultra-wide bandwidth. We demonstrate TS-IFM frequency measurement capabilities by performing frequency measurements across a wide bandwidth and simultaneous multiple frequency measurements without requiring additional hardware or cascading filter designs. The TS-IFM combines time-stretch enhanced recorder and digital signal processing that performs windowing on time-domain sampled data and frequency interpolation on the signal peaks. The combination of the two creates a high-resolution, wideband, and low power instantaneous frequency measurement receiver [76, 121, 171].

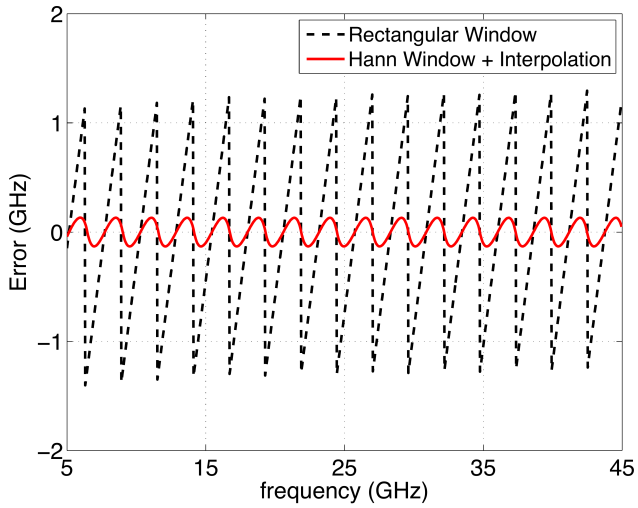

Figure 4.15: TS-IFM frequency estimation simulation, which shows using windowing with quadratic interpolation, reduces the frequency error from ±1.6 GHz to ±125 MHz. Courtesy of [121].

From each time-stretched pulse, we are able to digitize a short real-time segment of the signal due to real-time burst sampling, which allows us to perform analysis in the spectral domain. When performing an FFT of this short time segment of sampled data, the time aperture of TiSER limits the narrowest frequency resolution to resolve two signals, and the number of digitized sample points limits the spectrum frequency resolution prior to computing the FFT. However, the capture time window can be adjusted which allows for frequency resolution tuning. Windowing the sampled signal data and performing quadratic

interpolation on the signal peaks in the frequency-domain further improves the accuracy of frequency estimates [193–197]. This powerful technique is extended to improve the frequency and amplitude estimation from time-stretch measurements.

The time-stretch IFM system was simulated assuming experimental system parameters for single frequency estimation from 5 to 45 GHz [121]. To show the effectiveness of the windowing and quadratic interpolation technique, the signal frequency was estimated with and without this technique. The frequency error was calculated using a rectangular window function and a Hann window function with quadratic interpolation. As seen in Figure 4.15, with Hann windowing and interpolation, the frequency estimation error significantly reduced from ±1.6 GHz to ±125 MHz [76, 121].

To evaluate our system performance, we built TiSER using a chirped super-continuum source with $\Delta\lambda = 18$ nm, a first dispersive fiber with dispersion of -20 ps/nm, a 40 Gigabit/s EO modulator, a second dispersive fiber with dispersion of -984 ps/nm, and a 10 GHz photo-diode. A 3 Giga-samples/s ADC is used to digitize the signal. Using these dispersion parameters, we get a stretch factor of 50, giving an effective sampling rate of 150 Giga-samples/s. For tuning the frequency resolution by changing the time aperture, the first dispersive fiber was changed to -40 ps/nm and -100 ps/nm for stretch factors of 25 and 10, respectively. The EO modulator loses 6 dB over 30 GHz and limits the power sensitivity. Since each laser pulse captures a short window of the signal in time, we effectively are sweeping over a wideband spectrum. The laser pulse repetition rate of 36.6 MHz gives us a sweep time of 27 ns and the real-time burst sampling modality of TiSER would allow for detection of transient signals that could be missed by conventional IFMs.

4.7.3 Results

We performed a single frequency tone estimation experiment from 5 to 45 GHz. The signal was then digitized, a windowing function was applied to the digitized samples of the time-stretch signal, and quadratic interpolation was performed on the peaks in the frequency domain. Figure 4.16(a) shows that we are able to closely estimate the input frequency using

the TS-IFM, and Figure 4.16(b) shows the frequency estimation error.

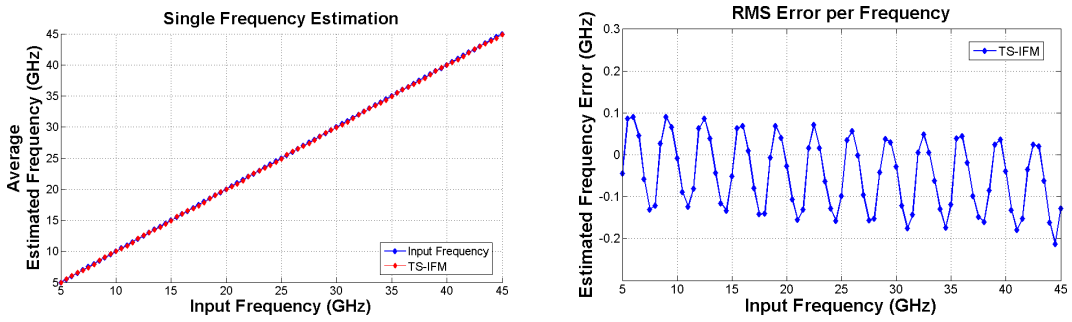

(a) (b)

Figure 4.16: The experimental results for the single tone input measurements: (a) frequency estimation for a single tone input was swept from 5 GHz to 45 GHz; (b) the estimated frequency error of 97 MHz rms is achieved using the TS-IFM receiver. Courtesy of [76, 121, 171].

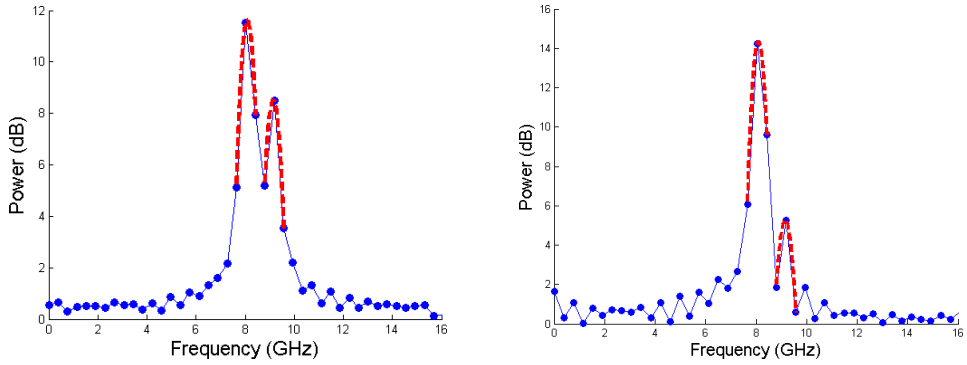

(a) (b)

Figure 4.17: Results for the double tone frequency measurements: (a) TS-IFM receiver can resolve two tones close together and with similar amplitudes simultaneously which is a challenge for current IFM receivers; (b) dual tones input at 8 GHz and 9 GHz with high and low amplitudes. Courtesy of [76, 121, 171].

Across 45 GHz, we achieve an average root-mean-square (rms) error of 97 MHz. For multiple frequency estimation, we demonstrate the capability of the TS-IFM to measure multiple tones simultaneously, given that the frequency spacing of the two tones is greater

than the FFT frequency resolution. We performed a two tone test using the TS-IFM for 10 GHz and 30 GHz with similar input RF powers, and the TS-IFM receiver estimated the tones simultaneously at 9.96 GHz and 30.01 GHz. Figure 4.17(a) shows how quadratic interpolation is applied to the peak for improved frequency estimation. We also demonstrate the flexibility of the system in tuning the bandwidth and frequency resolution by modifying the dispersion for the first dispersive fiber to provide a narrower frequency resolution.

Table 4.1: Tuning TS-IFM for bandwidth and resolution [76, 171]

$\Delta\lambda$ **(GHz)**	**DCF1 (ps/nm)**	**Time Aperture (ns)**	**Stretch Factor**	**Nyquist Frequency (GHz)**
3.31	-20	0.3	50	75
1.69	-40	0.6	25	37.5
0.72	-100	1.5	10	15

Table 4.1 shows the tested scenarios where altering the first dispersive fiber changes the time aperture and thus the frequency resolution. By changing the frequency resolution, the TS-IFM receiver can better resolve two tones closer together. As demonstrated in Figure 4.17(b), two frequencies at 8 GHz and 9 GHz were inputted to TS-IFM. The first dispersive fiber was modified to obtain a stretch factor of 10, thus increasing the time aperture. The frequencies were estimated to be at 8.09 GHz and 9.15 GHz.

The time-stretch IFM receiver has several key advantages compared to commercial systems. TS-IFM has the ability to perform frequency measurements across an ultra-wide instantaneous bandwidth with increased accuracy through windowing and quadratic interpolation. The fast sweep time allows for rapid spectral measurements across enormous bandwidths. Additionally, it is possible to estimate multiple frequencies simultaneously without any additional filtering or cascading stages, whereas current commercial systems do not have this capability. This makes the TS-IFM receiver very effective in spectrally cluttered environments and for quickly detecting transient signals. Moreover, the effective sampling throughput of TS-IFM is significantly higher, allowing it to capture signals with high tem-

poral resolution due to its real-time burst sampling and uses less power than high speed real-time ADCs with similar throughput, thus reducing the electronic hardware complexity and cost. The back-end digital signal processing of the TS-IFM can be implemented in real-time using field programmable gate arrays. It could also be used as a wideband cueing receiver for finer resolution systems. Further work in calibrating the system for amplitude measurements and also implementing continuous time-stretch digitization architecture for longer collection times will result in better frequency resolution [76, 171].

4.8 Future Work - Production-Level Device Testing

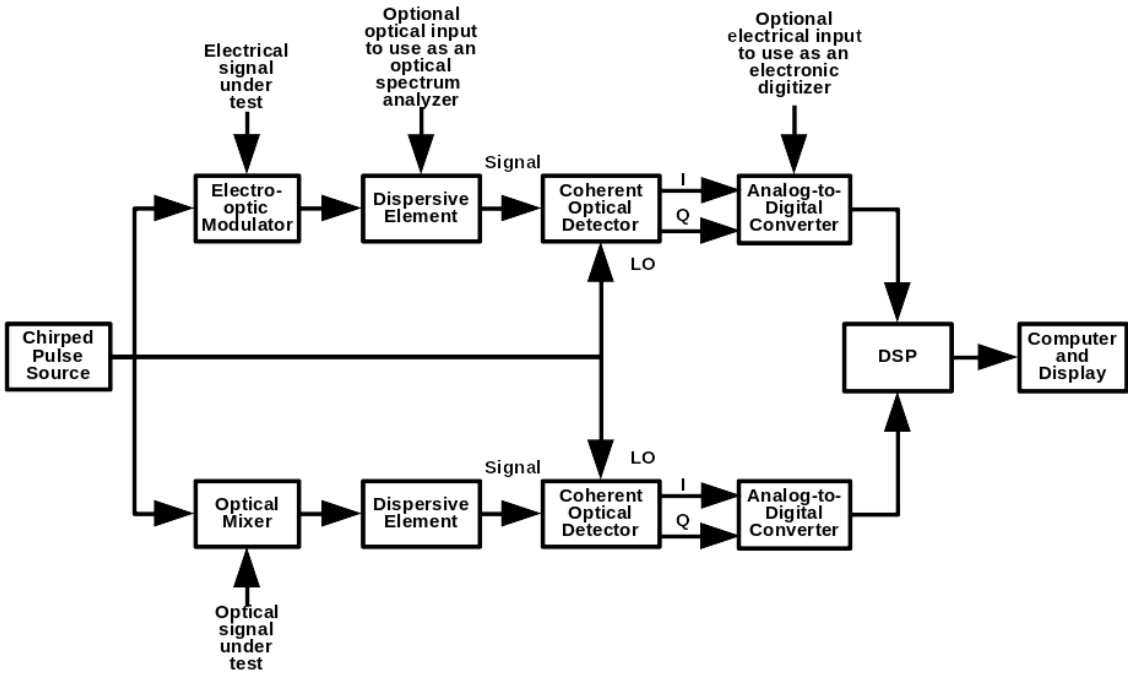

Figure 4.18: Proposed implementation of the hybrid coherent time-stretch oscilloscope with ability to capture and analyze both optical and electrical inputs simultaneously. Courtesy of [198].

Time-stretch enhanced recording oscilloscope has overcome the limitations of electronic ADCs, BERTs and sampling oscilloscopes for high-speed signal characterization. However, TiSER is limited in bandwidth due to electrical-to-optical (E/O) and optical-to-electrical

(O/E) conversions. The proposed system addresses these limitations and overcomes the deficiencies of previously developed methods and also enables analysis of advanced signal modulation formats such as coherent and pulse amplitude modulation schemes. The proposed system combines TiSAP [56] and all-optical photonic time-stretch digitizer [143] with coherent receivers to implement a hybrid time-stretch system that can enable ultra-fast production-level testing.

A block diagram of the proposed hybrid coherent time-stretch oscilloscope for measuring/testing both optical and electrical input signals simultaneously for a full-loop characterization of transmitters and receivers, can be seen in Figure 4.18. The hybrid coherent time-stretch oscilloscope modulates the signal under test onto a chirped mode-locked laser pulse using either an optical mixer based on four-wave mixing process for optical signals or an electro-optic modulator for electrical signals. The modulated signal undergoes time-stretch to compress the signal bandwidth and the stretched modulated signal is input to a coherent optical detector to recover the in-phase (I) and quadrature (Q) signals for the coherent optical signals. The electrical signals from the coherent detectors are digitized by slow, high resolution analog-to-digital converters. The digitized data is processed using an FPGA in real-time. A computer is used to visualize the signals under test using eye-diagrams or constellation diagrams and perform analysis to estimate the performance characteristics of the signal under test. [198].

The proposed system can analyze high-speed optical signals enabling fast characterization of optical/opto-electronic/electro-optic devices and also modulation format agnostic, in-service analysis of optical data in a communication system. A time-stretch accelerated processor for signal analysis is designed such that it can accommodate both optical data as well as electrical data (hybrid) with coherent (complex field) signal formats. Signal processing methods are used for recovering the phase of the signal and removal of distortion in a signal that was digitized using time-stretch enhanced recording oscilloscope. The coherent time-stretch accelerated processor described herein also offer a unique method to measure eye diagrams for serial data and to measure bit error rates in far less time than is required by existing technologies enabling faster testing of optical and opto-electronic devices.

4.9 Conclusion

We integrated TiSAP into the Testbed for Optical Aggregation Networks at the College of Optical Sciences, University of Arizona, Tucson. TiSAP was used to demonstrate in-service optical performance monitoring of 10 Gigabit/s NRZ OOK signal in a metro-scale network with real-time feedback of BER to the SDN control plane to switch wavelengths and routes to implement an agile network that recovers from disasters. We also characterized the BER of the network using TiSAP in the presence on non-linear effects namely, amplified spontaneous emission and self phase modulation and calibrated the measurements with a BERT. We also demonstrated for the first time, burst-mode real-time, in-service, optical performance monitoring using eye diagrams on a 10 Gbit/s NRZ OOK streaming video packets on a commercial optical network platform, consisting of two Fujitsu Flashwave 9500 nodes. The burst-mode real-time TiSAP implementation has an effective sampling rate of 125 GSamples/s, and a very fast acquisition time of $\sim$28 microseconds. We also report an ultra-fast time-stretch instantaneous frequency measurement receiver based on TiSAP which allows for both amplitude and frequency measurements for a wide bandwidth of 5-45 GHz. We also proposed a new instrumentation system based on a hybrid coherent TiSAP for analyzing high-speed optical and electrical signals enabling ultra-fast production-level characterization of optical/opto-electronic/electro-optic devices and for in-service analysis of optical and electrical data in a communication system.

CHAPTER 5

Single-shot Network Analyzer for Extremely Fast Measurements

A new instrument for fast measurement of frequency response of high bandwidth optical and electronic devices is reported. Single shot frequency spectrum measurements are enabled by the time-stretch technology. An extremely fast measurement time of 27 ns is reported for the instrument. The reported instrument enables single-shot impulse response measurements with 40 GHz bandwidth, which could be extended to beyond 100 GHz by using a faster electro-optic modulator. An ultra-low intra-pulse jitter of 5.4 fs is reported for the proposed instrument. The impulse responses measured using this technique are shown to correspond consistently with the manufacturer's specifications for the device under test. The reported instrument makes possible high-speed network parameter measurements thereby enabling high-speed production-level testing of high bandwidth opto-electronic devices/circuits/subsystems/systems and complex permittivity measurement of dielectric materials at a much reduced test time lowering the test costs in a production environment. A new instrument for extremely fast measurement of Terahertz signals is proposed.

5.1 Introduction

Many frequency response measurement techniques have been proposed for high-speed electro-optic modulators [199–203] and photo-diodes [204–209]. Equivalent-time sampling oscilloscopes have very high bandwidth capabilities, but requires a long time for accurate measurements. All these techniques are time consuming and would increase the production test time for the device under test. Also, it becomes difficult, for example due to increased parasitic

effects at higher frequencies, to accurately measure the frequency response of photo-diodes and electro-optic modulators using conventional swept-frequency techniques [99].

Time-domain based techniques have reported faster measurement times. A time-domain measurement technique for high bandwidth device characterization using optical-microwave phase locking using a mode-locked laser (MLL) and photo-conductive mixers and samplers [210] reports a measurement time of 40 µs. Small signal power measuring techniques to measure the frequency responses of $LiNbO_3$ modulators [211] and electro-absorption modulators [212] have also been proposed. The small signal power measurement technique also takes long measurement time of up to 10–15 seconds for taking one frequency measurement [212].

Real-time oscilloscopes have also been used to perform fast network analysis [213], which could enable faster frequency response measurements. Even though the real-time oscilloscopes commercially available today can have very high analog bandwidths of over 80 GHz, the effective number of bits reduce significantly as frequencies increase [90, 91, 94]. Clock jitter in the sampling clock of ADC also contributes to its reducing resolution. The best clock jitter achieved in state-of-the-art ADCs are of the order of 110-fs [130]. Since real-time oscilloscopes are the fastest technique available, the proposed system would be compared against a real-time oscilloscope.

We report a single-shot network analyzer (SiNA) which uses time-stretch technology to compress the signal bandwidth [111–114, 125], employing a slower ADC to digitize the time-stretched signal, and utilizing a field programmable gate array (FPGA) to perform the necessary digital signal processing (DSP) in real-time. The proposed system has an extremely high-speed, single-shot measurement time of 27 ns with a very low jitter of 5.4 fs.

5.2 Single-shot Network Analyzer (SiNA)

The SiNA, as shown in Figure 5.1, consists of the time-stretch enhanced recording oscilloscope with a high-bandwidth ADC and a reconfigurable FPGA to perform real-time digital signal processing on the digitized data [85, 86]. The ultra-short mode-locked laser pulse (width < 1 ps), prior to undergoing pre-chirping, is used as test stimulus for impulse response

analysis of the (DUT). The response signal from the DUT is captured by an electro-optic modulator (EOM) in a single-shot by modulating it onto the chirped laser pulse.

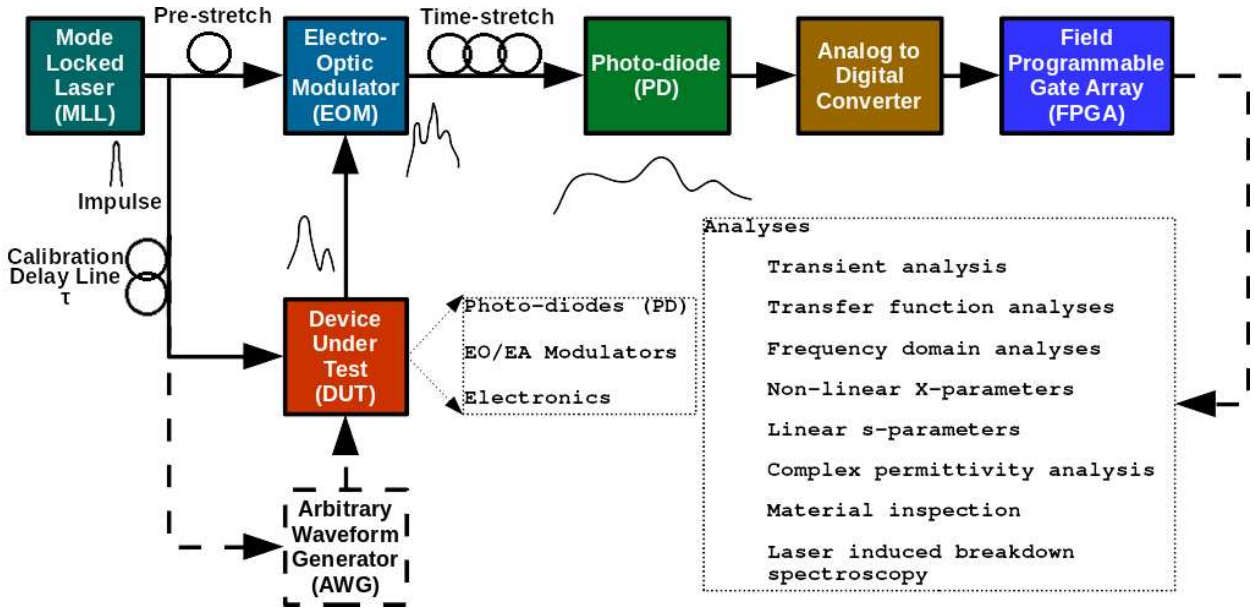

Figure 5.1: Block diagram of the Single-shot Network Analyzer (SiNA) [86].

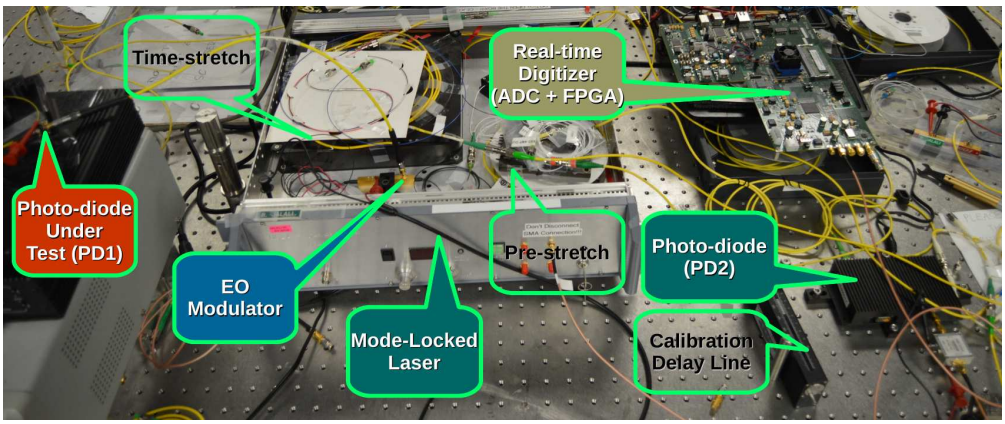

Figure 5.2: A photograph of the experimental setup for photo-diode testing.

A calibration delay line with a delay of τ, is used to adjust the delay of the impulse signal to synchronize the transient response of the DUT with its intensity modulation of chirped laser pulse. Alternatively, the SYNC output of the MLL can be used to trigger an arbitrary waveform generator (AWG) to generate the desired type of test stimuli, based on the optimum bandwidth considerations, for the device under test, for example, a sharp

rising edge to perform step response analysis or providing the highest resolution for a given bandwidth. A photograph of the experimental setup can be seen in Figure 5.2.

The time stretched response signal of the device under test is converted to an electrical signal by a photo-detector which is first digitized by a fast ADC and then processed in real-time using the massively parallel hardware implemented on the FPGA or by a computational software running on a computer. The output of the DUT is captured in real-time bursts by digitization of the corresponding time stretched modulated laser pulse. The pulse repetition rate of the MLL laser is 36.9 MHz and so the single-shot measurement acquisition time is ~27 ns.

5.3 Photo-diode Test

5.3.1 Low Bandwidth Photo-diode

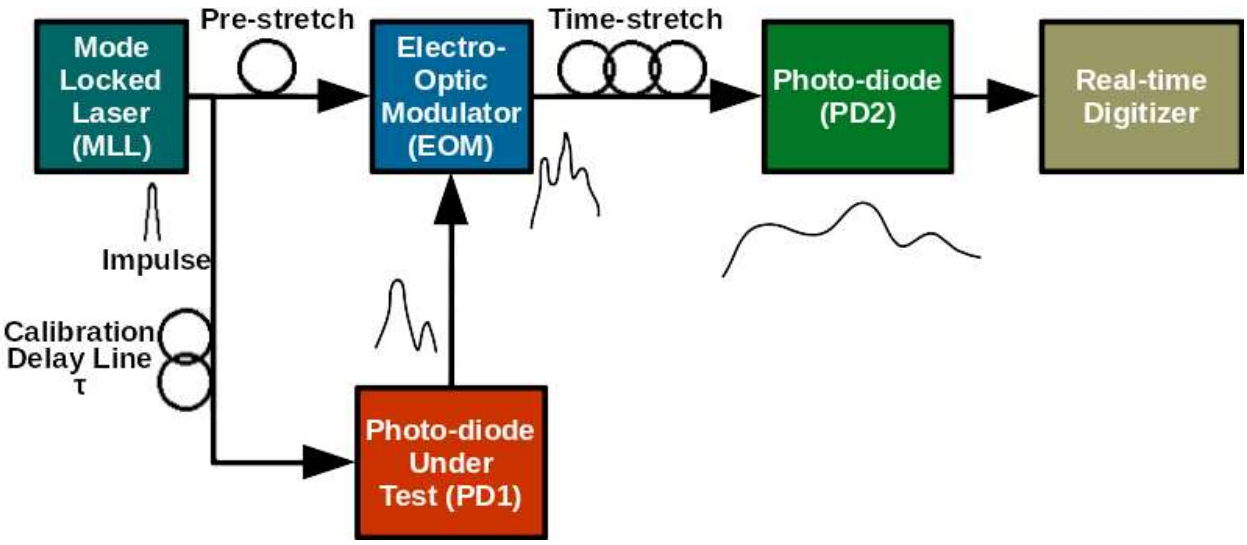

Figure 5.3: The test setup for measuring the impulse response of photo-detector [86].

The test setup for measuring the impulse response of photo-diodes is shown in Figure 5.3. The impulse response produced by the photo-diode under test is modulated onto the pre-chirped laser pulse using a 40 GHz EOM before time-stretching it by a stretch-factor of ~8.57 (using equation 2.4 for $D_1 = -130$ ps/nm and $D_2 = -984$ ps/nm) and subsequently digitizing

it using a 50 Giga-samples/s (GSps) real-time oscilloscope at 16 GHz analog bandwidth.

The synchronized time domain representation of the time-stretched un-modulated pre-chirped laser pulse envelope, e(n), and the impulse response of the photo-diode under test modulated onto the pre-chirped laser pulse after time-stretching, m(n) are shown in Figure 5.4. The time-domain impulse response of the photo-diode under test, h(n) is given by,

$$h(n) = \frac{m(n)}{e(n)} \tag{5.1}$$

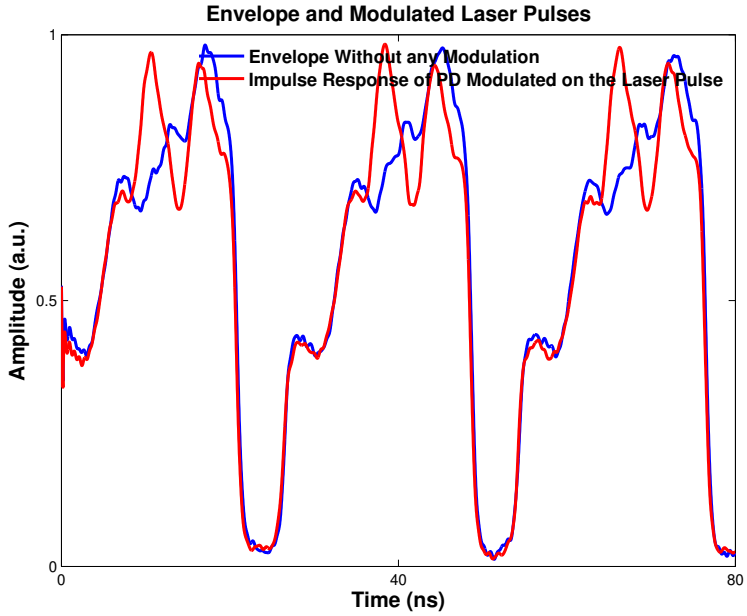

Figure 5.4: The laser envelope without any modulation and the laser pulse modulated by the impulse response of the photo-detector.

The time-domain impulse response of the photo-diode under test obtained from a single measurement by SiNA and also from a 50 GSps real-time oscilloscope without a time-stretch front-end is plotted in Figure 5.5. The temporal resolution of SiNA is 8.57 times better than the 50 GSps digitizer due to time-stretch, using equation 2.4. The impulse response of the photo-diode under test obtained from SiNA matches with the device manufacturer's datasheet [214]. The frequency response of the photo-diode is obtained by taking Fast Fourier Transform (FFT) of the impulse response estimated from the single shot measurement, h(n).

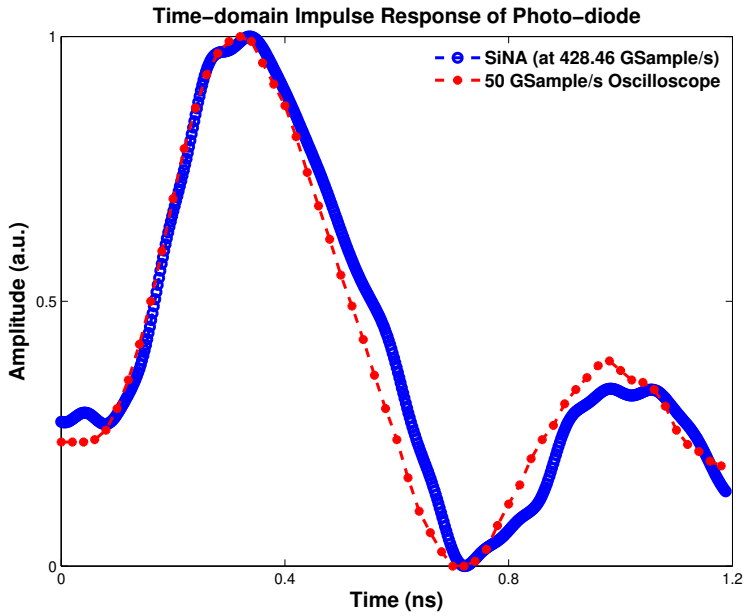

Figure 5.5: The time-domain impulse response of the photo-detector under test.

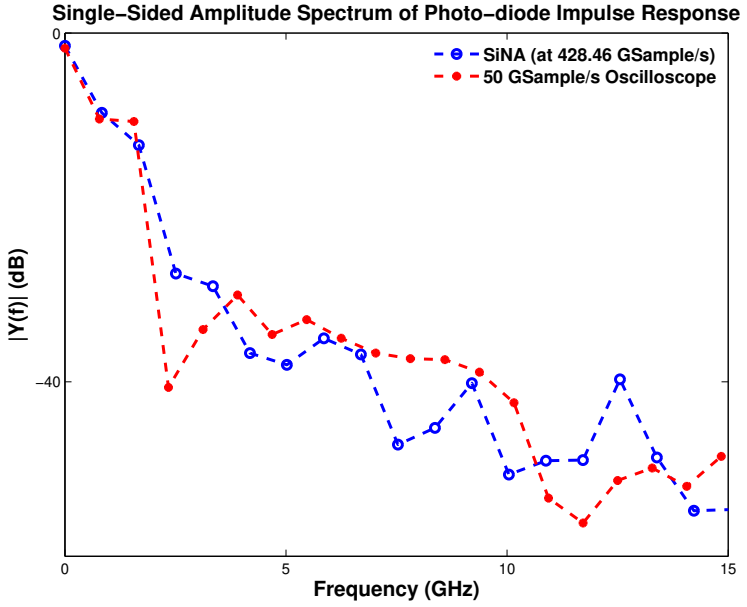

Figure 5.6: The single-sided amplitude spectrum of the impulse response of the photo-detector under test captured by SiNA and 50 GSample/s real-time oscilloscope in a single measurement.

The amplitude and phase spectrum of the photo-detector under test is shown in Figure 5.6

and Figure 5.7, respectively. Comparing the amplitude and phase spectrum from single-shot measurements of both SiNA and real-time oscilloscope, SiNA clearly has higher bandwidth and resolution due to time stretching (effective sampling rate of 428.5 GSps = 8.57×50 GSps).

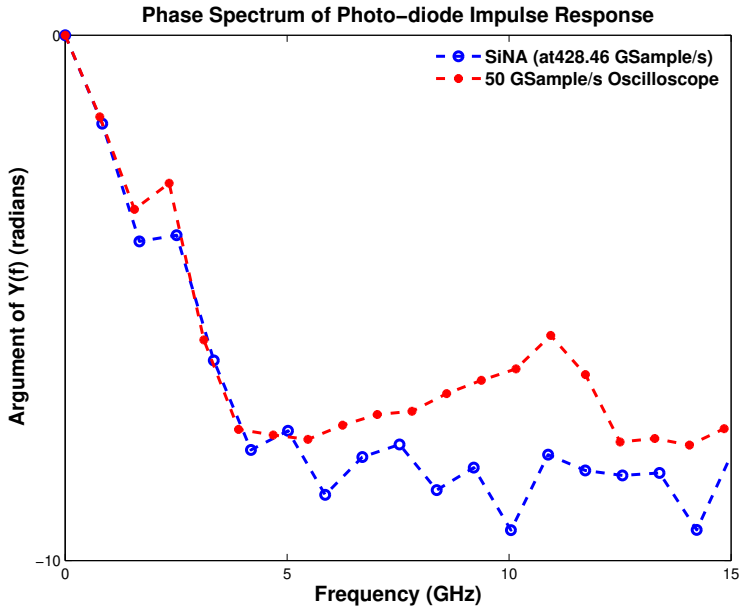

Figure 5.7: The phase spectrum of the impulse response of the photo-detector under test captured by SiNA and 50 GSample/s real-time oscilloscope in a single measurement.

At higher frequencies, the frequency response measured using the real-time oscilloscope becomes erroneous due to its lower temporal resolution and bandwidth limitation of 16 GHz.

5.3.2 High Bandwidth Photo-diode

We used the same test setup for measuring the impulse response of photo-diodes as shown in Figure 5.3 for a photo-diode with an RF bandwidth of 30 GHz. The impulse response produced by the high-bandwidth photo-diode under test is modulated onto the pre-chirped laser pulse using a 40 GHz EOM before time-stretching it by a stretch-factor of ∼50 (using equation 2.4 for D_1 = –50 ps/nm and D_2 = –984 ps/nm) and subsequently digitizing it using a 50 GSample/s (GSps) real-time oscilloscope at 16 GHz analog bandwidth.

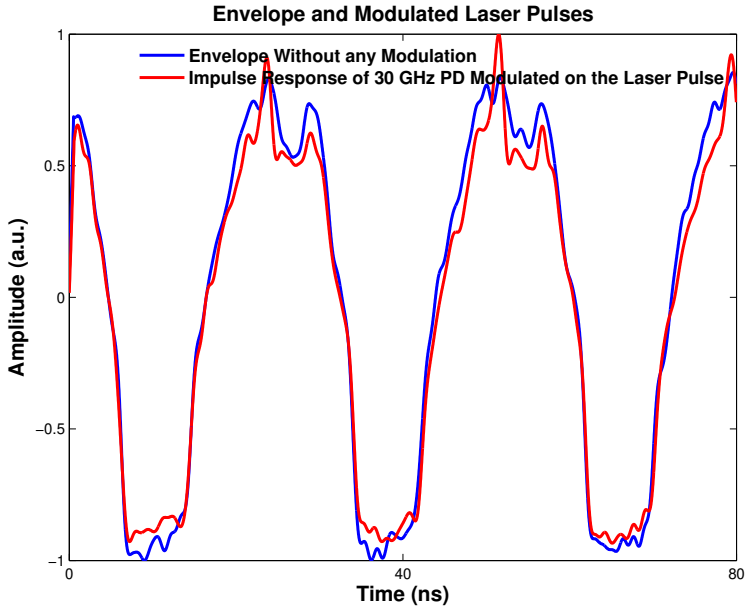

Figure 5.8: The laser envelope without any modulation and the laser pulse modulated by the impulse response of the photo-detector.

The synchronized time domain representation of the time-stretched un-modulated pre-chirped laser pulse envelope, e(n), and the impulse response of the high bandwidth photo-diode under test modulated onto the pre-chirped laser pulse after time-stretching, m(n) are shown in Figure 5.8. The time-domain impulse response of the photo-diode under test, h(n) is given by equation 5.1.

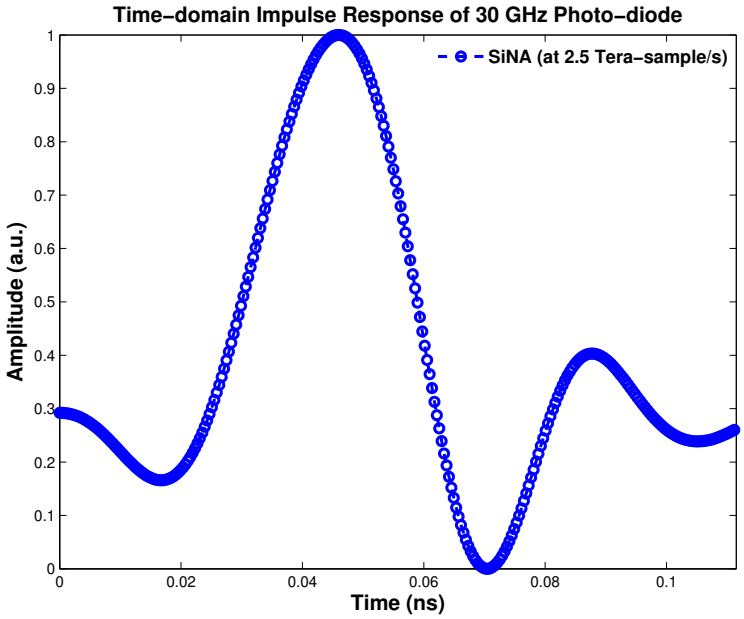

Figure 5.9: The time-domain impulse response of the photo-detector under test.

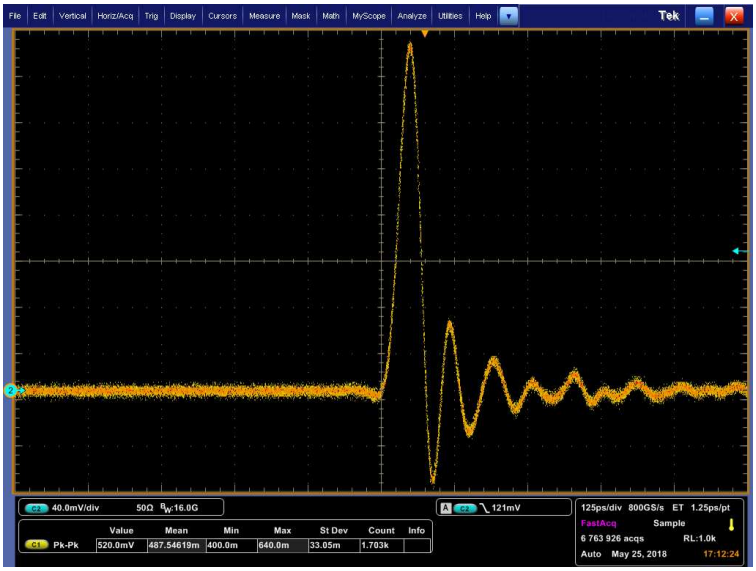

Figure 5.10: The time-domain impulse response of the 30 GHz photo-detector under test captured using a sampling scope.

The time-domain impulse response of the 30 GHz photo-diode under test obtained from a single measurement by SiNA is plotted in Figure 5.9. A real-time oscilloscope measurement for this device for comparison with SiNA was not performed due to the 16 GHz analog

bandwidth limitation of the oscilloscope. However the time-domain trace of the photo-diode impulse was measured using a sampling scope and is plotted in 5.10 for comparison with the measurement by SiNA.

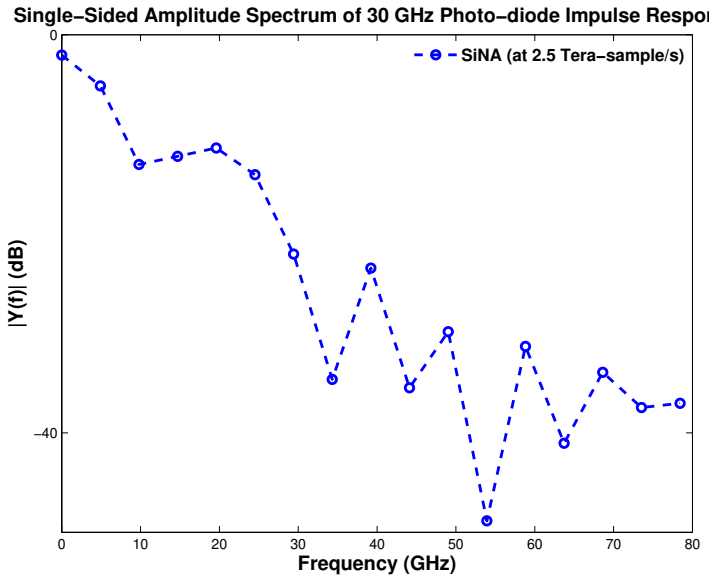

Figure 5.11: The single-sided amplitude spectrum of the impulse response of the photo-detector under test captured by SiNA and 50 GSample/s real-time oscilloscope in a single measurement.

The temporal resolution of the measurements taken using SiNA is extremely high due to the effective real-time burst sampling rate of 50×50 GSps = 2.5 Tera-samples/s (TSps). The frequency response of the photo-diode is obtained by taking Fast Fourier Transform (FFT) of the impulse response estimated from the single shot measurement, h(n).

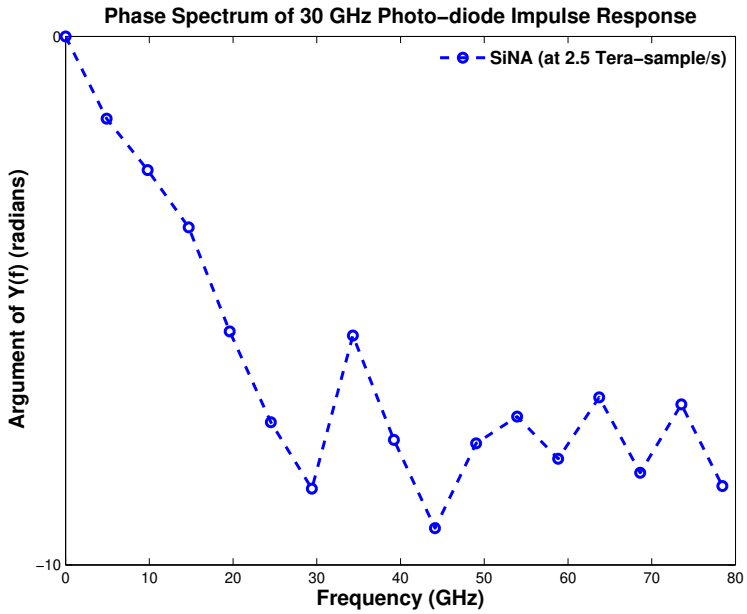

Figure 5.12: The phase spectrum of the impulse response of the photo-detector under test captured by SiNA and 50 GSample/s real-time oscilloscope in a single measurement.

The amplitude and phase spectrum of the photo-detector under test is shown in Figure 5.11 and Figure 5.12, respectively. Comparing the amplitude and phase spectrum from single-shot measurements of both SiNA and real-time oscilloscope, SiNA clearly has higher bandwidth and resolution due to time stretching (effective sampling rate of 2.5 Tera-samples/s = 50×50 GSps).

5.4 Electro-optic Modulator Test Setup

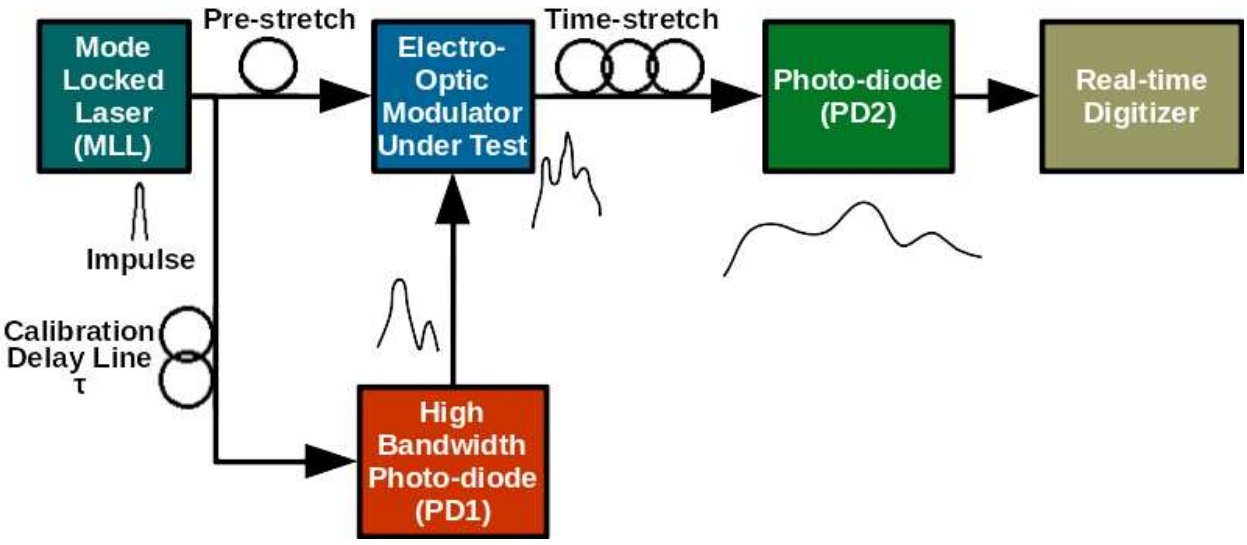

Figure 5.13: The test setup for measuring the impulse response of electro-optic modulator, EOM.

The test setup for characterizing the frequency response of an electro-optic modulator, is shown in Figure 5.13. The SYNC output from the mode locked laser of SiNA is converted to an electrical signal using a high bandwidth photo-diode, PD1. The electrical output signal of PD1 is the test pulse signal applied to the RF input port of the modulator. The electro-optic modulator under test, EOM, receives the optical input from a pre-chirped mode-locked laser and modulates it with the applied test impulse signal.

The impulse response of the modulator modulated on the pre-chirped laser pulse undergoes time stretching by the second dispersion compensating fiber. The time-stretched signal is then converted into an electrical signal by photo-diode PD2 and then digitized to perform the measurements of the frequency response of the EOM under test. The impulse response measurement of the EOM under test can be performed in a single-shot measurement time of 27 ns.

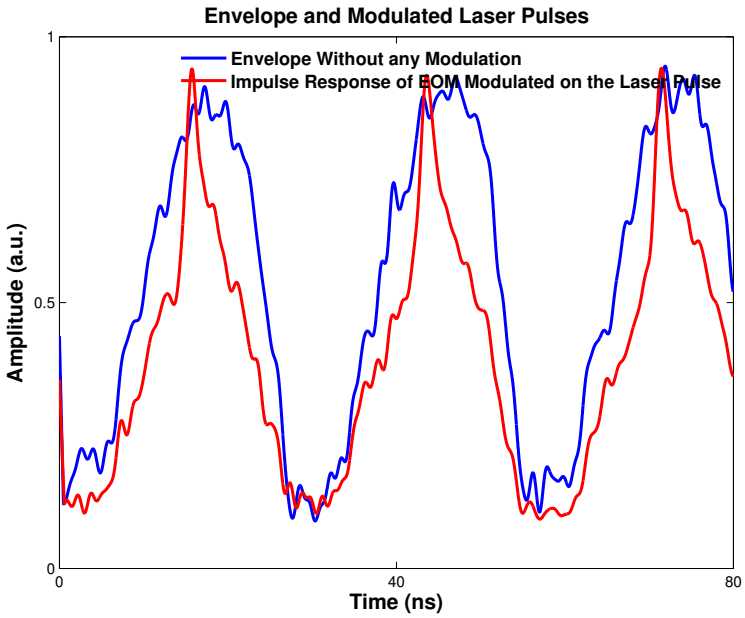

Figure 5.14: The laser envelope without any modulation and the laser pulse modulated by the impulse response of the electro-optic modulator.

The EOM under test was a 15 GHz $LiNbO_3$ modulator. The stretch-factor for this implementation of SiNA for measuring the frequency response of EOM under test was 50 as the the dispersion of the DCFs were selected such that D_1 = –20 ps/nm and D_2 = –984 ps/nm. The time-stretched un-modulated pre-chirped laser pulse envelope, and the impulse response of the EOM under test modulated onto the pre-chirped laser pulse after time-stretching, are shown in Figure 5.14.

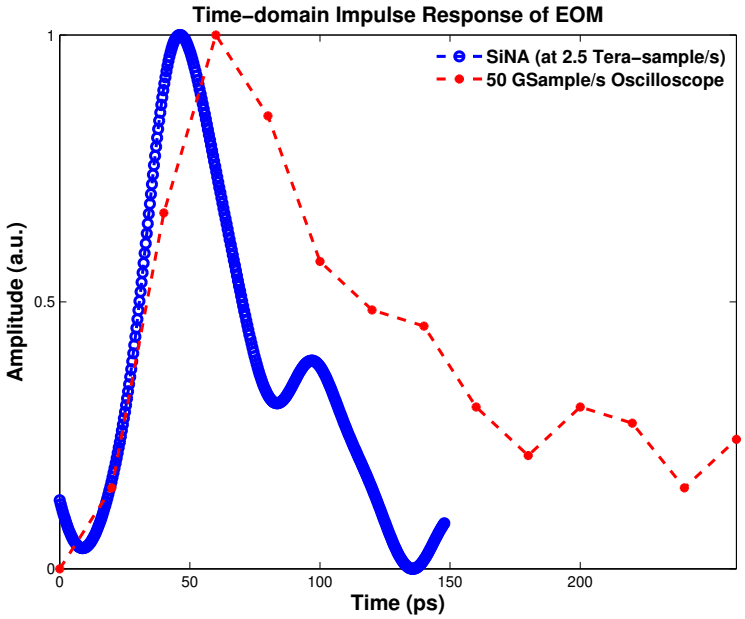

Figure 5.15: The time-domain impulse response of the electro-optic modulator under test captured at 2.5 Tera-samples/s by SiNA and 50 GSample/s real-time oscilloscope in a single measurement.

The time-domain impulse response of the EOM under test obtained from a single measurement by SiNA and also from a 50 GSps real-time oscilloscope without a time-stretch front-end is plotted in Figure 5.15. The temporal resolution of SiNA is 50 times better than the 50 GSps digitizer with a sampling rate of 2.5 Tera-samples/s, which is also evident from the faster rise-time observed in the impulse response captured by SiNA over the 50 GSps digitizer.

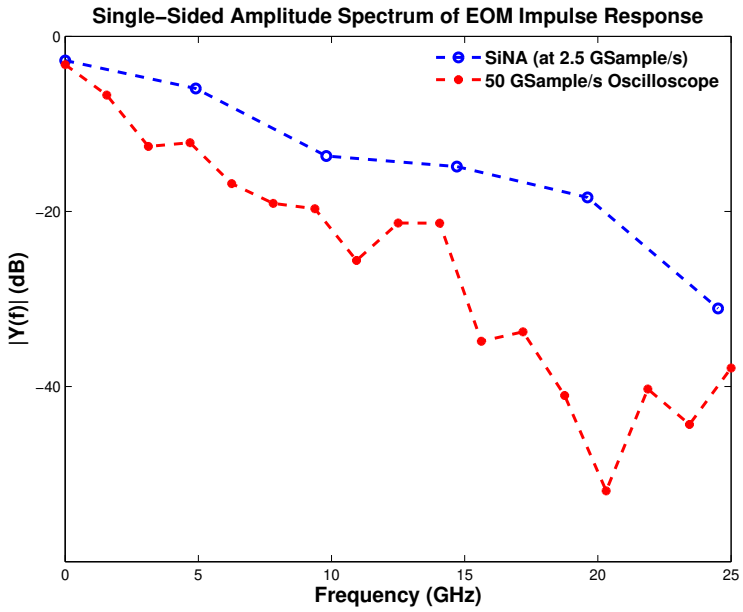

Figure 5.16: The single-sided amplitude spectrum of the impulse response of the electro-optic modulator under test captured at 2.5 Tera-samples/s by SiNA and 50 GSample/s real-time oscilloscope in a single measurement.

The amplitude and phase spectrum of the EOM under test is shown in Figure 5.16 and Figure 5.17, respectively. Comparing the amplitude and phase spectrum from single-shot measurements of both SiNA and real-time oscilloscope, SiNA clearly has higher bandwidth and resolution due to time stretching (effective sampling rate of 2.5 Tera-samples/s = 50×50 GSps). At higher frequencies, the frequency response measured using real-time oscilloscope becomes erroneous due to its lower temporal resolution and bandwidth limitation.

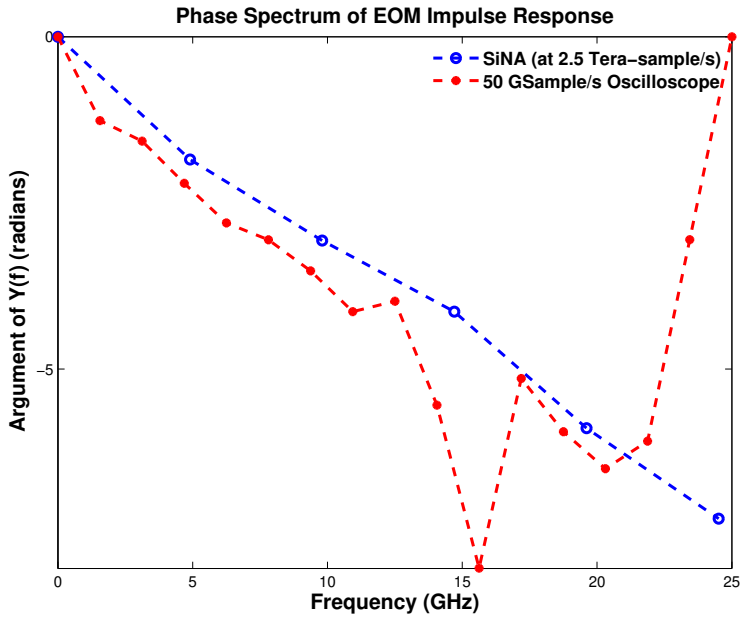

Figure 5.17: The phase spectrum of the impulse response of the electro-optic modulator under test captured at 2.5 Tera-samples/s by SiNA and 50 GSample/s real-time oscilloscope in a single measurement.

The bandwidth of photo-diode, PD1 has to be at least twice the bandwidth of the EOM under test. For the 15 GHz EOM testing, the bandwidth of the photo-diode PD1 was 30 GHz.

5.5 Broadband Electronic Amplifier Test Setup

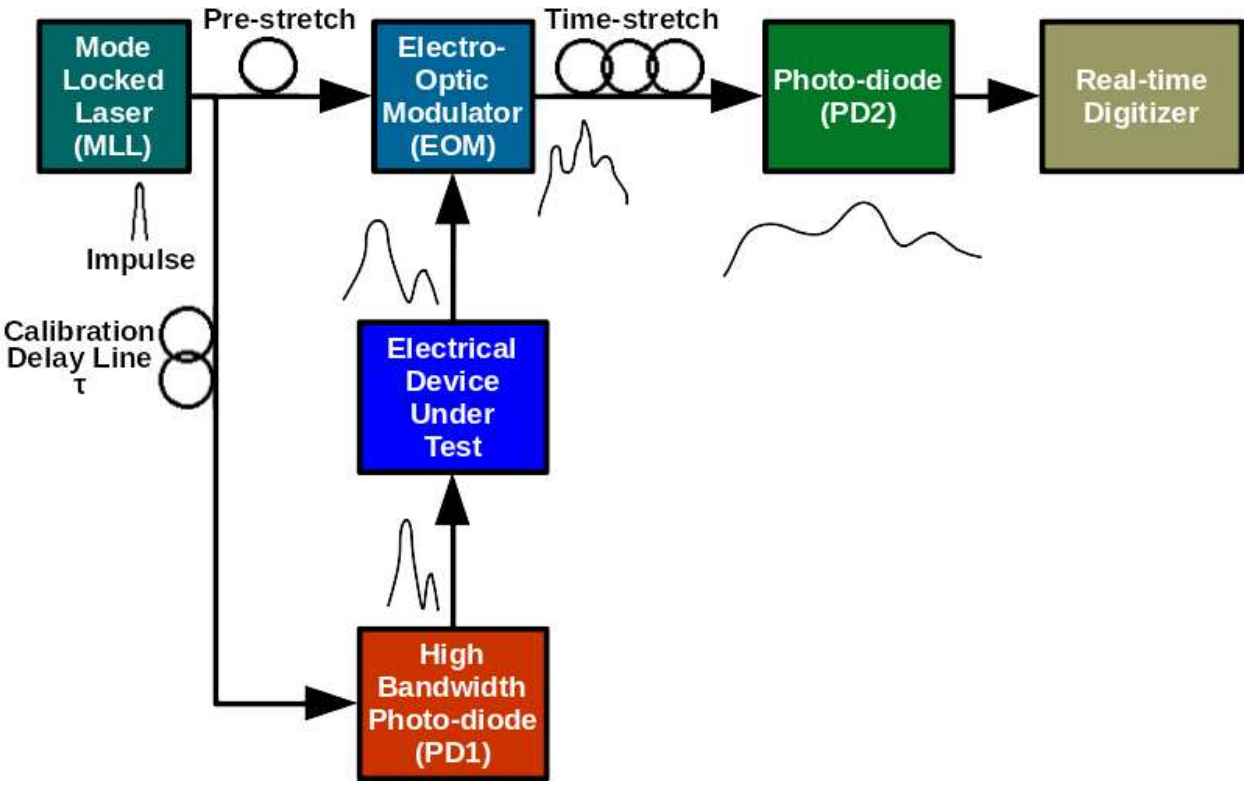

Figure 5.18: The test setup for measuring the impulse response of an electrical device under test such as an electrical broadband RF amplifier, modulator driver, etc.

The test setup for performing single-shot frequency response measurements of broadband electronic devices is shown in Figure 5.18. The ultra-short < 1 ps optical pulse signal from the mode-locked laser output is power divided and inputted to a high-speed photo-diode, PD1, through a calibrated delay line to generate an electrical impulse signal. The high bandwidth electrical impulse signal is used as the stimulus to test the wide-band electrical device under test. The impulse response of the electrical device under test is applied to the RF input port of the 40 GHz electro-optic modulator, EOM. The electro-optic modulator receives the optical input from a pre-chirped mode-locked laser and modulates it with the applied impulse response of the electrical device under test.

The impulse response of the electrical device under test modulated on the pre-chirped laser pulse undergoes time stretching by the second dispersion compensating fiber. The

time-stretched signal is then converted into an electrical signal by photo-diode, PD2, and then digitized to perform the measurements of the frequency response of the electrical device under test. The impulse response measurement of the electrical device under test can be performed in a single-shot measurement time of 27 ns.

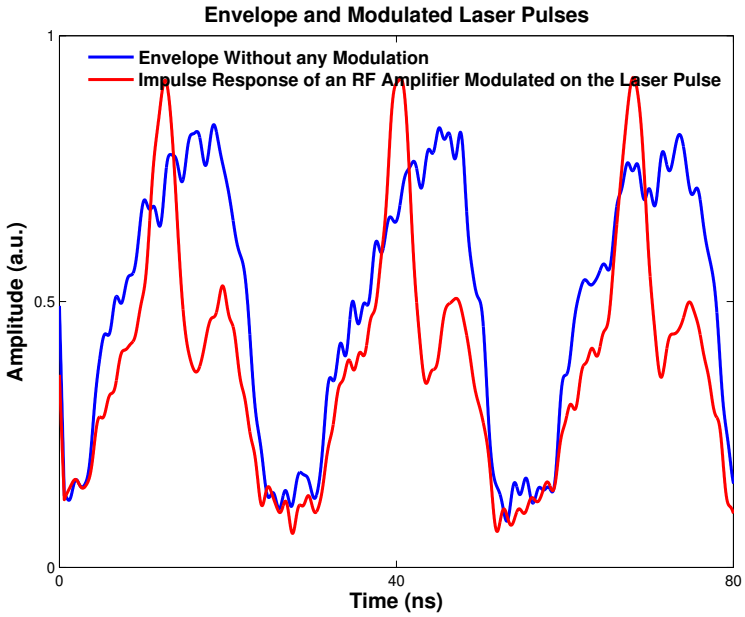

Figure 5.19: The laser envelope without any modulation and the laser pulse modulated by the impulse response of the electrical broadband RF amplifier under test.

The electrical broadband RF amplifier under test had a bandwidth of 9.5 GHz. The stretch-factor for this implementation of SiNA for measuring the frequency response of the broadband RF amplifier under test was 50 as the the dispersion of the DCFs were selected such that $D_1 = -20$ ps/nm and $D_2 = -984$ ps/nm. The time-stretched un-modulated pre-chirped laser pulse envelope, and the impulse response of the broadband RF amplifier under test modulated onto the pre-chirped laser pulse after time-stretching, are shown in Figure 5.19.

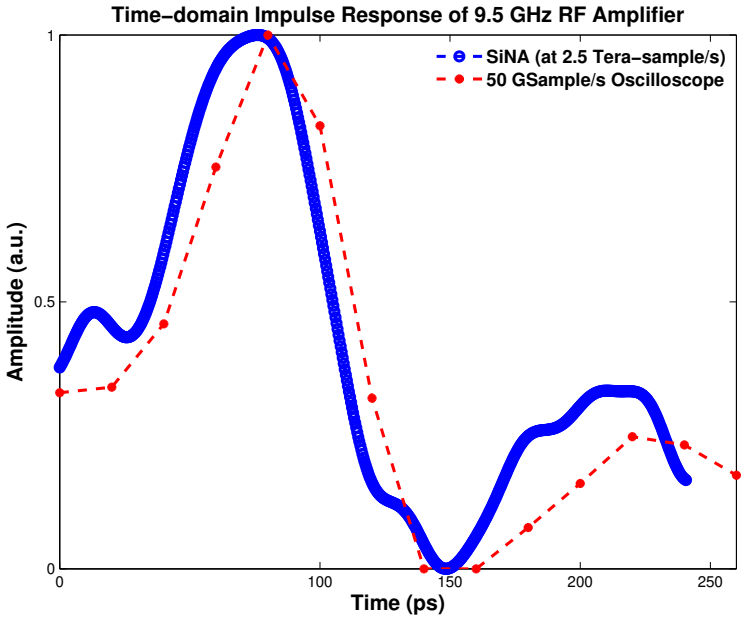

Figure 5.20: The time-domain impulse response of the electrical broadband RF amplifier under test captured at 2.5 Tera-samples/s by SiNA and 50 GSample/s real-time oscilloscope in a single measurement.

The time-domain impulse response of a 9.5 GHz electrical broadband RF amplifier under test obtained from a single measurement by SiNA and also from a 50 Giga-samples/s real-time oscilloscope is plotted in Figure 5.20. The temporal resolution of the measurements taken using SiNA is 50 times better than a 50 Giga-samples/s real-time oscilloscope due to the effective real-time burst sampling rate of 50×50 GSps = 2.5 Tera-samples/s.

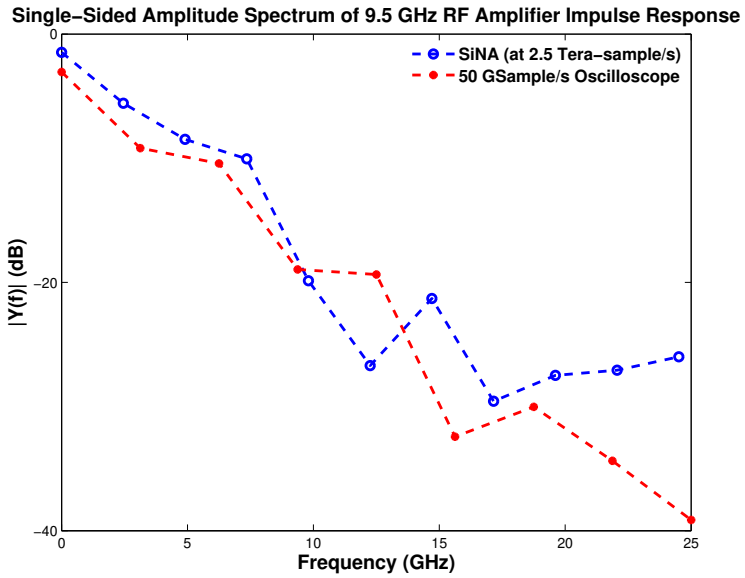

Figure 5.21: The single-sided amplitude spectrum of the impulse response of the electrical broadband RF amplifier under test captured at 2.5 Tera-samples/s by SiNA and 50 GSample/s real-time oscilloscope in a single measurement.

The amplitude and phase spectrum of the broadband RF amplifier under test is shown in Figure 5.21 and Figure 5.22, respectively.

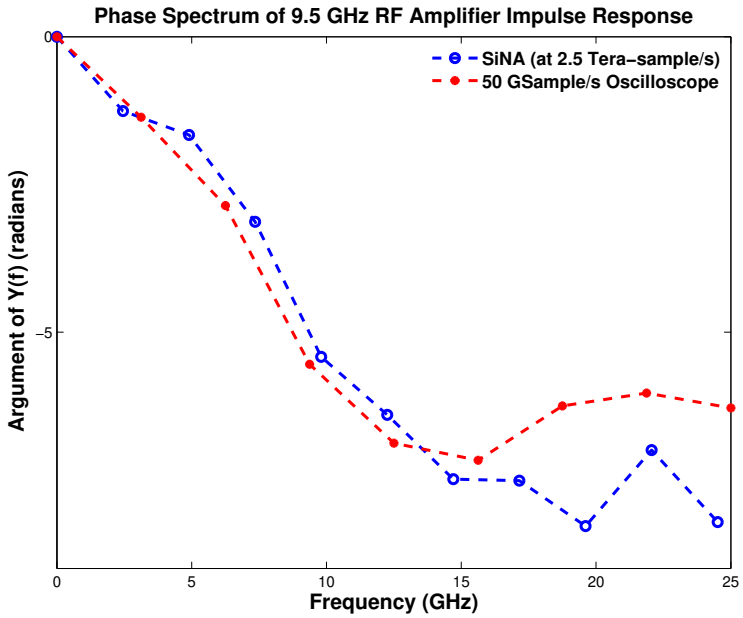

Figure 5.22: The phase spectrum of the impulse response of the electrical broadband RF amplifier under test captured at 2.5 Tera-samples/s by SiNA and 50 GSample/s real-time oscilloscope in a single measurement.

The bandwidth of photo-diode, PD1, and the electro-optic modulator, EOM, has to be at least twice the bandwidth of the electronic device under test. For the 9.5 GHz electrical broadband RF amplifier testing, the RF bandwidth of the Mach-Zehnder modulator, EOM, was 40 GHz. The photo-diode used had an RF bandwidth of 30 GHz, and its impulse and frequency response characteristics were measured using SiNA and can be found in section 5.3.2.

5.6 Discussion

SiNA is extremely power efficient, consuming only 50 W when used with a 3 GSps digitizer and an FPGA to perform digitization and measurement analyses as compared to over 670 W for a commercial bench-top VNA. SiNA is also very compact compared to a commercial bench-top VNA.

Table 5.1: Comparison of specifications of SiNA with a network analyzer

Specification	**Network Analyzer**	**SiNA**
Measurement time	µs to ms. Multiple sweeps required and is very slow for applications such as s-parameter measurements (can even take hours).	27 ns - single-shot
Equivalent sampling rate	Signal is down-converted and digitized or a sampling oscilloscope is used.	2.5 Tera-samples/s burst sampling throughput using time-stretch.
Operational bandwidth	300 kHz to 110 GHz for Keysight N5251A	800 MHz to 40 GHz. Limited by modulator (can go up to 110 GHz) and dispersion (can be tuned)
Jitter in single-shot measurements	Not available	5.4 fs
Power	670 W for Keysight N5251A	50 W

5.6.1 Acquisition Time

Table 5.1 shows a comparison of the specifications of SiNA with a bench-top commercial vector network analyzer. The acquisition time of SiNA is 27 ns which is much faster than any commercial VNA and is due to the unique high-speed, single-shot measurements capability of SiNA. The equivalent sampling rate of SiNA in a single-shot due to time-stretching is 2.5 TSps whereas in commercial VNAs, the signal is down-converted and digitized using a lower sampling rate ADC.

5.6.2 Non-linearity

Every device used in the proposed instrumentation system has to be operated in its linear region, especially the electro-optic modulator. Although automatic bias control systems can be employed to bias the modulators within a desired linear region, MZMs are inherently a non-linear device and can add distortions to the time-stretched signal. Many techniques have been developed to suppress non-linear effects and have been discussed in Section 2.5.

5.6.3 Bandwidth and Dispersion Penalty

When performing frequency response measurements of high speed opto-electronic devices, every component that follows the DUT must able to maintain the device bandwidth. In a conventional instrument, this would require all the cables, connectors, amplifiers, and digitizers used to have very high bandwidths for testing high-speed devices. When using SiNA to perform the high bandwidth device testing, the bandwidth requirements of the components used after the time-stretching stage is greatly relaxed and also the effective resolution of the measurement is improved significantly.

The analog bandwidth of time-stretch techniques are limited by dispersion penalty [113, 114]. There are various techniques to overcome the dispersion penalty limit on the bandwidth of time-stretched ADC and are discussed in Section 2.7. Overcoming the dispersion penalty would result in an intrinsic bandwidth of 16 GHz $\times$ 50 = 800 GHz. However, the practical bandwidth is limited by the electro-optic modulator used which is 40 GHz in the reported implementation. EOM bandwidths well above 100 GHz have been reported [80–82] and therefore can be used to extend the SiNA measurement bandwidth to beyond 100 GHz. Even though commercial real-time oscilloscopes have attained analog bandwidths of over 80 GHz, the resolution of ADCs at very high frequencies diminish due to reduction in the effective number of bits [90,94]. Impulse response based measurements using SiNA is consistent with frequency response measurements performed using conventional frequency swept network analyzers or digital sampling oscilloscopes, but of course with much reduced test time.

Commercial VNAs such as Keysight N5251A provide an operational bandwidth of 300

kHz to 110 GHz. The operational bandwidth of SiNA is 800 MHz to 40 GHz based on the current EOM used. The upper limit of bandwidth of SiNA is limited by the bandwidth of the electro-optic modulator used, which can be well over 100 GHz [80–82] and is commercially available. The lower limit of the operational bandwidth of SiNA is dependent on the laser repetition rate, dispersion of DCFs and the MLL chirped pulse width. However, SiNA is capable of testing opto-electronic devices/circuits/subsystems/systems within the operational bandwidth orders of magnitude faster than commercial VNAs which would enable shorter test time reducing the test cost in production testing applications.

5.6.4 Measurement Jitter

Jitter in SiNA due to the intra-pulse jitter is significantly reduced from the back-end ADC aperture jitter due to time-stretch as explained in section 2.4. The aperture jitter of the back-end digitizer used was 270 fs (rms) and the stretch factor (M) of SiNA implementations were 8.57 for low bandwidth photo-diode testing and 50 for both high bandwidth photo-diode and electrical broadband RF amplifier testing. Based on equation 2.9, the intra-pulse jitter of SiNA is therefore ∼31.5 fs (270/8.57) for low bandwidth photo-diode test setup and ∼5.4 fs (270/50) for both high bandwidth photo-diode and electrical broadband RF amplifier test setups, which is extremely low compared to the intrinsic jitter suffered in state-of-the-art conventional electronic digitizers [130]. This results in very accurate single-shot time-domain measurements compared to conventional network analyzers, where the jitter added by the instrument has to be very accurately estimated and corrected.

5.6.5 Digital Signal Processing

The digital signal processing for the reported implementation was done on the digitized data using MATLAB. The digitized data is captured using a 16 GHz analog bandwidth real-time digital phosphor oscilloscope at a vertical scale with the highest dynamic range possible and at the sampling rate of 50 Giga-samples/s. The number of sample points collected was 20 mega-samples. The following are the processing steps performed to measure the impulse and

frequency responses:

1. Measure time-stretched laser pulse *Envelope* without any modulation;
2. Measure the DUT *Response* modulated on the time-stretched *Envelope*;
3. Apply a low pass filter to all the collected data for filtering out high frequency noise;
4. Apply moving average filter (30 filter points) to all the collected data to reduce noise by lowering the sampling rate;((50*50 GSps)/30);
5. Add a DC shift to the data to avoid division by zero and normalize the data;
6. Manually identify the start and end sample points of the *Envelope* and DUT *Response*;
7. Divide the DUT *Response* by the *Envelope* to get the envelope-corrected time-domain DUT impulse response;
8. Manually identify the start and end sample points of the the envelope-corrected time-domain DUT impulse response;
9. Perform FFT to get magnitude and phase spectrum of DUT frequency response.

De-embedding of the system response from the DUT response especially for the testing of electronic devices will be implemented in the future by de-convolution in frequency domain. Also windowing and zero-padding can be applied to increase the frequency resolution in the estimated magnitude and phase spectrum of the DUT frequency response. Automation in the identification of the start and end point of the envelope and impulse response would also be implemented in the future work.

5.7 Future Work - Single-shot Terahertz Characterization

The accurate measurement of terahertz signals has always been very challenging due to extremely high bandwidth requirements for the instrumentation system. Performing accurate

instrumentation and measurement of terahertz signals can enable a wide variety of applications from quality measurement of medicine and integrated circuits, tissue imaging, to particle accelerator measurements.

Terahertz waveforms have been generated by illuminating photo-conducting structures with femtosecond laser pulses. Such structures include Hertzian dipoles [215], resonant dipoles [216], dipoles with dielectric lenses [217], large aperture photo-conductive antennae [218], large-aperture silicon p-i-n diode [219], optical rectification in nonlinear optical crystals [220, 221], etc.

Terahertz waveforms can be detected by photo-conductive antennae [222], far-infrared interferometric techniques [218, 223], and electro-optical (EO) sampling [224]. Although photo-conductive antennae have superior detection responsivity, the resonant behavior of their Hertzian dipole structure limits the accuracy of the measurement. Far-infrared interferometric techniques result in losing of the phase information which is crucial for certain applications. Electro-optic sampling is based on the Pockels effect, in which the refractive index of a medium is modified in proportion to the applied electric field strength. In electro-optical sampling technique, the terahertz electric field is measured by modulating a probe optical pulse inside an EO crystal by changing the polarization ellipticity of the optical pulse. The polarization ellipticity modulation of the optical pulse can be analyzed to obtain the amplitude and phase of the terahertz electric field.

Time-stretch based instrumentation systems have been used for analyzing the terahertz radiation emitted by electron-bunches in a synchrotron particle accelerator [153–155]. In these implementations, electro-optic sampling technique is employed to modulate the Terahertz radiation onto the polarization of an ultra-short optical pulse of 1060 nm wavelength inside a GaP EO crystal. The Terahertz modulated optical pulse is time-stretched, converted to an electrical signal, digitized using a real-time digitizer and applied digital signal processing to recover the signal and characterize it. We propose a single-shot Terahertz measurement system using SiNA, employing phase diversity technique to mitigate the dispersive RF fading effects associated with time-stretch systems [225].

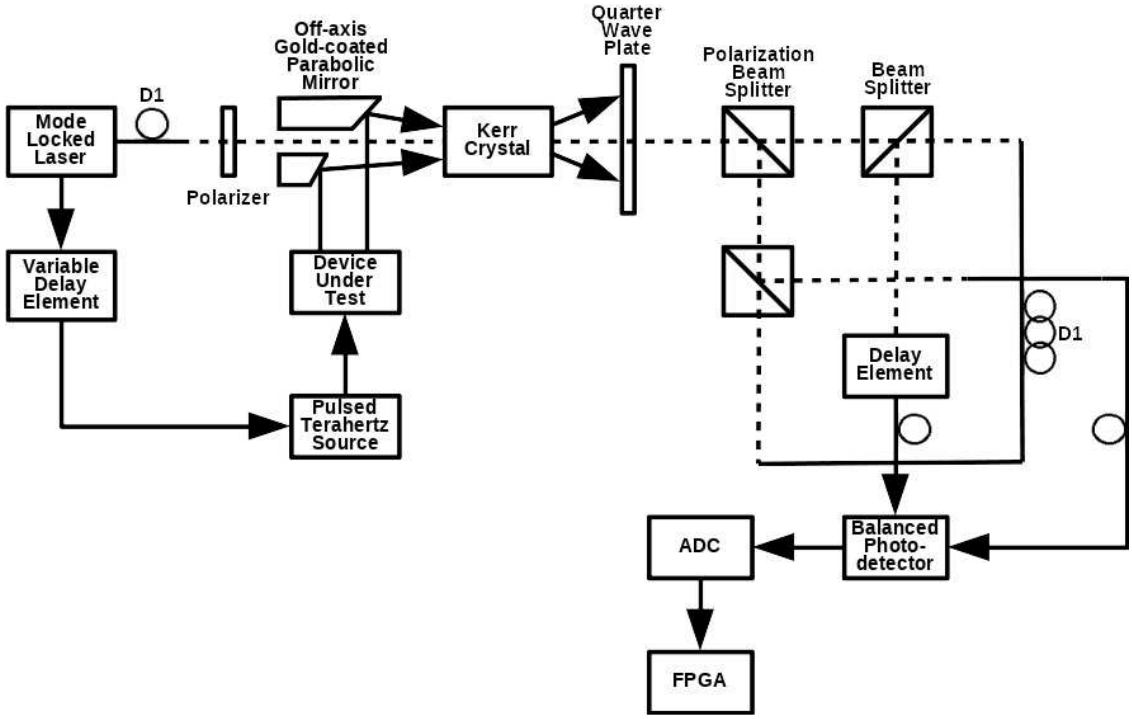

Figure 5.23: The test setup for measuring the Terahertz signals for applications such as quality measurement of medicine and integrated circuits, tissue imaging, THz device testing, etc [225].

A block diagram of the single-shot Terahertz signal measurement system can be found in Figure 5.23. The Terahertz time-stretch oscilloscope modulates the Terahertz signal under test onto a chirped mode-locked laser pulse using an electro-optic modulator comprising a Kerr crystal such as GaP or GaAs. The chirped laser pulse and the Terahertz signal are combined within the Kerr crystal which modulates the rotation of optical polarization of the chirped pulse in response to the Terahertz electric field. A quarter wave plate is used to bias the polarization of the optical signal carrying the Terahertz signal. The polarization modulation of the optical pulse is converted to intensity modulation by propagating the optical signal through a polarizing beam splitter, producing s and p polarization components. Time-stretch is applied to both the intensity modulated optical signals to compress the signal bandwidth using the same dispersion compensating fiber. The difference in the s and p polarization components is measured using a balanced photo-detector.

The balanced detector should produce no signal in the absence of a Terahertz electric field as the s and p-polarization components will have the same intensity. But the balanced detector will produce an electrical output signal in the presence of a Terahertz electric field which changes polarization of the chirped optical pulse. The resulting electrical signal from the balanced detector is digitized using an ADC. The digitized signal is analyzed using a real-time digital signal processor such as a field programmable gate array. All the digital signal processing, including Terahertz signal recovery and measurement, maximization of the signal-to-noise ratio by employing maximum ratio combining (MRC) algorithm, and distortion suppression by optical back propagation algorithm [133], are performed in real-time. A computer is used to visualize the Terahertz signals under test after the signal processing.

5.8 Conclusion

We have demonstrated an extremely fast, single-shot network analyzer for performing frequency response analysis of photo-detectors and electro-optic modulators. SiNA features an extremely fast single-shot acquisition time of 27 ns, an effective sampling rate of up to 2.5 Tera-samples/s, and an intra-pulse jitter of 5.4 fs. Frequency-domain analysis for the DUT can also be performed by applying Fourier transform on the time-domain measurement, thereby obviating the need for a wide-band frequency synthesizer, unlike conventional VNAs. The reported instrument can be modified to perform high-speed time domain reflectometry (TDR), two-port network analyses generating bode plots, transfer function analysis, pulsed s-parameter measurements and transient, non-repetitive, non-linear response analyses for high bandwidth electronic and opto-electronic devices/circuits/subsystems/systems. SiNA can also be modified to enable characterization of Terahertz signals. The instrument can also be configured to measure complex permittivity of dielectric materials at an extremely fast measurement rate, enabling its usage in high-throughput, real-time applications such as a particle flow analyzer.

CHAPTER 6

Conclusion

Time-stretch has enabled development of high-throughput, high bandwidth instruments for the real-time capture and analysis of ultra-fast signals, rare and/or single-events. In this dissertation, I employed time-stretch to design and develop ultra-fast instruments for analyzing high-bandwidth electrical and optical signals to enable the development of agile optical networks and for performing rapid frequency response measurements of high-bandwidth electrical, opto-electronic, and electro-optic devices, circuits, modules, and systems.

We developed a 2 Tera-bit/s burst-mode time-stretch accelerated processor with a real-time electronic processing back-end for analyzing bit-error rate of data rates up to 40 Giga-bit/s at an an effective sampling rate of 250 GSamples/s using an electronic digitizer of only 2.5 Giga-samples/s sampling rate with a 2 GHz analog bandwidth. This instrument avoids the manual post-processing previously used for TiSER, and thereby reduced its latency and increased its data handling capability. The burst-mode real-time time-stretch accelerated processor has a very fast acquisition time of $\sim$28 microseconds. Additionally, I enabled the communication of the estimated bit-error rate of the analyzed data signal to be provided as a feedback to a software-defined networking controller to implement flexible/agile optical communication networks.

We demonstrated in-service optical performance monitoring of 10 Giga-bit/s non-return-to-zero on-off-keying signal in a metro-scale network with real-time feedback of the bit-error rate to the software-defined networking control plane to implement an agile network that recovers from disasters. We also demonstrated for the first time, burst-mode real-time, in-service, optical performance monitoring using eye diagrams on a 10 Gbit/s non-return-to-zero on-off-keying modulated streaming video packets on a commercial optical network platform.

We characterized the bit-error rate of 10 Gigabit/s non-return-to-zero on-off-keying signals in the presence on non-linear effects namely, amplified spontaneous emission and self phase modulation using TiSAP and calibrated the measurements with a bit-error rate tester. We also report an ultra-fast time-stretch instantaneous frequency measurement receiver based on TiSER which allows for both amplitude and frequency measurements for a wide bandwidth range of 5 to 45 GHz. We also proposed a new hybrid instrumentation system based on TiSAP for analyzing both high-speed optical and electrical signals enabling ultra-fast production-level characterization of optical/opto-electronic/electro-optic devices and also modulation format agnostic, in-service analysis of optical and electrical data in a communication system.

We have demonstrated a new extremely fast, single-shot network analyzer for performing frequency response analysis of electronic, opto-electronic and electro-optic devices. SiNA features an extremely fast single-shot acquisition time of 27 ns, an effective sampling rate of 2.5 Tera-samples/s, and a measurement jitter of 5.4 fs (rms). SiNA obviates the need for a wide-band frequency synthesizer, needed in conventional vector network analyzers, by performing Fourier transform on the time-domain measurement. SiNA can be modified to enable characterization of Terahertz signals as well as for measuring complex permittivity of dielectric materials at an extremely fast measurement rate, enabling its usage in high-throughput, real-time applications such as a particle flow analyzer.

[1] John D'Ambrosia and Scott G. Kipp. The 2018 Ethernet Roadmap. *Ethernet Alliance White Paper*, 2018. xi, 1

[2] Cisco Visual Networking Index. Global Mobile Data Traffic Forecast Update, 2016–2021 White Paper [Online], March 28, 2017 (Accessed on May 3, 2018). https://www.cisco.com/c/en/us/solutions/collateral/service-provider/visual-networking-index-vni/mobile-white-paper-c11-520862.html. 1

[3] Cisco Visual Networking Index. The Zettabyte Era: Trends and Analysis [Online], June 7, 2017 (Accessed on May 3, 2018). https://www.cisco.com/c/en/us/solutions/collateral/service-provider/visual-networking-index-vni/vni-hyperconnectivity-wp.html. 1

[4] Donald Keck. A Future Full of Light. *IEEE Journal of Selected Topics in Quantum Electronics*, 6(6):1254–1258, 2000. 2

[5] Peter J. Winzer and René-Jean Essiambre. Advanced optical modulation formats. *Proceedings of the IEEE*, 94(5):952–985, 2006. 2

[6] Govind P. Agrawal. *Fiber-Optic Communication Systems*. Wiley Series in Microwave and Optical Engineering. Wiley, 2010. 2, 77

[7] Georgios Tzimpragos, Christoforos Kachris, Ivan B. Djordjevic, Milorad Cvijetic, Dimitrios Soudris, and Ioannis Tomkos. A survey on FEC codes for 100 G and beyond optical networks. *IEEE Communications Surveys & Tutorials*, 18(1):209–221, 2016. 2

[8] Giulio Colavolpe. Faster-than-Nyquist and beyond: how to improve spectral efficiency by accepting interference. In *2011 37th European Conference and Exhibition on Optical Communication*, pages 1–25, Sept 2011. 2

[9] Sethumadhavan Chandrasekhar, Xiang Liu, Benyuan Zhu, and David W. Peckham. Transmission of a 1.2-Tb/s 24-carrier no-guard-interval coherent OFDM superchannel over 7200-km of ultra-large-area fiber. In *Optical Communication, 2009. ECOC'09. 35th European Conference on*, volume 2009, pages 1–2. IEEE, 2009. 2

[10] Robert Maher, Alex Alvarado, Domaniç Lavery, and Polina Bayvel. Increasing the information rates of optical communications via coded modulation: a study of transceiver performance. *Scientific Reports*, 6:21278, 2016. 2

[11] Talha Rahman, Danish Rafique, Bernhard Spinnler, Erwan Pincemin, Claude Le Bouëtté, Jérémie Jauffrit, Stefano Calabro, Erik de Man, Sylvain Bordais, Uwe Feiste, Juraj Slovak, Antonio Napoli, Ginni Khanna, Norbert Hanik, Celine André, Chigo Okonkwo, Maxim Kuschnerov, A. M. J. Koonen, Christian Dourthe, Bruno Raguénès, Bernd Sommerkorn-Krombholz, Marc Bohn, and Huug de Waardt. Record field demonstration of C-band multi-terabit 16QAM, 32QAM and 64QAM over 762km

of SSMF. In *Opto-Electronics and Communications Conference (OECC), 2015*, pages 1–3. IEEE, 2015. 2

[12] Georg Rademacher, Ruben S Luís, Benjamin J Puttnam, Tobias A Eriksson, Erik Agrell, Ryo Maruyama, Kazuhiko Aikawa, Hideaki Furukawa, Yoshinari Awaji, and Naoya Wada. 159 Tbit/s C+ L Band Transmission over 1045 km 3-Mode Graded-Index Few-Mode Fiber. In *Optical Fiber Communication Conference*, pages Th4C–4. Optical Society of America, 2018. 2

[13] Hao Hu, Francesco Da Ros, Minhao Pu, Feihong Ye, Kasper Ingerslev, Edson Porto da Silva, Md. Nooruzzaman, Yoshimichi Amma, Yusuke Sasaki, Takayuki Mizuno, Yutaka Miyamoto, Luisa Ottaviano, Elizaveta Semenova, Pengyu Guan, Darko Zibar, Michael Galili, Kresten Yvind, Toshio Morioka, and Leif K. Oxenløwe. Single-source chip-based frequency comb enabling extreme parallel data transmission. *Nature Photonics*, page 1, 2018. 2

[14] Yu Rong Zhou, Kevin Smith, Roger Payne, Andrew Lord, Jonathan Hopewell, John Weatherhead, Jingxin Chen, Jiankang Yao, Wei Liu, Chen Zhao, Yong Xiong, Zhimin Xiao, and Peiyuan Du. Field Demonstration of up to 3 Tb/s Real-Time Superchannel Transport Over 359 km Using a Fully Managed Flexible Grid Infrastructure With Net Spectral Efficiency of 5.97 b/s/Hz. *Journal of Lightwave Technology*, 34(2):805–811, Jan 2016. 2

[15] Robert Maher, Kevin Croussore, Matthias Lauermann, Ryan Going, Xian Xu, and Jeff Rahn. Constellation shaped 66 GBd DP-1024QAM transceiver with 400 km transmission over standard SMF. In *Optical Communication (ECOC), 2017 European Conference on*, pages 1–3. IEEE, 2017. 2

[16] Omar Ait Sab, Amirhossein Ghazisaeidi, Philippe Plantady, Alain Calsat, Ivan Fernandez de Jauregui Ruiz, Suwimol Dubost, Pascal Pecci, Jeremie Renaudier, and Vincent Letellier. 376 Pb/s×km Transmission Record over 13,419km Using TPCS-64QAM and C-Band EDFA-Only. In *Asia Communications and Photonics Conference*, pages Su2B–2. Optical Society of America, 2017. 2

[17] Infinera Corporation. Infinera and Seaborn Set Subsea Industry Benchmark for Capacity - Reach with XTS - 3300 on Seabras - 1 [Online], September 20, 2017 (Accessed on May 3, 2018). https://www.infinera.com/wp-content/uploads/pr-20170921-seaborn-subsea-benchmark-capacity-reach-xts-3300-seabras-1.pdf. 2

[18] Ori Gerstel, Masahiko Jinno, Andrew Lord, and S. J. Ben Yoo. Elastic optical networking: A new dawn for the optical layer? *IEEE Communications Magazine*, 50(2), 2012. 2

[19] Cisco Visual Networking Index. Cisco Global Cloud Index: Forecast and Methodology, 2016–2021 White Paper [Online], February 1, 2018 (Accessed on May 3, 2018). https://www.cisco.com/c/en/us/solutions/collateral/service-provider/global-cloud-index-gci/white-paper-c11-738085.html. 2

[20] Daniel J. Blumenthal, John Barton, Neda Beheshti, John E. Bowers, Emily Burmeister, Larry A. Coldren, Matt Dummer, Garry Epps, Alexander Fang, Yashar Ganjali, John Garcia, Brian Koch, Vikrant Lal, Erica Lively, John Mack, Milan Masanović, Nick McKeown, Kim Nguyen, Steven C. Nicholes, Hyundai Park, Biljana Stamenic, Anna Tauke-Pedretti, Henrik Poulsen, and Matt Sysak. Integrated photonics for low-power packet networking. *IEEE Journal of Selected Topics in Quantum Electronics*, 17(2):458–471, 2011. 3

[21] Sean Koehl, Ansheng Liu, and Mario Paniccia. Integrated silicon photonics: Harnessing the data explosion. *Optics and Photonics News*, 22(3):24–29, 2011. 3

[22] Richard Soref. The past, present, and future of silicon photonics. *IEEE Journal of Selected Topics in Quantum Electronics*, 12(6):1678–1687, 2006. 3

[23] Bahram Jalali and Sasan Fathpour. Silicon Photonics. *Journal of lightwave technology*, 24(12):4600–4615, 2006. 3

[24] Yurii A Vlasov. Silicon CMOS-integrated nano-photonics for computer and data communications beyond 100G. *IEEE Communications Magazine*, 50(2), 2012. 3

[25] Christopher Richard Doerr. Silicon photonic integration in telecommunications. *Frontiers in Physics*, 3:37, 2015. 3

[26] Cathy Yunshan Jiang, Peter T. S. DeVore, Cejo Konuparamban Lonappan, Jost Adam, and Bahram Jalali. SiCloud: An online education tool for silicon photonics. In *Education and Training in Optics and Photonics: ETOP 2017, 14th Conference on*, volume 10452, pages 10452 – 10452 – 5, August 2017. 3

[27] Thomas L Koch and Uziel Koren. Semiconductor photonic integrated circuits. *IEEE Journal of Quantum Electronics*, 27(3):641–653, 1991. 3

[28] Günther Roelkens, Liu Liu, Di Liang, Richard Jones, Alexander Fang, Brian Koch, and John Bowers. III-V/silicon photonics for on-chip and intra-chip optical interconnects. *Laser & Photonics Reviews*, 4(6):751–779, 2010. 3

[29] Meint Smit, Xaveer Leijtens, Erwin Bente, Jos van der Tol, Huub Ambrosius, David Robbins, Mike Wale, Norbert Grote, and Martin Schell. A generic foundry model for InP-based photonic ICs. In *Optical Fiber Communication Conference and Exposition (OFC/NFOEC), 2012 and the National Fiber Optic Engineers Conference*, pages 1–3. IEEE, 2012. 3

[30] R. Going, M. Lauermann, R. Maher, H. Tsai, M. Lu, N. Kim, S. Corzine, P. Studenkov, J. Summers, A. Hosseini, J. Zhang, B. Behnia, J. Tang, S. Buggaveeti, T. Vallaitis, J. Osenbach, M. Kuntz, X. Xu, K. Croussore, V. Lal, P. Evans, J. Rahn, T. Butrie, A. Karanicolas, K. . Wu, M. Mitchell, M. Ziari, D. Welch, and F. Kish. Multi-channel InP-based Coherent PICs with Hybrid Integrated SiGe Electronics Operating up to 100 GBd, 32QAM. In *Optical Communication (ECOC), 2017 European Conference on*, pages 1–3. IEEE, 2017. 3

[31] Di Liang, Gunther Roelkens, Roel Baets, and John E Bowers. Hybrid integrated platforms for silicon photonics. *Materials*, 3(3):1782–1802, 2010. 3

[32] Xuezhe Zheng, Dinesh Patil, Jon Lexau, Frankie Liu, Guoliang Li, Hiren Thacker, Ying Luo, Ivan Shubin, Jieda Li, Jin Yao, Po Dong, Dazeng Feng, Mehdi Asghari, Thierry Pinguet, Attila Mekis, Philip Amberg, Michael Dayringer, Jon Gainsley, Hesam Fathi Moghadam, Elad Alon, Kannan Raj, Ron Ho, John E. Cunningham, and Ashok V. Krishnamoorthy. Ultra-efficient 10Gb/s hybrid integrated silicon photonic transmitter and receiver. *Optics Express*, 19(6):5172–5186, 2011. 3

[33] Martijn JR Heck, Jared F Bauters, Michael L Davenport, Jonathan K Doylend, Siddharth Jain, Géza Kurczveil, Sudharsanan Srinivasan, Yongbo Tang, and John E Bowers. Hybrid silicon photonic integrated circuit technology. *IEEE Journal of Selected Topics in Quantum Electronics*, 19(4):6100117, 2013. 3

[34] Qixiang Cheng, Sébastien Rumley, Meisam Bahadori, and Keren Bergman. Photonic switching in high performance datacenters. *Optics Express*, 26(12):16022–16043, 2018. 3

[35] Günther Roelkens, Joost Brouckaert, Dries Van Thourhout, Roel Baets, R Nötzel, and Meint Smit. Adhesive bonding of InP/ InGaAsP dies to processed silicon-on-insulator wafers using DVS-bis-benzocyclobutene. *Journal of the Electrochemical Society*, 153(12):G1015–G1019, 2006. 3

[36] Joris Van Campenhout, P Rojo-Romeo, P Regreny, C Seassal, Dries Van Thourhout, Steven Verstuyft, L Di Cioccio, J-M Fedeli, C Lagahe, and Roel Baets. Electrically pumped InP-based microdisk lasers integrated with a nanophotonic silicon-on-insulator waveguide circuit. *Optics Express*, 15(11):6744–6749, 2007. 3

[37] Tin Komljenovic, Michael Davenport, Jared Hulme, Alan Y Liu, Christos T Santis, Alexander Spott, Sudharsanan Srinivasan, Eric J Stanton, Chong Zhang, and John E Bowers. Heterogeneous silicon photonic integrated circuits. *Journal of Lightwave Technology*, 34(1):20–35, 2016. 3

[38] Nahum Izhaky, Michael T. Morse, Sean Koehl, Oded Cohen, Doron Rubin, Assia Barkai, Gadi Sarid, Rami Cohen, and Mario J. Paniccia. Development of CMOS-compatible integrated silicon photonics devices. *IEEE Journal of Selected Topics in Quantum Electronics*, 12(6):1688–1698, 2006. 3

[39] Lars Zimmermann, Giovan Battista Preve, Tolga Tekin, Thomas Rosin, and Kennedy Landles. Packaging and assembly for integrated photonicsâĂŤa review of the epixpack photonics packaging platform. *IEEE Journal of Selected Topics in Quantum Electronics*, 17(3):645–651, 2011. 3

[40] Nicola Pavarelli, Jun Su Lee, Marc Rensing, Carmelo Scarcella, Shiyu Zhou, Peter Ossieur, and Peter A O'Brien. Optical and electronic packaging processes for silicon photonic systems. *Journal of Lightwave Technology*, 33(5):991–997, 2015. 3

[41] Ashok V. Krishnamoorthy, Hiren D. Thacker, Ola Torudbakken, Shimon Müller, Arvind Srinivasan, Patrick J. Decker, Hans Opheim, John E. Cunningham, Ivan Shubin, Xuezhe Zheng, Marcelino Dignum, Kannan Raj, Eivind Rongved, and Raju Penumatcha. From chip to cloud: Optical interconnects in engineered systems. *Journal of Lightwave Technology*, 35(15):3103–3115, 2017. 3

[42] Ola Torudbakken and Ashok V Krishnamoorthy. A 50 Tbps optically-cabled infiniband datacenter switch. In *Optical Fiber Communication Conference and Exposition and the National Fiber Optic Engineers Conference (OFC/NFOEC), 2013*, pages 1–3. IEEE, 2013. 3

[43] DJ Richardson, JM Fini, and LE Nelson. Space-division multiplexing in optical fibres. *Nature Photonics*, 7(5):354, 2013. 3

[44] RGH Van Uden, R Amezcua Correa, E Antonio Lopez, FM Huijskens, Cen Xia, G Li, A Schülzgen, H De Waardt, AMJ Koonen, and CM Okonkwo. Ultra-high-density spatial division multiplexing with a few-mode multicore fibre. *Nature Photonics*, 8(11):865, 2014. 3

[45] Jun Sakaguchi, Werner Klaus, J-MD Mendinueta, Benjamin J Puttnam, Ruben Soares Luìs, Yoshinari Awaji, Naoya Wada, Tetsuya Hayashi, Tetsuya Nakanishi, Tatsuhiko Watanabe, Yasuo Kokubun, Taketoshi Takahata, and Tetsuya Kobayashi. Realizing a 36-core, 3-mode fiber with 108 spatial channels. In *Optical Fiber Communications Conference and Exhibition (OFC), 2015*, pages 1–3. IEEE, 2015. 3

[46] Dan M Marom and Miri Blau. Switching solutions for WDM-SDM optical networks. *IEEE Communications Magazine*, 53(2):60–68, 2015. 3

[47] Alan Willner, Xiaoxia Wu, and Jeng-Yuan Yang. 1 - Optical performance monitoring: Perspectives and challenges. In Calvin C.K. Chan, editor, *Optical Performance Monitoring: Advanced Techniques for Next-Generation Photonic Networks*, pages 1 – 19. Academic Press, Oxford, 2010. 4, 36

[48] Calvin C. K. Chan. *Optical Performance Monitoring: Advanced Techniques for Next-Generation Photonic Networks*. Elsevier, 2010. 4, 75

[49] D. C. Kilper, R. Bach, D. J. Blumenthal, D. Einstein, T. Landolsi, L. Ostar, M. Preiss, and A. E. Willner. Optical Performance Monitoring. *Journal of Lightwave Technology*, 22(1):294, Jan 2004. 4

[50] Zhongqi Pan, Changyuan Yu, and Alan E. Willner. Optical performance monitoring for the next generation optical communication networks. *Optical Fiber Technology*, 16(1):20–45, 2010. 4

[51] Tatsumi Takagi, Hiroshi Hasegawa, Ken-ichi Sato, Yoshiaki Sone, Akira Hirano, and Masahiko Jinno. Disruption minimized spectrum defragmentation in elastic optical path networks that adopt distance adaptive modulation. In *2011 37th European Conference and Exhibition on Optical Communication*, pages 1–3, Sept 2011. 4

[52] Jochen Schröder, Owen Brasier, Jürgen Van Erps, Michaël AF Roelens, Steve Frisken, and Benjamin J Eggleton. OSNR monitoring of a 1.28 Tbaud signal by interferometry inside a wavelength-selective switch. *Journal of Lightwave Technology*, 29(10):1542–1546, 2011. 4

[53] Caroline P. Lai, Jeng-Yuan Yang, Ajay S. Garg, Michael S. Wang, Mohammad R. Chitgarha, Alan E. Willner, and Keren Bergman. Experimental demonstration of packet-rate 10-Gb/s OOK OSNR monitoring for QoS-aware cross-layer packet protection. *Optics Express*, 19(16):14871–14882, 2011. 4

[54] Zhenhua Dong, Faisal Nadeem Khan, Qi Sui, Kangping Zhong, Chao Lu, and Alan Pak Tao Lau. Optical performance monitoring: A review of current and future technologies. *Journal of Lightwave Technology*, 34(2):525–543, 2016. 4

[55] Christopher M. Miller. High-speed digital transmitter characterization using eye diagram analysis. *Hewlett Packard Journal*, 45:29–29, 1994. 4

[56] Cejo K. Lonappan, Brandon W. Buckley, Daniel Lam, Asad M. Madni, Bahram Jalali, and Jost Adam. Time-stretch accelerated processor for real-time, in-service, signal analysis. In *Signal and Information Processing (GlobalSIP), 2014 IEEE Global Conference on*, pages 707–711, Dec 2014. xiii, xvi, xvii, 5, 7, 35, 38, 39, 42, 45, 85, 86, 94

[57] G Recommendation. 694.1: Spectral grids for WDM applications: DWDM frequency grid. *International Telecommunications Union, Tech. Rep*, 2012. 6

[58] Daniel Kilper, Keren Bergman, Vincent WS Chan, Inder Monga, George Porter, and Kristin Rauschenbach. Optical networks come of age. *Optics and Photonics News*, 25(9):50–57, 2014. 6

[59] Ioannis Tomkos, Siamak Azodolmolky, Josep Solé-Pareta, Davide Careglio, and Eleni Palkopoulou. A tutorial on the flexible optical networking paradigm: State of the art, trends, and research challenges. *Proceedings of the IEEE*, 102(9):1317–1337, 2014. 6

[60] Siamak Azodolmolky, Jordi Perelló, Marianna Angelou, Fernando Agraz, Luis Velasco, Salvatore Spadaro, Yvan Pointurier, Antonio Francescon, Chava Vijaya Saradhi, Panagiotis Kokkinos, Emmanouel Varvarigos, Sawsan Al Zahr, Maurice Gagnaire, Matthias Gunkel, Dimitrios Klonidis, and Ioannis Tomkos. Experimental Demonstration of an Impairment Aware Network Planning and Operation Tool for Transparent/Translucent Optical Networks. *Journal of Lightwave Technology*, 29(4):439–448, Feb 2011. 6

[61] Jayant Baliga, Robert Ayre, Kerry Hinton, Wayne V Sorin, and Rodney S Tucker. Energy consumption in optical ip networks. *Journal of Lightwave Technology*, 27(13):2391–2403, 2009. 6

[62] Daniel Kilper, Kyle Guan, Kerry Hinton, and Robert Ayre. Energy challenges in current and future optical transmission networks. *Proceedings of the IEEE*, 100(5):1168–1187, 2012. 6

[63] Alex Vukovic. Network power density challenges. *ASHRAE journal*, 47(4):55, 2005. 7

[64] Jonathan Koomey. Growth in data center electricity use 2005 to 2010. *A report by Analytical Press, completed at the request of The New York Times*, 9, 2011. 7

[65] Jun Yan, Cejo K. Lonappan, Amir Vajid, Digvijay Singh, and William J. Kaiser. Accurate and low-overhead process-level energy estimation for modern hard disk drives. In *Green Computing and Communications (GreenCom), 2013 IEEE and Internet of Things (iThings/CPSCom), IEEE International Conference on and IEEE Cyber, Physical and Social Computing*, pages 171–178. IEEE, 2013. 7

[66] Masahiko Jinno, Hidehiko Takara, Bartlomiej Kozicki, Yukio Tsukishima, Yoshiaki Sone, and Shinji Matsuoka. Spectrum-efficient and scalable elastic optical path network: architecture, benefits, and enabling technologies. *IEEE communications magazine*, 47(11), 2009. 7

[67] Raffaele Bolla, Roberto Bruschi, Franco Davoli, and Flavio Cucchietti. Energy efficiency in the future internet: A survey of existing approaches and trends in energy-aware fixed network infrastructures. *IEEE Communications Surveys & Tutorials*, 13(2):223–244, 2011. 7

[68] Daniel C Kilper, Michael S Wang, Atiyah Ahsan, and Keren Bergman. Efficient and agile optical networks. In *Optical Network Design and Modeling (ONDM), 2013 17th International Conference on*, pages 217–222. IEEE, 2013. 7

[69] Software-Defined Networking: The New Norm for Networks [Online], October 13, 2012 (Accessed August 10, 2018). https://www.opennetworking.org/images/stories/downloads/sdn-resources/white-papers/wp-sdn-newnorm.pdf. 7

[70] OpenFlow Switch Specification 1.4 [Online], October 14, 2013 (Accessed August 10, 2018). https://www.opennetworking.org/images/stories/downloads/sdn-resources/onf-specifications/openflow/openflow-spec-v1.4.0.pdf. 7, 72

[71] Siamak Azodolmolky, Reza Nejabati, Eduard Escalona, Ramanujam Jayakumar, Nikolaos Efstathiou, and Dimitra Simeonidou. Integrated OpenFlow–GMPLS control plane: an overlay model for software defined packet over optical networks. *Optics express*, 19(26):B421–B428, 2011. 7

[72] Christoforos Kachris and Ioannis Tomkos. A survey on optical interconnects for data centers. *IEEE Communications Surveys & Tutorials*, 14(4):1021–1036, 2012. 7

[73] Steven Gringeri, Nabil Bitar, and Tiejun J. Xia. Extending Software Defined Network Principles to Include Optical Transport. *IEEE Communications Magazine*, 51(3):32–40, 2013. 7

[74] Mayur Channegowda, Reza Nejabati, and Dimitra Simeonidou. Software-defined optical networks technology and infrastructure: Enabling software-defined optical network

operations. *Journal of Optical Communications and Networking*, 5(10):A274–A282, 2013. 7

[75] Yao Li and Daniel C Kilper. Optical Physical Layer SDN. *IEEE/OSA Journal of Optical Communications and Networking*, 10(1):A110–A121, 2018. 7

[76] Daniel Lam, Brandon W. Buckley, Cejo K. Lonappan, Asad M. Madni, and Bahram Jalali. Ultra-wideband instantaneous frequency estimation. *IEEE Instrumentation Measurement Magazine*, 18(2):26–30, April 2015. xvii, xx, 7, 35, 87, 89, 90, 91, 92, 93

[77] K. Kato, A. Kozen, Y. Muramoto, Y. Itaya, T. Nagatsuma, and M. Yaita. 110-GHz, 50%-efficiency mushroom-mesa waveguide p-i-n photodiode for a 1.55-μm wavelength. *IEEE Photonics Technology Letters*, 6(6):719–721, June 1994. 8

[78] Fengnian Xia, Thomas Mueller, Yu-ming Lin, Alberto Valdes-Garcia, and Phaedon Avouris. Ultrafast graphene photodetector. *Nature Nanotechnology*, 4(12):839–843, Dec 2009. 8

[79] Qinglong Li, Kejia Li, Yang Fu, Xiaojun Xie, Zhanyu Yang, Andreas Beling, and Joe C. Campbell. High-Power Flip-Chip Bonded Photodiode With 110 GHz Bandwidth. *Journal of Lightwave Technology*, 34(9):2139–2144, May 2016. 8

[80] Datong Chen, Harold R. Fetterman, Antao Chen, William H. Steier, Larry R. Dalton, Wenshen Wang, and Yongqiang Shi. Demonstration of 110 GHz electro-optic polymer modulators. *Applied Physics Letters*, 70(25):3335–3337, 1997. 8, 67, 118, 119

[81] Datong Chen, D. Bhattacharya, A. Udupa, B. Tsap, H. R. Fetterman, Antao Chen, Sang-Shin Lee, Jinghong Chen, W. H. Steier, and L. R. Dalton. High-frequency polymer modulators with integrated finline transitions and low V_π. *IEEE Photonics Technology Letters*, 11(1):54–56, Jan 1999. 8, 67, 118, 119

[82] Luca Alloatti, Robert Palmer, Sebastian Diebold, Kai Philipp Pahl, Baoquan Chen, Raluca Dinu, Maryse Fournier, Jean-Marc Fedeli, Thomas Zwick, Wolfgang Freude, Christian Koos, and Juerg Leuthold. 100 GHz silicon–organic hybrid modulator. *Light: Science & Applications*, 3:e173, May 2014. 8, 67, 118, 119

[83] Melanie Po-Leen Ooi, Zainal Abu Kassim, and Serge N Demidenko. Shortening burn-in test: Application of HVST and Weibull statistical analysis. *IEEE Transactions on Instrumentation and Measurement*, 56(3):990–999, 2007. 8

[84] Mukesh Agrawal and Krishnendu Chakrabarty. Test-cost modeling and optimal test-flow selection of 3-D-stacked ICs. *IEEE Transactions on Computer-Aided Design of Integrated Circuits and Systems*, 34(9):1523–1536, 2015. 8

[85] Bahram Jalali, Cejo Konuparamban Lonappan, and Asad M. Madni. Single-shot network analyzer (SiNA), 2016. WO Patent Application, WO2017223149A1. 8, 97

[86] Cejo Konuparamban Lonappan, Asad M. Madni, and Bahram Jalali. Single-shot network analyzer for extremely fast measurements. *Applied Optics*, 55(30):8406–8412, 2016. xvii, 8, 35, 97, 98, 99

[87] Manar El-Chammas and Boris Murmann. *Background calibration of time-interleaved data converters*. Springer Science & Business Media, 2011. xi, 10, 11

[88] Naoki Kurosawa, Haruo Kobayashi, Kaoru Maruyama, Hidetake Sugawara, and Kensuke Kobayashi. Explicit analysis of channel mismatch effects in time-interleaved ADC systems. *IEEE Transactions on Circuits and Systems I: Fundamental Theory and Applications*, 48(3):261–271, 2001. 11

[89] Behzad Razavi. Design considerations for interleaved ADCs. *IEEE Journal of Solid-State Circuits*, 48(8):1806–1817, 2013. 11

[90] Robert H. Walden. Analog-to-digital converter survey and analysis. *IEEE Journal on Selected Areas in Communications*, 17(4):539–550, Apr 1999. xi, 11, 12, 13, 20, 22, 26, 37, 67, 97, 118

[91] Boris Murmann. ADC Performance Survey 1997-2018 [Online], 2018 (Accessed August 16, 2018). `http://www.stanford.edu/~murmann/adcsurvey.html`. xi, 12, 13, 20, 22, 37, 67, 97

[92] Willie W. Ng, Troy D. Rockwood, George Anthony Sefler, and George C. Valley. Demonstration of a Large Stretch-Ratio (M=41) Photonic Analog-to-Digital Converter With 8 ENOB for an Input Signal Bandwidth of 10 GHz. *IEEE Photonics Technology Letters*, 24(14):1185–1187, 2012. xi, 12, 17

[93] Willie W. Ng, Troy D. Rockwood, and Alan E. Reamon. Demonstration of channel-stitched photonic time-stretch analog-to-digital converter with ENOB$\geq$ 8 for a 10 GHz signal bandwidth. In *Proceedings of the Government Microcircuit Applications & Critical Technology Conference (GOMACTech'14)*, 2014. xi, 12, 17

[94] Boris Murmann. A/D converter trends: Power dissipation, scaling and digitally assisted architectures. In *2008 IEEE Custom Integrated Circuits Conference*, pages 105–112, Sept 2008. 13, 22, 37, 67, 97, 118

[95] Shalabh Gupta, George C. Valley, Robert H. Walden, and Bahram Jalali. Power scaling in photonic time-stretched analog-to-digital converters. In *2009 IEEE Avionics, Fiber-Optics and Phototonics Technology Conference*, pages 5–6, Sept 2009. xii, 13, 23, 27, 37

[96] Richard W. Anderson and Orthell T. Dennison. An advanced new network analyzer for sweep measuring amplitude and phase from 0.1 to 12.4 GHz. *Hewlett-Packard Journal*, 18(6), 1967. 13

[97] François Ziadé, André Poletaeff, and Djamel Allal. Primary standard for s-parameter measurements at intermediate frequencies (ifs). *IEEE Trans. Instrumentation and Measurement*, 62(3):659–666, 2013. 13

[98] Valeria Teppati and Andrea Ferrero. A Comparison of Uncertainty Evaluation Methods for On-Wafer S-Parameter Measurements. *IEEE Transactions on Instrumentation and Measurement*, 63(4):935–942, 2014. 13

[99] N.H. Zhu, Y. Liu, E.Y.B. Pun, and P.S. Chung. Scattering-parameter measurements of laser diodes. *Optical and Quantum Electronics*, 34(8):747–757, 2002. 13, 97

[100] Alexander M. Nicolson. Broad-band microwave transmission characteristics from a single measurement of the transient response. *IEEE Transactions on Instrumentation and Measurement*, 17(4):395–402, 1968. 13

[101] Philippe Ferrari and Gilbert Angenieux. A simulation technique for the evaluation of random error effects in time-domain measurement systems. *IEEE Transactions on Instrumentation and Measurement*, 50(3):665–671, 2001. 13

[102] Denis Barataud, Caroline Arnaud, Barbara Thibaud, Michel Campovecchio, J-M Nebus, and Jean Pierre Villotte. Measurements of time-domain voltage/current waveforms at RF and microwave frequencies based on the use of a vector network analyzer for the characterization of nonlinear devices-application to high-efficiency power amplifiers and frequency-multipliers optimization. *IEEE Transactions on Instrumentation and Measurement*, 47(5):1259–1264, 1998. 13

[103] Wendy Van Moer and Yves Rolain. An improved broadband conversion scheme for the large-signal network analyzer. *IEEE Transactions on Instrumentation and Measurement*, 58(2):483–487, 2009. 13

[104] Jan Verspecht and Ken Rush. Individual characterization of broadband sampling oscilloscopes with a nose-to-nose calibration procedure. *IEEE Transactions on instrumentation and measurement*, 43(2):347–354, 1994. 13

[105] Jeffrey A. Jargon, Paul D. Hale, and Chih-Ming Wang. Correcting sampling oscilloscope timebase errors with a passively mode-locked laser phase locked to a microwave oscillator. *IEEE Transactions on Instrumentation and Measurement*, 59(4):916–922, 2010. 13

[106] Maximilian Hofmann, Georg Fischer, Robert Weigel, and Dietmar Kissinger. Microwave-based noninvasive concentration measurements for biomedical applications. *IEEE Transactions on Microwave Theory and Techniques*, 61(5):2195–2204, 2013. 14

[107] Emanuele Piuzzi, Caterina Merla, Giuseppe Cannazza, Alessandro Zambotti, Francesca Apollonio, Andrea Cataldo, Paolo D'Atanasio, Egidio De Benedetto, and Micaela Liberti. A comparative analysis between customized and commercial systems for complex permittivity measurements on liquid samples at microwave frequencies. *IEEE Transactions on Instrumentation and Measurement*, 62(5):1034–1046, 2013. 14

[108] Xuezhi Zeng, Andreas Fhager, Zhongxia He, Mikael Persson, Peter Linner, and Herbert Zirath. Development of a time domain microwave system for medical diagnostics. *IEEE Transactions on Instrumentation and Measurement*, 63(12):2931–2939, 2014. 14

[109] Adam Santorelli, Emily Porter, Eric Kang, Taylor Piske, Milica Popović, and Joshua D. Schwartz. A time-domain microwave system for breast cancer detection using a flexible circuit board. *IEEE Transactions on Instrumentation and Measurement*, 64(11):2986–2994, 2015. 14

[110] Ata Mahjoubfar, Dmitry V. Churkin, Stéphane Barland, Neil Broderick, Sergei K. Turitsyn, and Bahram Jalali. Time stretch and its applications. *Nature Photonics*, 11(6):341, 2017. xi, xiii, 14, 18, 34, 37

[111] Asuri S. Bhushan, Frederic Marie Alain Coppinger, and Bahram Jalali. Time-stretched analogue-to-digital conversion. *Electronics Letters*, 34(9):839–841, 1998. 14, 15, 37, 97

[112] Bahram Jalali and Frederic Marie Alain Coppinger. Data conversion using time manipulation, September 2001. US Patent US6288659B1. 14, 15, 37, 97

[113] Ali Motafakker-Fard, Shalabh Gupta, and Bahram Jalali. Photonic time-stretch digitizer and its extension to real-time spectroscopy and imaging. *Laser & Photonics Reviews*, 7(2):207–263, 2013. xi, xii, 14, 15, 17, 23, 37, 67, 97, 118

[114] Yan Han and Bahram Jalali. Photonic time-stretched analog-to-digital converter: Fundamental concepts and practical considerations. *Journal of Lightwave Technology*, 21(12):3085–3103, Dec 2003. xii, 15, 18, 24, 28, 30, 37, 67, 97, 118

[115] George C. Valley, George A. Sefler, Jason Chou, and Bahram Jalali. Continuous time realization of time-stretch ADC. In *2006 International Topical Meeting on Microwave Photonics*, pages 1–3, Oct 2006. 15, 37, 69

[116] Yan Han and Bahram Jalali. Continuous-time time-stretched analog-to-digital converter array implemented using virtual time gating. *IEEE Transactions on Circuits and Systems I: Regular Papers*, 52(8):1502–1507, 2005. xi, 16

[117] Shalabh Gupta and Bahram Jalali. Time-warp correction and calibration in photonic time-stretch analog-to-digital converter. *Optics Letters*, 33(22):2674–2676, Nov 2008. 16, 26

[118] Jason Chou, Ozdal Boyraz, Daniel Solli, and Bahram Jalali. Femtosecond real-time single-shot digitizer. *Applied Physics Letters*, 91(16):161105, 2007. 17

[119] Shalabh Gupta and Bahram Jalali. Time stretch enhanced recording oscilloscope. *Applied Physics Letters*, 94(4):041105, 2009. xii, 17, 19, 20, 21, 22, 37, 38

[120] Ali Motafakker-Fard. *Photonic Time-Stretch for High-Speed Analog-to-Digital Conversion and Imaging*. Ph.D dissertation, Department of Electrical Engineering, University of California, Los Angeles, CA 90095, 2011. 17, 22, 37

[121] Brandon W. Buckley. *Ultra-high Throughput Real-time Instruments for Capturing Fast Signals and Rare Events*. Ph.D dissertation, Department of Physics, University of California, Los Angeles, CA 90095, 2013. xiii, xiv, xvii, 17, 22, 32, 33, 37, 40, 41, 43, 45, 48, 51, 52, 54, 59, 87, 89, 90, 91

[122] Eric D Diebold, Nick K Hon, Zhongwei Tan, Jason Chou, Todd Sienicki, Chao Wang, and Bahram Jalali. Giant tunable optical dispersion using chromo-modal excitation of a multimode waveguide. *Optics Express*, 19(24):23809–23817, 2011. 18

[123] Chinlon Lin and Rogers H. Stolen. New nanosecond continuum for excited-state spectroscopy. *Applied Physics Letters*, 28(4):216–218, 1976. 18

[124] Daniel R. Solli, Bahram Jalali, and Claus Ropers. Seeded supercontinuum generation with optical parametric down-conversion. *Physical Review Letters*, 105(23):233902, 2010. 18

[125] Keisuke Goda and Bahram Jalali. Dispersive fourier transformation for fast continuous single-shot measurements. *Nature Photonics*, 7(2):102–112, Feb 2013. 18, 97

[126] Mike Li. *Jitter, Noise, and Signal Integrity at High-speed*. Prentice Hall Press, Upper Saddle River, NJ, USA, first edition, 2007. 21

[127] Yi Cai, S. A. Werner, G. J. Zhang, M. J. Olsen, and R. D. Brink. Jitter testing for multi-gigabit backplane serdes-techniques to decompose and combine various types of jitter. In *Test Conference, 2002. Proceedings. International*, pages 700–709. IEEE, 2002. 22

[128] Ali Motafakker-Fard, Shalabh Gupta, and Bahram Jalali. Eye diagram measurements and equalization with real-time burst sampling. In *Instrumentation and Measurement Technology Conference (I2MTC), 2010 IEEE*, pages 1030–1032. IEEE, 2010. 22

[129] Tae Keun Kim, Youjian Song, Kwangyun Jung, Chur Kim, Hyoji Kim, Chang Hee Nam, and Jungwon Kim. Sub-100-as timing jitter optical pulse trains from mode-locked Er-fiber lasers. *Optics Letters*, 36(22):4443–4445, 2011. 23

[130] Kostas Doris, Erwin Janssen, Claudio Nani, Athon Zanikopoulos, and Gerard Van der Weide. A 480 mW 2.6 GS/s 10b Time-Interleaved ADC With 48.5 dB SNDR up to Nyquist in 65 nm CMOS. *IEEE Journal of Solid-State Circuits*, 46(12):2821–2833, Dec 2011. 23, 68, 97, 119

[131] Shalabh Gupta, George C Valley, and Bahram Jalali. Distortion cancellation in time-stretch analog-to-digital converter. *Journal of Lightwave Technology*, 25(12):3716–3721, 2007. 25

[132] Johan Stigwall and Sheila Galt. Signal reconstruction by phase retrieval and optical backpropagation in phase-diverse photonic time-stretch systems. *Journal of Lightwave Technology*, 25(10):3017–3027, 2007. 25

[133] Shalabh Gupta, Bahram Jalali, Johan Stigwall, and Sheila Galt. Demonstration of Distortion Suppression in Photonic Time-Stretch ADC using Back Propagation Method. In *Microwave Photonics, 2007 IEEE International Topical Meeting on*, pages 141–144, Oct 2007. 25, 123

[134] S Dubovitsky, WH Steier, and S Yegnanarayanan. Analysis and improvement of mach-zehnder modulator linearity performance for chirped and tunable optical carriers. *Journal of Lightwave Technology*, 20(5):858, 2002. 25

[135] Ali Motafakker-Fard, Shalabh Gupta, and Bahram Jalali. Digital broadband linearization technique and its application to photonic time-stretch analog-to-digital converter. *Optics Letters*, 36(7):1077–1079, 2011. 25

[136] Daniel Lam, Ali Motafakker-Fard, Brandon Buckley, and Bahram Jalali. Digital broadband linearization of optical links. *Optics Letters*, 38(4):446–448, 2013. 25

[137] Ram Sadhwani and Bahram Jalali. Adaptive CMOS predistortion linearizer for fiber-optic links. *Journal of Lightwave Technology*, 21(12):3180, 2003. 25

[138] Juthika Basak and Bahram Jalali. Photodetector Linearization Using Adaptive Electronic Postdistortion. In *Optical Fiber Communication Conference*, page OThR2. Optical Society of America, 2005. 25

[139] Keisuke Goda, Daniel R Solli, Kevin K Tsia, and Bahram Jalali. Theory of amplified dispersive fourier transformation. *Physical Review A*, 80(4):043821, 2009. 25

[140] Ata Mahjoubfar, Keisuke Goda, Gary Betts, and Bahram Jalali. Optically amplified detection for biomedical sensing and imaging. *Journal of the Optical Society of America A*, 30(10):2124–2132, 2013. 25

[141] Anne-Johan Annema. Analog circuit performance and process scaling. *IEEE Transactions on Circuits and Systems II: Analog and Digital Signal Processing*, 46(6):711–725, 1999. 26

[142] Yan Han and Bahram Jalali. Time-bandwidth product of the photonic time-stretched analog-to-digital converter. *IEEE Transactions on Microwave Theory and Techniques*, 51(7):1886–1892, 2003. 28, 30

[143] Ali Motafakker-Fard, Brandon Buckley, Sanja Zlatanovic, Camille-Sophie Brès, Stojan Radic, and Bahram Jalali. All-optical time-stretch digitizer. *Applied Physics Letters*, 101(5):051113, 2012. xii, xiii, 28, 31, 32, 94

[144] Theodore S. Rappaport. *Wireless Communications: Principles and Practice*, volume 2. Prentice Hall PTR New Jersey, 1996. 29

[145] Yan Han, Ozdal Boyraz, and Bahram Jalali. Ultrawide-band photonic time-stretch A/D converter employing phase diversity. *IEEE Transactions on Microwave Theory and Techniques*, 53(4):1404–1408, April 2005. xiii, 29, 31

[146] Jose M. Fuster, Dalma Novak, Ampalavanapillai Nirmalathas, and Javier Marti. Single-sideband modulation in photonic time-stretch analogue-to-digital conversion. *Electronics Letters*, 37(1):67–68, Jan 2001. 31

[147] Brandon W. Buckley, Asad M. Madni, and Bahram Jalali. Coherent time-stretch transformation for real-time capture of wideband signals. *Optics Express*, 21(18):21618–21627, Sep 2013. xiii, 32, 33, 37

[148] Daniel R. Solli, Claus Ropers, Prakash Koonath, and Bahram Jalali. Optical rogue waves. *Nature*, 450(7172):1054–1057, Dec 2007. 33

[149] Antoine F. J. Runge, Neil G. R. Broderick, and Miro Erkintalo. Observation of soliton explosions in a passively mode-locked fiber laser. *Optica*, 2(1):36–39, 2015. 33

[150] Antoine F. J. Runge, Neil G. R. Broderick, and Miro Erkintalo. Dynamics of soliton explosions in passively mode-locked fiber lasers. *Journal of the Optical Society of America B*, 33(1):46–53, 2016. 33

[151] Georg Herink, B Jalali, Claus Ropers, and Daniel R. Solli. Resolving the build-up of femtosecond mode-locking with single-shot spectroscopy at 90 mhz frame rate. *Nature Photonics*, 10(5):321, 2016. 33

[152] Georg Herink, Felix Kurtz, Bahram Jalali, Daniel R. Solli, and Claus Ropers. Real-time spectral interferometry probes the internal dynamics of femtosecond soliton molecules. *Science*, 356(6333):50–54, 2017. 33

[153] Eleonore Roussel, Clément Evain, Marc Le Parquier, Christophe Szwaj, Serge Bielawski, Laurent Manceron, Jean-Blaise Brubach, Marie-Agnès Tordeux, Jean-Paul Ricaud, Lodovico Cassinari, Marie Labat, Marie-Emmanuelle Couprie, and Pascale Roy. Observing microscopic structures of a relativistic object using a time-stretch strategy. *Scientific Reports*, 5:10330, 2015. 33, 121

[154] Christophe Szwaj, Clément Evain, Marc Le Parquier, Pascale Roy, Laurent Manceron, Jean-Blaise Brubach, Marie-Agnès Tordeux, and Serge Bielawski. High sensitivity photonic time-stretch electro-optic sampling of terahertz pulses. *Review of Scientific Instruments*, 87(10):103111, 2016. 33, 121

[155] Clément Evain, Eleonore Roussel, Marc Le Parquier, Christophe Szwaj, Marie-Agnès Tordeux, Jean-Blaise Brubach, Laurent Manceron, Pascale Roy, and Serge Bielawski. Direct observation of spatiotemporal dynamics of short electron bunches in storage rings. *Physical Review Letters*, 118(5):054801, 2017. 33, 121

[156] K Goda, KK Tsia, and B Jalali. Serial time-encoded amplified imaging for real-time observation of fast dynamic phenomena. *Nature*, 458(7242):1145, 2009. 33

[157] Keisuke Goda, Ali Ayazi, Daniel R. Gossett, Jagannath Sadasivam, Cejo K. Lonappan, Elodie Sollier, Ali Motafakker-Fard, Soojung Claire Hur, Jost Adam, Coleman Murray, Chao Wang, Nora Brackbill, Dino Di Carlo, and Bahram Jalali. High-throughput single-microparticle imaging flow analyzer. *Proceedings of the National Academy of Sciences*, 109(29):11630–11635, 2012. 33

[158] Ata Mahjoubfar, Claire Chen, Kayvan R Niazi, Shahrooz Rabizadeh, and Bahram Jalali. Label-free high-throughput cell screening in flow. *Biomedical Optics Express*, 4(9):1618–1625, 2013. 33

[159] Claire Lifan Chen, Ata Mahjoubfar, Li-Chia Tai, Ian K. Blaby, Allen Huang, Kayvan Reza Niazi, and Bahram Jalali. Deep learning in label-free cell classification. *Scientific Reports*, 6:21471, 2016. 33

[160] Ata Mahjoubfar, Keisuke Goda, Ali Ayazi, Ali Fard, Sang Hyup Kim, and Bahram Jalali. High-speed nanometer-resolved imaging vibrometer and velocimeter. *Applied Physics Letters*, 98(10):101107, 2011. 33

[161] Benjamin Wetzel, Alessio Stefani, Laurent Larger, Pierre-Ambroise Lacourt, Jean-Marc Merolla, Thibaut Sylvestre, Alexandre Kudlinski, Arnaud Mussot, Goëry Genty, Frédéric Dias, and John M. Dudley. Real-time full bandwidth measurement of spectral noise in supercontinuum generation. *Scientific reports*, 2:882, 2012. 35

[162] Time-Stretch ADC Design Calculator [Online]. http://photonics.ucla.edu/host/media/interactive/tiser_calc/TISER/TiSER.php. Accessed August 16, 2018. 35

[163] Time-Stretch Dispersive Fourier Transform Design Calculator [Online]. http://photonics.ucla.edu/host/media/interactive/dft_calc/DFT/dispersioncalc.php. Accessed August 16, 2018. 35

[164] Caroline P. Lai, Daniel Brunina, Brandon W. Buckley, Cedric Ware, Wenjia Zhang, Ajay S. Garg, Bahram Jalali, and Keren Bergman. First demonstration of a cross-layer enabled network node. *Journal of Lightwave Technology*, 31(9):1512–1525, 2013. 36

[165] Mike Golio. *The RF and Microwave Handbook*. CRC press, 2000. 37

[166] Stamatios V. Kartalopoulos. Channel protection with real-time and in-service performance monitoring for next generation secure WDM networks. In *2007 IEEE International Conference on Communications*, pages 1235–1240, June 2007. 37

[167] National Semiconductors (Texas Instruments). *ADC083000 8-Bit, 3 GSPS, High Performance, Low Power A/D Converter Datasheet [Online]*. http://www.ti.com/lit/ds/symlink/adc083000.pdf. 42

[168] Xilinx Inc. *Virtex-6 Family Overview Datasheet [Online]*. https://www.xilinx.com/support/documentation/data_sheets/ds150.pdf. 42

[169] Xilinx Inc. *Virtex-6 FPGA Clocking Resources User Guide [Online]*, January 24, 2014 (Accessed May 25, 2018). https://www.xilinx.com/support/documentation/user_guides/ug362.pdf. 49

[170] IEEE. IEEE Std. 754-2008. *IEEE Standard for Floating-Point Arithmetic*, pages 1–70, Aug 2008. 55

[171] Daniel W. Lam. *Digital Linearization and Wideband Measurements in Optical Links*. Ph.D dissertation, Department of Electrical Engineering, University of California, Los Angeles, CA 90095, 2014. xiv, xv, xvii, xx, 60, 61, 63, 64, 65, 66, 71, 74, 87, 89, 91, 92, 93

[172] Keysight Technologies. *Centellax TG1B1-A Datasheet [Online]*, April 8, 2009 (Accessed July 28, 2018). https://www.keysight.com/upload/cmc_upload/All/N4962-91021.pdf. 62

[173] Keysight Technologies. *Keysight 346A Datasheet [Online]*, July 26, 2018 (Accessed August 1, 2018). https://literature.cdn.keysight.com/litweb/pdf/00346-90148.pdf. 63

[174] Mohammad Massoud Karbassian, Jun He, Ning Zhu, William Duncan, Daniel Carothers, John Wissinger, and Nasser Peyghambarian. Experiment of Transparent QoT-Aware Cross-Layer Wavelength Assignment Switching. In *Proceedings of the World Congress on Engineering and Computer Science*, volume 2, 2011. 72

[175] Michael S. Wang. *Energy Efficient, Cross-Layer Enabled, Dynamic Aggregation Networks for Next Generation Internet*. Ph.D dissertation, Columbia University, NY 10027, 2015. xv, 72, 73, 75

[176] Emmanuel Benoit Desurvire. *Erbium-Doped Fiber Amplifiers: Principles and Applications*. Wiley Series in Telecommunications and Signal Processing. Wiley, 1994. 76

[177] John Kerr. Xl. a new relation between electricity and light: Dielectrified media birefringent. *The London, Edinburgh, and Dublin Philosophical Magazine and Journal of Science*, 50(332):337–348, 1875. 79

[178] Rajiv Ramaswami, Kumar N. Sivarajan, and Galen H. Sasaki. *Optical Networks: A Practical Perspective*. Morgan Kaufmann Series in Networking. Elsevier Science, 2010. 80

[179] Katsumi Takano, Norihiro Sakamoto, and Kiyoshi Nakagawa. SPM effect on carrier-suppressed optical SSB transmission with NRZ and RZ formats. *Electronics Letters*, 40(18):1, 2004. 81

[180] Katsumi Takano, Takashi Murakami, Yuki Sawaguchi, and Kiyoshi Nakagawa. Influence of self-phase modulation effect on waveform degradation and spectral broadening in optical BPSK-SSB fiber transmission. *Optics Express*, 19(10):9699–9707, 2011. 81

[181] Fujitsu Network Communications Inc. *Fujitsu Flashwave 9500 Packet Optical Networking Platform Datasheet [Online]*, 2014 (Accessed August 12, 2018). https://www.fujitsu.com/downloads/TEL/fnc/datasheets/flashwave9500.pdf. 84

[182] Peter W. East. Fifty years of instantaneous frequency measurement. *IET Radar, Sonar & Navigation*, 6(2):112–122, 2012. 87

[183] Henryk Gruchala and Mirostaw Czyzewski. The instantaneous frequency measurement receiver in the complex electromagnetic environment. In *Microwaves, Radar and Wireless Communications, 2004. MIKON-2004. 15th International Conference on*, volume 1, pages 155–158, May 2004. 87

[184] William B. Sullivan. Instantaneous frequency measurement receivers for maritime patrol. *Journal of Electronic Defense*, 25(10):55–62, 2002. 87

[185] William B. Sullivan. Simultaneous signal errors in wideband IFM receivers. *Microwave Journal*, 38(9):86–94, 1995. 87

[186] Timothy W. Fields, David L. Sharpin, and James B. Tsui. Digital channelized IFM receiver. In *Telesystems Conference, 1994. Conference Proceedings., 1994 IEEE National Conference on*, pages 87–90, 1994. 88

[187] Hossein Emami, Niusha Sarkhosh, Lam A. Bui, and Arnan Mitchell. Amplitude independent RF instantaneous frequency measurement system using photonic Hilbert transform. *Optics Express*, 16(18):13707–13712, 2008. 88

[188] Niusha Sarkhosh, Hossein Emami, Lam A. Bui, and Arnan Mitchell. Reduced cost photonic instantaneous frequency measurement system. *IEEE Photonics Technology Letters*, 20(18):1521–1523, 2008. 88

[189] Miguel V. Drummond, Paulo P. Monteiro, and Rogério N. Nogueira. Photonic RF instantaneous frequency measurement system by means of a polarization-domain interferometer. *Optics Express*, 17(7):5433–5438, 2009. 88

[190] Linh V. T. Nguyen. Microwave photonic technique for frequency measurement of simultaneous signals. *IEEE Photonics Technology Letters*, 21(10):642–644, 2009. 88

[191] Xihua Zou, Wei Pan, Bin Luo, and Lianshan Yan. Photonic approach for multiple-frequency-component measurement using spectrally sliced incoherent source. *Optics Letters*, 35(3):438–440, 2010. 88

[192] Lam A. Bui, Niusha Sarkhosh, and Arnan Mitchell. Photonic instantaneous frequency measurement: parallel simultaneous implementations in a single highly nonlinear fiber. *IEEE Photonics Journal*, 3(5):915–925, 2011. 88

[193] Asad M. Madni and Zoltan Tarczy-Hornoch. Microprocessor based fault finder pinpoints transmission-line faults within inches... and within minutes. *Microwave Journal*, 24(11):49, 1981. 90

[194] Asad M. Madni and Robert B. Windle. Microprocessor based hardware and digital signal processing algorithms provide a state-of-the-art approach to transmission line/antenna systems analysis. In *Electromagnetic Compatibility, 1982 IEEE International Symposium on*, pages 1–6, 1982. 90

[195] Asad M. Madni and Ernest J. Nyiri. Fast fourier transform and digital filtering solution to transmission line analysis. In *Military Microwaves' 82*, pages 423–428, 1983. 90

[196] Zoltan Tarczy-Hornoch, Asad M. Madni, and Joseph Fala. Transmission line analyzer for automatically identifying the severities and locations of multiple mismatches, December 1986. US Patent US4630228. 90

[197] Asad M. Madni. *Frequency domain reflectometry and digital signal processing solution to transmission lines/antenna systems analysis.* Ph.D dissertation, California Coast University, Santa Ana, CA, 1987. 90

[198] Bahram Jalali and Cejo Konuparamban Lonappan. A method for signal characterization, March 2018. US Patent Applied. xvii, 93, 94

[199] Paul D. Hale and Dylan F. Williams. Calibrated measurement of optoelectronic frequency response. *IEEE Transactions on Microwave Theory and Techniques*, 51(4):1422–1429, Apr 2003. 96

[200] Yongqiang Shi, Lianshan Yan, and Alan E. Willner. High-speed electrooptic modulator characterization using optical spectrum analysis. *Journal of Lightwave Technology*, 21(10):2358–2367, Oct 2003. 96

[201] Alfred Kan Min Lam, Mark Fairburn, and Nicolas A. F. Jaeger. Wide-band electrooptic intensity modulator frequency response measurement using an optical heterodyne down-conversion technique. *IEEE Transactions on Microwave Theory and Techniques*, 54(1):240–246, Jan 2006. 96

[202] Xu Ming Wu, Jiang Wei Man, Liang Xie, Yu Liu, Xiao Qiong Qi, Li Xian Wang, Jian Guo Liu, and Ning Hua Zhu. Novel Method for Frequency Response Measurement of Optoelectronic Devices. *IEEE Photonics Technology Letters*, 24(7):575–577, April 2012. 96

[203] Shangjian Zhang, Chong Zhang, Heng Wang, Xinhai Zou, Yong Liu, and John E. Bowers. Calibration-free measurement of high-speed Mach–Zehnder modulator based on low-frequency detection. *Optics Letters*, 41(3):460–463, Feb 2016. 96

[204] Doug M. Baney, Wayne V. Sorin, and Steve A. Newton. High-frequency photodiode characterization using a filtered intensity noise technique. *IEEE Photonics Technology Letters*, 6(10):1258–1260, Oct 1994. 96

[205] Bang Hong Zhang, Ning Hua Zhu, Wei Han, Jian Hong Ke, Hong Guang Zhang, Min Ren, Wei Li, and Liang Xie. Development of swept frequency method for measuring frequency response of photodetectors based on harmonic analysis. *IEEE Photonics Technology Letters*, 21(7):459–461, April 2009. 96

[206] David A. Humphreys, Matthew R. Harper, Andrew JA Smith, and Ian M. Smith. Vector calibration of optical reference receivers using a frequency-domain method. In *Precision Electromagnetic Measurements Digest, 2004 Conference on*, pages 526–527, June 2004. 96

[207] Keizo Inagaki, Tetsuya Kawanishi, Hidenori Iwai, and Yoichi Oikawa. Development of lightwave frequency response analyzer for characterizing O/E conversion devices. In *Microwave Photonics (MWP) and the 2014 9th Asia-Pacific Microwave Photonics Conference (APMP), 2014 International Topical Meeting on*, pages 113–116, Oct 2014. 96

[208] Tasshi Dennis and Paul D. Hale. High-accuracy photoreceiver frequency response measurements at 1.55 μm by use of a heterodyne phase-locked loop. *Optics Express*, 19(21):20103–20114, Oct 2011. 96

[209] Shangjian Zhang, Heng Wang, Xinhai Zou, Yali Zhang, Rongguo Lu, Heping Li, and Yong Liu. Optical Frequency-Detuned Heterodyne for Self-Referenced Measurement

of Photodetectors. *IEEE Photonics Technology Letters*, 27(9):1014–1017, May 2015. 96

[210] Sheng-Lung Huang, Chi H. Lee, and Hing-Loi A. Hung. Real-time linear time-domain network analysis using picosecond photoconductive mixer and samplers. *IEEE Transactions on Microwave Theory and Techniques*, 43(6):1281–1289, Jun 1995. 97

[211] Shingo Uehara. Calibration of optical modulator frequency response with application to signal level control. *Applied Optics*, 17(1):68–71, Jan 1978. 97

[212] H. P. Huang, N. H. Zhu, Q. Q. G. Hasen, Y. Liu, X. Wang, E. Y. B. Pun, and P. S. Chung. Small-Signal Power Measuring Technique for Measuring the Frequency Response of Electroabsorption Modulators. *IEEE Photonics Technology Letters*, 18(23):2451–2453, Dec 2006. 97

[213] Sebastian Gustafsson, Mattias Thorsell, Jörgen Stenarson, and Christian Fager. An Oscilloscope Correction Method for Vector-Corrected RF Measurements. *IEEE Transactions on Instrumentation and Measurement*, 64(9):2541–2547, Sept 2015. 97

[214] Fermionics Opto-technology. *FD100ST High Speed InGaAs PIN Photo-diodes Datasheet [Online]*, 2002 (Accessed August 16, 2018). `http://www.fermionics.com/PDFfiles/FD100series.pdf`. 100

[215] David H. Auston, Kin P. Cheung, and Peter R. Smith. Picosecond photoconducting hertzian dipoles. *Applied Physics Letters*, 45(3):284–286, 1984. 121

[216] Peter R. Smith, David H. Auston, and Martin C. Nuss. Subpicosecond photoconducting dipole antennas. *IEEE Journal of Quantum Electronics*, 24(2):255–260, 1988. 121

[217] Christof Fattinger and Daniel R. Grischkowsky. Terahertz beams. *Applied Physics Letters*, 54(6):490–492, 1989. 121

[218] Binbin B. Hu, Justin T. Darrow, Xi-Cheng Zhang, David H. Auston, and Peter R. Smith. Optically steerable photoconducting antennas. *Applied Physics Letters*, 56(10):886–888, 1990. 121

[219] L. Xu, X-C. Zhang, D.H. Auston, and B. Jalali. Terahertz radiation from large aperture si p-i-n diodes. *Applied Physics Letters*, 59(26):3357–3359, 1991. 121

[220] Xi-Cheng Zhang, Binbin B. Hu, Justin T. Darrow, and David H. Auston. Generation of femtosecond electromagnetic pulses from semiconductor surfaces. *Applied Physics Letters*, 56(11):1011–1013, 1990. 121

[221] Shun Lien Chuang, Stefan Schmitt-Rink, Benjamin I. Greene, Peter N. Saeta, and Anthony F.J. Levi. Optical rectification at semiconductor surfaces. *Physical Review Letters*, 68(1):102, 1992. 121

[222] Martin Van Exter, Christof Fattinger, and Daniel R. Grischkowsky. High-brightness terahertz beams characterized with an ultrafast detector. *Applied Physics Letters*, 55(4):337–339, 1989. 121

[223] Stephen E. Ralph and Daniel R. Grischkowsky. Thz spectroscopy and source characterization by optoelectronic interferometry. *Applied Physics Letters*, 60(9):1070–1072, 1992. 121

[224] Qi Wu and Xi-Cheng Zhang. Free-space electro-optic sampling of terahertz beams. *Applied Physics Letters*, 67(24):3523–3525, 1995. 121

[225] Bahram Jalali, Cejo Konuparamban Lonappan, and Asad M. Madni. A method for characterizing Terahertz signals, 2018. US Patent Applied. xix, 121, 122